University of Southampton Research Repository

Copyright © and Moral Rights for this thesis and, where applicable, any accompanying data are retained by the author and/or other copyright owners. A copy can be downloaded for personal non-commercial research or study, without prior permission or charge. This thesis and the accompanying data cannot be reproduced or quoted extensively from without first obtaining permission in writing from the copyright holder/s. The content of the thesis and accompanying research data (where applicable) must not be changed in any way or sold commercially in any format or medium without the formal permission of the copyright holder/s.

When referring to this thesis and any accompanying data, full bibliographic details must be given, e.g.

Thesis: Author (Year of Submission) "Full thesis title", University of Southampton, name of the University Faculty or School or Department, PhD Thesis, pagination.

Data: Author (Year) Title. URI [dataset]

UNIVERSITY OF SOUTHAMPTON

Faculty of Engineering and Physical Sciences
School of Engineering

Flow past flapping foils:
Surface texture and unsteadiness effects

by

Rodrigo Vilumbrales Garcia

ORCiD: 0000-0003-3778-0082

A thesis for the degree of
Doctor of Philosophy

February 2024

University of Southampton

Abstract

Faculty of Engineering and Physical Sciences
School of Engineering

Doctor of Philosophy

Flow past flapping foils: Surface texture and unsteadiness effects

by Rodrigo Vilumbrales Garcia

Evolution has lead to extremely efficient biological swimmers and flyers. Animals are able to use the surrounding flow to obtain performance gains, like in the fish-schooling operation. Although nowadays their way of travelling is being replicated in mechanical systems, such as Micro Air Vehicles or energy harvesters, we are still far from achieving their efficiency. In this thesis we aim to advance towards more efficient propulsive methods. We mimic the fish-schooling operation by the use of tandem flapping foils, and we explore real-life aspects that could influence the hydrodynamics performance. Do animals present surface texture for propulsive performance reasons? How does the unsteadiness in the surrounding flow affect the performance of a flapping foil? In this thesis we aim to answer those questions by conducting numerical simulations and experiments. We find that the addition of surface texture (36% and 70% coverage area) is prejudicial for a pure pitching foil. As for the second question, we explore the importance of adding physically relevant inputs to recover the dynamics of a flapping foil submerged inside unsteady incoming flow, and executing transitions in its motion. We later use the recovered force model to predict the path that maximises its propulsive performance. We finish by focusing on more efficient ways of developing the transition motion, finding that the optimal manoeuvre is associated with a more efficient evolution of the transition velocities.

Contents

List of Figures **ix**

List of Tables **xiii**

Declaration of Authorship **xv**

Acknowledgements **xvii**

1 Introduction **1**
- 1.1 Motivation 1
- 1.2 Aim and objectives 2
- 1.3 Thesis structure 3
- 1.4 Results summary 3
- 1.5 Acknowledgements 4

2 Literature Review **5**
- 2.1 Introduction 5
- 2.2 Dimensionless parameters 5
- 2.3 Flapping foils in uniform upstream flow 7
  - 2.3.1 Kinematics 7
  - 2.3.2 Forces generation and wake characteristics 8
  - 2.3.3 Foil texture and flexibility 12
  - 2.3.4 Flapping foil manoeuvring 13
- 2.4 Tandem flapping foils 14
- 2.5 Machine Learning techniques applied to flapping foils. 16
- 2.6 Applications 17

3 Methodology **19**
- 3.1 Computational 19
  - 3.1.1 Solver 19
  - 3.1.2 Grid analysis 19
  - 3.1.3 Validation 20
- 3.2 Experimental 22
  - 3.2.1 Recirculating water tunnel 22
    - 3.2.1.1 Experimental flapping equipment 23
    - 3.2.1.2 Flapping arm 23
  - 3.2.2 Kinematics control and forces acquisition 24
    - 3.2.2.1 cRIO 25

3.2.2.2 SCL protocol 25
3.2.3 PIV techniques 27
3.3 Machine learning and System Identification techniques 27
3.3.1 Machine Learning tools 27
3.3.1.1 Neural ODE 28
3.3.2 System identification 28
3.3.2.1 Sparse Identification of nonlinear Dynamics (SINDy) . . 28

4 Effects of surface roughness on the propulsive performance of pitching foils 31
4.1 Introduction 33
4.2 Experimental setup and methodology 34
4.3 Results 37
4.3.1 Flow-field and force production analysis of foils with different roughness area coverage ratios 37
4.3.2 Comparison between static and flapping regimes 40
4.4 Conclusions 43

5 Force models for a flapping foil under unsteady upstream conditions 45
5.1 Introduction 47
5.2 Methodology 48
5.3 Force models for a foil immersed in uniform upstream conditions 50
5.4 Force models for a flapping foil immersed in unsteady upstream conditions. 52
5.4.1 Force prediction capabilities 54
5.4.2 Optimum path finding capabilities 56
5.5 Experimental implementation 58
5.5.1 Results 59
5.6 Conclusions 63

6 Trajectory optimisation for flapping foils under unsteady inflow conditions 65
6.1 Abstract 65
6.2 Introduction 65
6.3 Methodology 66
6.4 Results 69
6.4.1 Convergence analysis of the optimisations 69
6.4.2 Optimised trajectories for a maximum transition time of one cycle 69
6.4.3 Optimised trajectories for a maximum transition time of three cycles 73
6.4.4 Sensitivity analysis of the trajectory control points 75
6.5 Conclusions 78

7 Conclusions 79
7.1 Conclusions 79
7.2 Future work 80

Appendix A Physics-based and Machine learning predictions of maneuvering forces in unsteady inflow conditions 83
Appendix A.1 Introduction 83

Appendix A.2 Problem definition and data generation 85
Appendix A.3 Physics-based performance estimation approaches 86
  Appendix A.3.1 Quasi-steady model 86
  Appendix A.3.2 Adapted Theodorsen model 87
Appendix A.4 Machine Learning performance estimation approaches 88
  Appendix A.4.1 LSTM 89
  Appendix A.4.2 Neural ODE 90
  Appendix A.4.3 SINDy 90
Appendix A.5 Results 91
Appendix A.6 Conclusions 94

References **97**

List of Figures

2.1 Transition from drag producing wake to thrust producing wake. Lagopoulos et al. (2019) . . . 9
2.2 Wake shape in terms of the effective angle of attack and St value Anderson et al. (1998) . . . 10
2.3 Sketch of the forces and induced velocities seen by a flapping foil in tandem arrangement . . . 11
2.4 Wakes of single flapping foil, and a high-performance and low-performance tandem configuration. Muscutt et al. (2017a) . . . 15

3.1 Schematics of the grid used in this thesis. Extracted from Lagopoulos (2021) . . . 21
3.2 Analysis of the convergence achieved by the lotus simulations for a grid spacing of 192 points per chord. The figure presents a comparison between the instantaneous C_X produced at consecutive flapping cycles. . . . 21
3.3 Comparison between the $\overline{C_X}$ values described by Anderson et al. (1998) for a solo flapping foil (Cases 1-8). Case 9, extracted from Muscutt (2017) follows the same kinematics as Case 5. Case 10 is equivalent to Case 7. . . 22
3.4 Schematics of the University of Southampton recirculating water flume. 23
3.5 Schematic of the flapping carriage used to perform the heaving/pitching motions. . . . 24
3.6 Schematics of the flapping arm built for this thesis. . . . 25
3.7 Schematics of the original labview-based cRio control system, extracted from (Muscutt, 2017) . . . 26
3.8 Schematics of the MATLAB-based SCL control protocol. . . . 26

4.1 Schematics of the experimental setup in the water flume (A), the actuation arm (B), foils with three different roughness area coverage ratio (C), and the forces acting on the foil (D). . . . 35
4.2 PIV results for $Re = 28,000$. $t/T = 0.15$ (A,B,C) and $t/T = 0.50$ (D,E,F) for the Smooth (A,D), 36% (B,E) and 70% (C,F). Instantaneous C_X (G) and instantaneous C_P (H). Figure 2 (G,H) contains confidence intervals calculated as $CI = 4.6\sigma/\sqrt{N}$. . . . 38
4.3 (A) Power Spectral Density (PSD) analysis of the instantaneous C_X at $Re = 28,000$. The cross indicates the location of the peak for each case. (B) Peak frequency across the Re values considered. A value of 2 denotes that the thrust force signal peak f is equal to two times the input pitching frequency f_0. . . . 38

4.4 A) $\overline{C_X}$ obtained in the current study (red range) and compared with previous studies against Re: Senturk and Smits (2019) (gray). The data enclosed by the blue box presents an inset of $\overline{C_X}$ data for the Re range of $17,000 \leq Re \leq 33,000$. B) $\overline{C_P}$ results (hexagon) and η (cross) for current and previous studies: Mackowski and Williamson (2017) (dark-gray) for $Re = 16,600$, $k = 4$, $PP = 0c$ and $\theta_0 = 8^o$. Senturk and Smits (2019) (gray) for $500 \leq Re \leq 32,000$, $St = 0.2 - 0.4$, $PP = 0.25c$, $\theta_0 = 8^o$. Fernandez-Feria and Sanmiguel-Rojas (2020) for $Re = 16,000$, $k = 4$, $PP = 0c$ and $\theta_0 = 8^o$. The shadow region introduces the confidence intervals calculated as $CI = 4.6\sigma/\sqrt{N}$. 39

4.5 Averaged C_D values obtained for a static smooth foil at $\theta = 0^o$. The shadow region introduces the confidence intervals calculated as $CI = 4.6\sigma/\sqrt{N}$. 39

4.6 A) Static C_X vs angle of attack Θ measured using static foils at $Re = 28,000$. Smooth foil is presented in light blue, 36% in medium blue, and 70% in dark blue. The red dashed line indicates the θ used to compare with the unsteady regime, defined as $\theta_s = 4.75°$. B) Thrust and drag penalty due to roughness for both the flapping (triangles) and static results (crosses) for the 36% case (medium blue) and the 70% case (dark blue). The shadow region introduces the confidence intervals calculated as $CI = 4.6\sigma/\sqrt{N}$. 41

4.7 Pitching cycle-averaged vorticity (A,B,C), pitching instantaneous vorticity at $\theta = 6°$ degrees (E,F,G) and static PIV results at $\theta = 6°$ (I,J,K). Smooth foil (A,E,I), 36% (B,F,J), and 70% (C,G,K). The comparison of the wakes generated by the foils at each of the conditions is presented at (D,H,L). All data obtained at $Re = 28,000$. 42

5.1 Sketch of the tandem arrangement considered in this study. The bottom part of the figure introduced the manoeuvre motion executed by the hind foil (green) in its kinematics during cycles 0 to 1. 49

5.2 Comparison between the projections for three selected test cases and the target data. Delay - raw model (pink), delay - filtered (blue) and kinematics model (red). The insets contain the components recovered for each of the models during the system identification process. 52

5.3 Analysis of the components recovered by the kinematics model for the solo foil scenario. Each row introduces the sum of the contributions of each of the elements presented at the inset of Figure 5.2. 53

5.4 Schematics of the virtual simulations used to track the evolution of the wake. The information is included as a control input in the wake info model. 53

5.5 Comparison between target data and projections for the solo and tandem scenarios. Kinematics solo model (red), kinematics tandem model (green), and wake info (purple). The bottom figure introduces a comparison of the error achieved for all the test cases between the wake info and kinematics model. 55

5.6 Analysis of the components recovered by the wake info model for the tandem foil scenario. The first row presents the contribution of the kinematic terms, while the second adds to the previous the wake terms, as seen on the inset. 55

5.7 Instantaneous vorticity at three different time stamps for the test case presented at Figure 5.6. 56
5.8 Study of the optimum path selection capabilities of the models. Target data (black), wake info (purple) and kinematics (green), at three different St values: 0.36 (training), 0.30 and 0.40. Light squares indicate routes with large performance detriment. Darker squares indicate optimum path inside the wake 57
5.9 Application of the optimum paths prediction capabilities. Each of the lines starts at a different ϕ_0 and corresponds to a simulation based on the optimum path found by the models. The top row introduces the wake info, and the bottom the kinematics. The coloured lines surrounding the forces data highlight the convergence capabilities of the wake info, specially for $St = 0.36$ and $St = 0.40$ 58
5.10 Schematics of the tandem flapping foil experiments. A) depicts the details of the water tunnel setup. B) Introduces the flapping arm components. C) Presents the schematics of the forces 60
5.11 Lift amplitude obtained at the ϕ_1 state. The blue region correspond to low-performance kinematics. The green region highlights high-performance situations. 61
5.12 Instantaneous C_X, C_Y and C_P obtained during the experiments (green) and simulations (black) for three selected transition cases. 62
5.13 Instantaneous C_Y and C_P for three selected transition lengths. One cycle (black, numerical), 1.5 cycles (red, experimental) and 2 cycles (blue, experimental). 62
5.14 Analysis of the power cost used during the transitions. One cycle (black, numerical), 1.5 cycles (red, experimental) and 2 cycles (blue, experimental). 63

6.1 Schematics of the transition phase. The signal is constructed using Hermit spline, controlled by five nodes of different time (x) and ϕ values. . . 68
6.2 Instantaneous phasing ϕ, C_L and C_P results for different trials of the optimisation. The results are based on Lotus simulations conducted for the optimum trajectory recovered by the approach. The dashed-line at the top row presents an equivalent transition following a sigmoid evolution of ϕ, as described at Chapter 5. The top row introduces the results for a maximum transition time of one cycle. The bottom row presents the results for a maximum transition time of three cycles. 70
6.3 Optimised trajectories and forces for a maximum transition time of one cycle. Top-left compares the convergence process found by the optimiser (grey dots) against validation at selected iterations using Lotus (coloured dots). Top-right introduces the optimised transition kinematics (ϕ) and the instantaneous frequency $\dot{\phi}$. The trajectory is compared with a sigmoid evolution, as described at Chapter 5. The C_L and C_P evolution are shown at bottom-left and bottom-right sub-figures. 71
6.4 Comparison between the force model estimations for C_L and C_P^* (purple) and Lotus results (coloured lines) for C_L and C_P at different iterations. . 72
6.5 Instantaneous vorticity at two selected time instants for the transitions presented at Chapter 5 (green) and the optimised kinematics (Red) . . . 73

6.6 Optimised trajectories and forces for a maximum transition time of three cycles. Top-left compares the convergence process found by the optimiser (grey dots) against validation at selected iterations using Lotus (coloured dots). Top-right introduces the optimised transition kinematics (ϕ) and the instantaneous frequency $\dot{\phi}$. The trajectory is compared with a sigmoid evolution, as described at Chapter 5. The C_L and C_P evolution are shown at bottom-left and bottom-right sub-figures. 74

6.7 Comparison of the forces and flow fields for equivalent transition cases with 3 control points (green), and 5 control points (red). Top left figure introduces the ϕ and $\dot{\phi}$ evolution. Bottom left introduces the C_P evolution. The instantaneous vorticity is shown at the time steps denoted by vertical dashed lines. 75

6.8 Sensitivity analysis conducted for the optimised trajectory. The first row presents the modifications on the coordinates of the fourth control node. The second row introduces the changes done on the coordinates of the third control node. Each of the new cases is run using the CFD solver . . 76

6.9 Results for the sensitivity analysis conducted at the node that controls the division in the acceleration stage. The black lines represent the base trajectory and forces. Each of the trajectories is run in Lotus, and the resultant C_P is presented here. The first column introduces the optimised and modified ϕ (continuous line) and $\dot{\phi}$ (dashed) evolution. The last column compares the obtained power cost compared to the optimum trajectory. The last column compares the obtained power cost compared to the optimum trajectory. Values below 1 represent an improvement in the power expense. 77

6.10 Results for the sensitivity analysis conducted at the node that controls the deceleration part of the trajectory. The black lines represent the base trajectory and forces. Each of the motions is run in Lotus, and the resultant C_P is presented here. The first column introduces the optimised and modified ϕ (continuous line) and $\dot{\phi}$ (dashed) evolution. The last column compares the obtained power cost compared to the optimum trajectory. Values below 1 represent an improvement in the power expense. 77

Appendix A.1 Sketch and comparison of the virtual probes method and the tandem simulations. The red and green dots indicate virtual probes acting and moving as virtual hind foils. The red dot in the left hand size of the figure helps to represent that the virtual dots are place at the LE of their equivalent foil. 88

Appendix A.2 Time signal prediction comparison for the HP case. HP test case at the left column and LP test case at the right column. LSTM results (A and B), NODE results (C and D) and SINDy (LASSO) results (E and F). 91

Appendix A.3 NRMSE comparison. HP test case at the left column and LP test case at the right column. C_X (A and B) and C_Y (C and D) 93

List of Tables

3.1 Grid density study 20

4.1 Experimental parameters used in the current study 36

5.1 Parameters used to recover the force models. 51
5.2 Experimental parameters used in the current study 59

6.1 Table of parameters used in the optimisation. The values are presented in the bounds allowed to the optimiser. Variables coloured in red are fixed. 68

Appendix A.1 Numerical cases 86
Appendix A.2 Machine Learning models: state vector 89
Appendix A.3 LSTM parametric study 89
Appendix A.4 Neural ODE parametric study 90

Declaration of Authorship

I declare that this thesis and the work presented in it is my own and has been generated by me as the result of my own original research.

I confirm that:

1. This work was done wholly or mainly while in candidature for a research degree at this University;
2. Where any part of this thesis has previously been submitted for a degree or any other qualification at this University or any other institution, this has been clearly stated;
3. Where I have consulted the published work of others, this is always clearly attributed;
4. Where I have quoted from the work of others, the source is always given. With the exception of such quotations, this thesis is entirely my own work;
5. I have acknowledged all main sources of help;
6. Where the thesis is based on work done by myself jointly with others, I have made clear exactly what was done by others and what I have contributed myself;
7. Parts of this work have been published as:

Signed:.. Date:..................

Acknowledgements

In the words of David Hume, ”the sweetest and most inoffensive path of life leads through the avenues of science and learning”. I would like to thank my advisors, Bharath Ganapathisubramani and Gabriel Weymouth, for opening that avenue to me. Without your support and encouragement, this thesis would have never been completed. I would also like to thank my lab mate and friend Melike Kurt. I will certainly miss our little daily chats, and those long hours at the lab with you. During this path I have met a lot of amazing people. Special mention to those who started their journey with me. Mattias, Francis, Bradley, Jonah, you have definitely made these four years easier. We have been through a lot together, and your support and friendship has been extremely important in this process. To every single member of Gabe’s and Bharath’s group, thank you! I really hope our lines will cross again in the future. Last, but not least, I would like to acknowledge the continuous support of my family and friends, who have always been there in the good days but, more importantly, in the not so-good ones. This thesis is yours as much as it is mine.

Chapter 1

Introduction

1.1 Motivation

Life forms optimise gradually their physiology to adapt to their environment Darwin and Bynum (2009). This gradual evolution has lead to extremely efficient biological swimmers and flyers, that are nowadays being replicated in mechanical systems, such as Micro Air Vehicles or energy harvesters.

It is well known that animals need to adapt to its surroundings in order to accomplish efficient ways of travelling. An example of this is the fish-schooling organisation, where several individuals combine their efforts to achieve benefits Weihs (1973). This arrangement, characterised by high levels of unsteadiness and constantly changing circumstances, can provide a performance benefit only when the attitude of the individuals is properly tuned. If the motion of the fish is not phased accordingly with the surrounding flow, large penalties have been observed Lupandin (2005). Flapping foils in tandem configuration have been widely used in an effort to understand and replicate the augmentation effects of fish-schooling. In line with the findings in the biological field, previous studies have shown a potential benefit if the motion of the foil located at the back of the configuration is properly tuned to the unsteadiness coming from the leader Muscutt et al. (2017a). The characteristics of the operation imply that a deeper knowledge is needed about the mechanisms to maximise the propulsive performance. The existing tools to model the forces evolution of a flapping foil are either limited to idealised conditions Garrick (1936); Theodorsen and Mutchler (1935), making them unrealistic for real life applications.

In this thesis, we aim to progress towards a real-life application of a flapping foil system able to maximise its swimming performance. This implies that a closer attention needs to be paid to the aspects characterising the swimming of real animals. For example, a certain degree of roughness is present in every living swimmer. Although some efforts have been paid to relate that texture to hydrodinamic benefits, for example by replicating the well known denticle-like texture of sharks Domel et al. (2018b), the results are not conclusive. Previous work has shown that a potential drag benefit could be achieved, but it is still to be seen if the drag reductions are coming from the shape of the rough element, or just from the rough texture itself.

The second aspect to consider revolves around the high-unsteadiness of real life swimmers. As discussed before, the fish schooling is a constantly changing environment, and any real-life application needs to be able to recognise it, and adapt to it to maintain gains. Also, the need to adapt to comes associated with a requirement for manoeuvring motions. We believe that new tools must be developed to better understand the effects of unsteadiness on the propulsive performance of a foil, and to account for the effects of manoeuvring kinematics. In this thesis we aim to use state-of-the-art system identification tools that could not only produce more realistic force models, but also provide a better understanding of the mechanisms behind any potential gains. We aim to use the force model to predict the optimum path that maximises the performance of the foil, and to execute the required manoeuvre in the most efficient way.

1.2 Aim and objectives

The aim of this thesis can be defined as "to analyse the effects of surface texture and flow unsteadiness on the propulsive performance of flapping foils". The objectives needed in order to achieve this aim are stated in the next section.

The objectives of this thesis can be summarised as follows:

-Objective one: analysis of the hydrodynamic effects of surface textures on the propulsive performance of a flapping foil.

-Objective two: development of force models to predict the performance of a flapping foil swimming under unsteady incoming conditions, and subjected to manoeuvring motions.

-Objective three: use of sparse force models to predict the path that maximises the performance of a flapping foil inside unsteady incoming flow.

-Objective four: optimisation of the manoeuvring motion executed by a flapping foil to adapt to the incoming flow in order to maximise its propulsive performance.

1.3 Thesis structure

The present thesis is divided as follows. A general literature review is presented in Chapter 2 covering the principal literature in the field of flapping foils. Chapter 3 presents the numerical and experimental methodology followed in this thesis.

Chapter 4 analyses the effects of surface roughness on the propulsive performance of a pure-pitching foil, and compares it with the effects of similar texture on steady wings.

Chapter 5 describes the process followed to develop force models to predict the performance of a foil executing manoeuvring motions under unsteady flow conditions. The force model is later used to estimate the optimum route inside the incoming wake that maximises the performance of a flapping foil. It also introduces an experimental implementation of the manoeuvring methodology. We also perform a first analysis focused on identifying efficient ways of manoeuvring.

Chapter 6 focuses at optimising the transition motion needed by a flapping foil to maximise its performance. We focus on the hydrodynamic characteristics and forces productions to understand how can we execute manoeuvring motions in an efficient manner.

Chapter A presents a first approach conducted to explore ML techniques related to estimating the performance of flapping foils.

1.4 Results summary

The main findings of this thesis are detailed next:

Chapter 4: ”Effects of surface roughness on the propulsive performance of pitching foils”. We explored the effects of commercially available rough elements on the propulsive performance of a pitching foil. The results suggest that the texture is providing a mild penalty due to higher drag productions. We compared the flapping case with steady foils, finding that the first are more robust to roughness. This effect could be explained by considering the importance that aspects such as the kinematics or Strouhal value have on the performance of a flapping foil. This two conditions could be neglecting the effect of the rough elements.

This effect is explained by considering the influence that parameters such as the kinematics or Strouhal value have on flapping propulsion.

The findings of this chapter focusing on the pitching studies have been accepted for publication at JFM (Vilumbrales-Garcia et al. (2023)). Another article, looking at the steady foils part of the study is yet to be submitted ”Force generation and flow over static foils with surface roughness” Bioinspiration and Biommimetics, Kurt et. al.

Chapter 5: in this chapter we used new system-identification tools able to recover the dynamics of highly unsteady systems. By carefully selecting the inputs associated to the process we were able to recover a force model able to predict the performance of a flapping foil subjected to manoeuvres and unsteady inflow conditions. We later used that model to predict the optimum path for the foil to maximise its performance. We implemented experimentally the transition manoeuvre needed to maximise the performance of the flapping foil. Although the propuslive performance was greatly improved after the transition, the manoeuvre was associated to large power consumption. We conducted a first analysis to identify more efficient ways of manoeuvring.

The findings of this chapter are going to be submitted to JFM under the title ”Force models for a flapping foil under unsteady upstream conditions”, Vilumbrales-Garcia et. al.

Chapter 6: in this chapter, we focused on optimising the manoeuvring motion needed to maximise the performance of a flapping foil. By using evolutionary algorithms, we were able to find a new transition motion able to reduce the overall power consumption, characterised by a more efficient evolution of the accelerations needed to conduct the manoeuvre.

The findings of this chapter are going to be submitted for publication under the title ”Trajectory optimisation for flapping foils under unsteady inflow conditions”, Vilumbrales et. al.”, Vilumbrales-Garcia et. al.

Chapter A: in this chapter we developed a first analysis on Machine Learning tools to predict the performance of a flapping foil. Although the results suggested that a good accuracy could be achieved, the set up of the method was not suitable for real life applications. Still, we have used the knowledge gained during this work to conduct the chapters of this thesis.

Te work presented on this Appendix has been published as conference proceedings. Vilumbrales-Garcia et al. (2022))

1.5 Acknowledgements

This research was supported financially by the Office of Naval Research Global Award N62909-18-1-2091, the Engineering and Physical Sciences Research Council (Grant No: EP/R034370/1) and the doctoral training award.

Chapter 2

Literature Review

2.1 Introduction

This section presents an study of the existing literature in the field of flapping foils. At section 2.2 we analyse fundamental parameters related to the performance of flapping foils. A first analysis of the mechanics of flapping foil devices swimming in uniform upstream flow, also known as solo foils is introduced at section 2.3, were the impact of aspects such as the wake characteristics, the kinematics or the foil shape and texture is discussed. Section 2.4 presents the mechanisms behind the tandem flapping foil operation. We continue by providing an introduction of machine learning and system identification tools, such as Deep Reinforcement Learning, that are being used to recover the dynamics of a flapping foil under unsteady inflow conditions, and to maximise the performance of tandem-foil arrangements, and conclude with an analysis of several applications where flapping foils have been shown to be efficient propulsors section 2.6. The literature review introduced here will be complemented in each of the chapters by a more detailed analysis of the state of the art.

2.2 Dimensionless parameters

The use of dimensionless numbers is important to compare findings and systems of different scales. In this thesis, dimensionless numbers will be used to present final results, and to validate against existing literature.

In the field of flapping foils, there are two important dimensionless numbers related to the fluid mechanics of the operation: the Strouhal (St) and the Reynolds number (Re).

StrouhalNumber: St is used to describe oscillating flow mechanisms and can be described as follows:

$$St = \frac{2Af}{U_\infty} \tag{2.1}$$

where A is half the amplitude of the motion of the foil, f is the oscillating frequency, and U_∞ is the free-stream velocity of the flow. The effects of St on the swimming and flying performance of animals have been widely studied in the past. Eloy (2012) found an optimal St range from 0.15 to 0.8 for animals of different size. Rohr and Fish (2004) reported that cetaceans efficient swimming is achieved for St values in the range of 0.2-0.4. Rohr et al. (1998) analysed the swimming of dolphins to find an optimum St of 0.25 and 0.27. Similar values were found by Taylor et al. (2003) for fish, bats and insects. Nudds et al. (2004) discovered that cruising birds achieve high propulsive efficiency when flying towards the lower end of the $St = 0.2 - 0.4$ range. Equivalent values have been discovered in the field of flapping foils, commonly used to replicate the swimming operation of aquatic animals. A high propulsive efficiency is usually achieved when the motion of the foils is tuned to the $St = 0.2 - 0.4$ range (Triantafyllou et al., 1991, 1993, 2000). In line with previous studies and biological findings, the experiments and simulations conducted in this thesis are limited to the optimum range fund by previous studies. In an effort to generate efficient swimmers, we will limit the Strouhal range operation between $St = 0.30$ and $St = 0.40$

ReynoldsNumber: Re relates the effects of inertial to viscous forces in a fluid, where higher values are associated with more turbulent flow. It can be defined as follows:

$$Re = \frac{LU_\infty}{\nu} \tag{2.2}$$

where L is a characteristic length, usually associated with the chord of the foil, and ν is the kinematics viscosity.

The swimming Re widely varies depending on the size of the animal. It can be as low as 10^{-5} for micro-organism, and as high as 10^7 for whales (Salta et al., 2010; Eloy, 2012). Several studies have been carried out in the field of flapping foils to analyse the effects of variations in the Re on the propulsive forces and efficiency. Ol (2007) found negligible impacts of Re for a high-frequency pitching and plunging aerofoil at low Re. Medjroubi et al. (2011) conducted simulations for a heaving foil with a Re in the range of 800 to 10^4, and reported no major effects neither on the flow structure nor on the aerodynamical loads. Similar effects were achieved by Ashraf et al. (2011) for a $Re = 2000 - 20000$. In line with the previous studies, Baik et al. (2012) reported negligible effects on the propulsive performance of pitching and heaving foils in the Re range of 5000-20000.

2.3 Flapping foils in uniform upstream flow

This sections presents an overview of the existing literature in the field of flapping foils submerged in uniform upstream conditions, also known as solo foils. We start by providing an analysis of the mechanisms behind the forces production at section 2.3.2. Next, we study the impact that parameters such as the kinematics (section 2.3.1) or the foil shape and texture (section 2.3.3) have on the propulsive performance. We conclude by providing an analysis of the manoeuvring capabilities of flapping systems. (section 2.3.4) .

2.3.1 Kinematics

The kinematics of a flapping foil play an important role in the force production and propulsive efficiency. The motion is usually prescribed by a heaving or plunging attitude, consisting of a lateral displacement of the body, a pitching motion, or a combination of both, usually described as coupled kinematics.

$$h = Asin(2\pi ft), \quad \theta = \theta_A sin(2\pi ft + \psi), \tag{2.3}$$

where A and θ_A are the heaving and pitching amplitude, f is the oscillating frequency, and ψ is a delay component between both motions, often used when considering coupled kinematics. Flapping foils following pure pitching kinematics have been usually found to be inefficient in terms of propulsive efficiency. Mackowski and Williamson (2015) reported a maximum efficiency near 15% for a NACA0012 oscillating at a $Re = 17000$ at various St values. Similar efficiency peaks have been found for several Re (Das et al., 2016) and reduced frequency values (Dewey et al., 2013). For pure heaving cases, Heathcote et al. (2008) reported a maximum efficiency of 30% for a NACA0012 at various reduced frequency values. The performance of the foil can be greatly increased by combining the heaving and pitching motions. Scherer (1968) analysed rectangular wings with mid aspect ratios and found a peak value in the efficiency of 70%. Anderson et al. (1998) reported a peak efficiency of 87% for a foil combining sinusoidal pitching and heaving kinematics, while DeLaurier and Harris (1982) noticed a maximum η value of 50%. Even when the results vary in terms of maximum efficiency, the advantage of coupled kinematics with respect to pure pitching or heaving is clear. By properly combining both motions into what is usually known as flapping kinematics, more efficient flippers can be designed.

The majority of studies conducted in the field consider only sinusoidal kinematics, but several other approaches can be noticed. Das et al. (2019) observed high-harmonics in the effective angle of attack evolution of sinusoidal coupled kinematics, and found that a square-shaped waveform can increase the thrust generation when comparing to a sinusoidal evolution. Hover et al. (2004) controlled the evolution of the effective angle of attack (α) experienced by the foil by adjusting the kinematics, finding that a cosine evolution of α can maintain a stable reverse von Kármán street for a wider St range. Lu et al. (2013) compared different waveforms and pitching amplitudes to conclude that both the thrust and the power coefficient increase as the wave progress towards quadratic, together with a stronger reverse Kármán street. Van Buren et al. (2017) designed, with the use of a Jacobi function, three types of kinematics: triangular, sinusoidal, and square. The authors linked the sinusoidal waves to high-efficiency, and the square-like motions to greater speeds. The authors compared the effects of applying non-sinusoidal motions to the pitch and heave separately, discovering that an unusual heave motion has a greater influence on the shape of the wake than the case where the pitch is modified. Slight changes in the pitch and/or heave evolution can lead to important changes in the wake and hence in the forces generated. Perfect sinusoidal waves are unlikely in nature, and analysing other types of motion could lead to applications for special cases, such as spontaneous thrust increase or manoeuvring. While the field of different types kinematics is of great interest, this thesis will contain only sinusoidal pure-pitching and/or coupled sinusoidal pitch and heave motion. The parameters will be based on the values reported by other studies, in an effort to generate efficient ways of propulsion and to validate our results against existing literature.

2.3.2 Forces generation and wake characteristics

Swimming and flying animals have evolved to use their fins or wings to produce efficient thrust or lift. By performing different types of motions, depending on the animal or the situation, animals can travel efficiently. Although the mechanisms behind the motion of animals are still not fully understood, a wide range of studies have been conducted in the last decades using flapping foils. From a biommimetic perspective, engineers and researchers have been trying to conduct studies using flapping foils in an effort to answer the remaining questions about why are animals so efficient when travelling. This section of the literature review aims to present, in a brief way, the main advancements in that field.

The motion of a flapping foil generates a distinctive feature known as Leading-Edge-Vortices (LEV) Muscutt et al. (2017a); Akhtar et al. (2007) . The presence of LEV promotes a change in the velocity or pressure fields that result in forces production. The LEVs create a low-pressure region influenced by the increment of the flow velocity in this area. The location of the LEV in terms of the foil - inner or outer face - generates a suction that can lead to a propulsive - horizontal axis - or lift - vertical axis - force. The existence of this LEV can be related to the physical phenomena known as ”Dynamic stall”, which occurs when the effective angle of attack of the motion exceeds the stall angle of attack of the steady aerofoil (Carr et al., 1977). The effects of the dynamic stall are maximised when the effective angle of attack of the foil is at its peak (Tuncer et al., 1998; Rival et al., 2011). At the beginning of the motion, the flow is attached to the surface of the foil. As the effective angle of attack increases, the foil reaches the region of dynamic stall, causing a sudden increase of the aerodynamic loading. The increment in the forces occurring during the maximum effective angle part of the flapping cycle leads to an increment in the forces, while the vortex is attached to the body (Park and Choi, 2012). Still, the kinematics followed by the object can have a drastic impact on the development of the dynamic stall. Ol et al. (2010) compared a pure-heaving and pitching-heaving flapping body, finding that the first leads to a stronger phenomena. The lower effective angle of attack promoted by the couple kinematics leads to almost no LEV, reducing the overall dynamic stall strength. Still, this reduction in dynamic stall is dependent on the pitch-heave combination. Isogai et al. (1999) reported that a 90 degree phasing between the plunging and the rotating motion leads to efficient propulsion, why other combinations can lead to large leading-edge separation, drastically reducing the overall efficiency of the motion. The 90 degree heave-pitch lag is commonly used in flapping studies Kinsey and Dumas (2008); Platzer et al. (2008), and will be used in this thesis.

When the LEV generated during the flapping cycle are detached, a characteristic wake can be observed behind the foil. The type of motion followed by the foil can strongly influence the shape and type of wake developed by the foil, and hence the propulsive performance. A bluff body immersed in a fluid can promote the formation of vortices in its wake. This phenomenon is well known for stationary cylinders. A von Kármán Street is generated by the shedding of counter-rotating vortices from either side of the body (Zdravkovich, 1996; Gerrard, 1966). The vortices remain on the side where they were formed, leading to a drag-producing wake caused by a reduction in the velocity of the flow. For a flapping foil to produce thrust, the detachment of the vortices has to form what is usually described as a reverse von Kármán Street (Triantafyllou et al., 1991). In this case, the rotation sense of the vortices detached by the body is reversed with respect to the cylinder wake, leading to an acceleration of the free-stream flow, and to a thrust-producing wake.

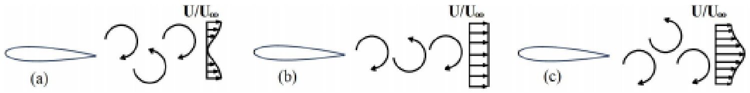

FIGURE 2.1: Transition from drag producing wake to thrust producing wake. Lagopoulos et al. (2019)

Figure 2.1 shows the transition from drag-producing wake to thrust-producing wake.

The dominant parameter to characterise each of the types is U/U_∞. This highlights that a thrust-producing wake develops a jet that increases the velocity of the flow behind the foil. If attention is paid to the direction of the vorticity structures, this jet-flow can be explained. In the case of the reverse Kármán, the velocity between the vortices is pointing downstream, which is the opposite case to the classical von Kármán Street. The propulsive force generated by a flapping foil can be related then to the strength of the reverse Kármán street Lagopoulos et al. (2019); Streitlien and Triantafyllou (1998); Bohl and Koochesfahani (2009)

The characteristics of the wake developed by a flapping foil can be linked to its kinematics. Figure 2.2 (Anderson et al. (1998)) presents a comparison of several types of wakes produced by a flapping foil under various motion regimes, with a pivot-point located at one third of the chord.

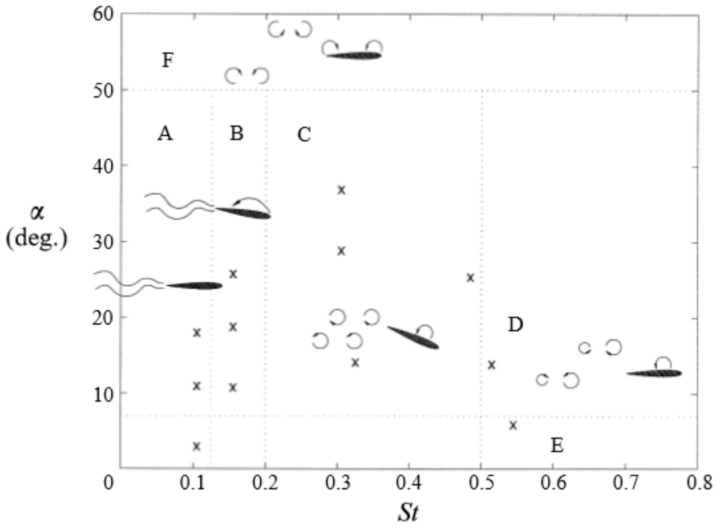

FIGURE 2.2: Wake shape in terms of the effective angle of attack and St value Anderson et al. (1998)

Regions A and B: in this area, the motion of the foil is characterised by a low *St* value, leading to a low or negative thrust production. The distinct reverse von Kármán street is not developed, and there are no distinct vorticity structures in the wake of the foil.

Region C: this region, corresponding to the efficient Strouhal range of 0.2-0.4 discussed before, presents a development of two main vortices per cycle, of opposite rotating sign. The wake of the foil evolves to a revers von Kármán Street, associated with moderately-strong LEV and high forces production. As discussed before, this area corresponds to the *St* values followed by different animals. The research covered in this thesis will be restricted to this range.

Region D: the LEV structures interact with trailing edge vorticity to generate four vortices per cycle, or 2P wake. This is characterised by asymmetry on the vorticity structures of opposite sign, which could lead to wake deflection and high forces.

The optimum St value to achieve maximum efficiency is also linked to the natural vortex shedding frequency of the foil. When the foil flaps around the previous parameter, also known as resonance, it can be concluded that the body motion is at optimum St. Rohr and Fish (2004) Taylor et al. (2003). The resonant frequency achieves maximum amplitude, which, for example, would be of the greatest importance when flexibility effects are under consideration. It is then understood that the resonance frequency would generate maximum amplitude with the minimum energy input, hence increasing the efficiency. It is important then, before entering any considerations about the kinematics of the foil, to characterise its frequency, which is known to depend on aspects such as the length of the foil, its mass distribution, or spring constant.

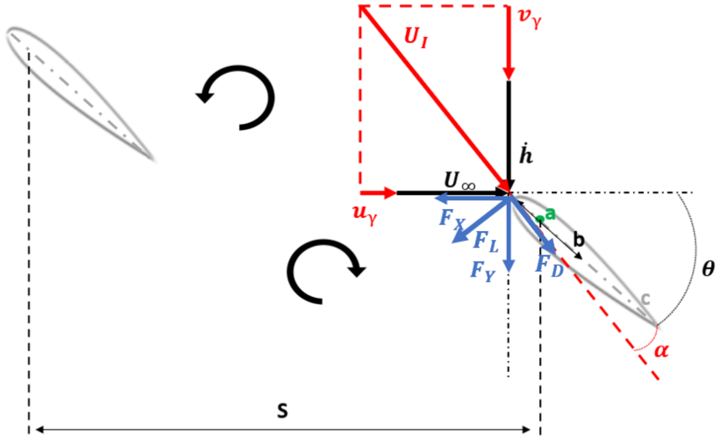

FIGURE 2.3: Sketch of the forces and induced velocities seen by a flapping foil in tandem arrangement

The forces produced by a flapping foil can be usually defined as two main components: the drag force, parallel to the induced flow seen by the aerofoil, or F_D, and the lift force, or F_L. The instantaneous forces can be projected onto the thrust and side forces as F_X and F_Y. The schematics and denomination of forces followed in this study is similar to Muscutt et al. (2017a)). A detail can be seen at Figure 2.3. In this thesis, we present the forces evolution on its dimensionless format, as follows:

$$C_D = \frac{F_D}{\frac{1}{2}\rho U^2 sc}, \qquad C_L = \frac{F_L}{\frac{1}{2}\rho U^2 sc} \tag{2.4}$$

where ρ is the density of water and U represents the free-stream flow velocity, s is the wing span, ρ is the flow density, and c is the wing chord.

as denoted before, the instantaneous C_L and C_D can be used to obtain the thrust, and side components C_X and C_Y, as follows:

$$C_X = C_L sin(\alpha) - C_D cos(\alpha), \qquad C_Y = C_L cos(\alpha) + C_D sin(\alpha) \tag{2.5}$$

where α is the induced velocity angle seen during the flapping motion defined, in line with Muscutt et al. (2017a), as $\alpha = arctan(\dot{h}/U_\infty)$

The previous components, together with the kinematics of the foil, can be used to obtain the input power and efficiency:

$$P = \dot{h}F_Y + \dot{\theta}M_Z, \qquad C_P = \frac{P}{\frac{1}{2}\rho U^3 Sc}, \qquad \eta = \frac{C_X}{C_P} \tag{2.6}$$

where ρ is the density of water and U represents the free-stream flow velocity. To differentiate between instantaneous, and time-averaged quantities, the latter are presented with an overline, as $\overline{C_X}$.

2.3.3 Foil texture and flexibility

Real life swimmers are not rigid or smooth. Every single animal presents a certain degree of surface texture and/or flexibility that can have a major impact on its swimming performance. In this section, we present briefly the research focused on analysing two main areas of surface modifications: flexibility and texture.

Flexibility

A certain degree of surface flexibility has been found to influence significantly the performance of flapping wings. It has been widely observed in nature, such as in the flight of birds or in the swimming of fish, that animals can flex their wings or fins to increment their forces production or travelling efficiency. Several works have been done in the field of single flapping foils, involving the analysis of scaling parameters Barenblatt (2003), Shyy et al. (1999) or the use of Navier Stoke's Equations to analyse the effects of flexibility in dipteran flapping flight. Ramananarivo et al. (2011) carried out an experimental study concluding that the maximum propulsion is achieved at a frequency slightly lower than the natural frequency of the system. Zhang et al. (2010) improved the findings of Ramananarivo et al. (2011) finding that, if the flapping frequency is higher than the natural frequency of the body, the foil would move backwards, highlighting the importance of the relation between the flapping frequency and the natural response of the body. There are two types of flexibility to be analysed, at least in relation to the foil. The first one, the chordwise flexibility, has been found to increase the thrust production of a flapping foil, under the right conditions, when compared to a rigid system Iverson et al. (2018), Zhu (2007), Heathcote et al. (2008), Yang et al. (2012), Jeanmonod and Olivier (2017). A certain degree of flexibility can increase the propulsion up to two times. The spanwise flexibility, on the other hand, has been less studied. Xia et al. (2018) applied this type of flexibility to small fish-like robots, finding that dolphins and other animals can benefit from spanwise flexibility on the caudal fin.

Heathcote et al. (2008) found that, for low St values, a small degree of spanwise flexibility could be beneficial, but higher flexibility in the span direction could be detrimental. Yang et al. (2012) compared both span and chordwise flexibility together finding that the two phenomena are related, and the right combination of them can lead to an increase in propulsion and efficiency. Finally, the effects of the body deflection, although can provide crucial in order to achieve performance augmentation, are indubitably going to alter the flow surrounding the flapper. Although the effects of flexibility can highly influence the performance of a flapping foil, in this thesis we will limit to a solid surface, to help with the comparison with existing literature.

Texture

Surface roughness is ever present in swimming animals. With a clear biomimetic inspiration, several studies have tried to understand the purpose of the body roughness, and its relation to swimming performance. The most common approach has been focused on the well known shark-skin type texture. Although most of the research has been done for steady bodies in gliding applications, Oeffner and Lauder (2012); Domel et al. (2018a), reported that adding denticles designed to mimic those of a shark can reduce the drag of a flapping foil or increase the swimming velocity of self-propelling bodies. Still, those benefits have only been achieved under certain conditions, such as the shape of the denticle. Varying this last parameter can lead from a performance augmentation, to a performance detriment.

Although some benefits have been reported, it is yet to be seen if those arise from the shape of the denticle, or from the presence of a rough element. To answer that question, we will conduct in this thesis a study using simple, commercially available elements to alter the texture of a flapping foil.

2.3.4 Flapping foil manoeuvring

Flapping foils have proven to be excellent manoeuvring bodies. Read et al. (2003) found that, due to the strong instantaneous lift and side-force production, the manoeuvring capabilities were ”outstanding”. The author analysed aspects such as the use of pitch bias to generate those manoeuvring forces, or the impulse starting motion. Similar results were found by Licht et al. (2004a) when the authors designed an UAV for underwater purposes. Bandyopadhyay et al. (1997) analysed the manoeuvring capabilities of several fishes and analysed the gap between the nature world and the engineering world, finding a close relation between the ability to manoeuvre and the length and scale of the fins. This ability to manoeuvre will be used in this thesis in order to find the optimum route that maximises the performance of a flapping foil.

2.4 Tandem flapping foils

This section provides an introduction of the existing literature in the field of tandem flapping foils.

The configuration where one foil is placed downstream of the other foil is known as tandem scenario. In this situation, the front foil, or fore, experiences a uniform incoming flow, and its performance is expected to be similar to the single flapping foil detailed before. On the other hand, the foil placed at the back, or hind, will encounter the wake produced by the leader. This phenomena implies a higher degree of unsteadiness in the flow experienced by the flipper, and is expected to modify its performance. The use of tandem flapping foils for propulsive or energy-harvesting applications has gained relevance in the last years. Its foundations are based on nature, and it is an idealised way of studying the physics behind the flight formation of birds (Lissaman and Shollenberger, 1970) or fish-schooling arrangements (Weihs, 1973).

The use of flapping foils in group configuration for propulsive applications find its foundations on nature: from the flight formation of birds (Weimerskirch et al., 2001) to fish schooling Weihs (1973)). Biological studies have found multiple benefits associated to fish schooling: Pitcher et al. (1982) reported that fish under school arrangement can find food faster than isolated individuals. Abrahams and Colgan (1985) found that the hydrodynamic benefits of the school arrangements could lead a to reduced respiratory rate and an increase in the swimming efficiency. Weihs (1975) observed that, for an optimal configuration, a reduction in the swimming effort of up to a factor of 5 could be achieved. The hydrodynamic benefits achieved from the interactions between two moving bodies are not necessarily limited to schooling. Several animals have evolve towards two or more set of flippers. For example, Alexander (1984) and Thomas et al. (2004) observed that dragonflies can adapt their fore and hind wing motions to adapt to different flight modes. Fish can combine the motion of their different appendix (dorsal fin, tail) to increase their overall thrust (Drucker and Lauder, 2001; Bandyopadhyay et al., 1997; Akhtar et al., 2007). Other research has been focused on the swimming of plesiosaur, finding that, if the back flipper is properly tuned to the motion of the front, a surplus of up to two times in the thrust production can be achieved (Muscutt et al., 2017b,a). The use of tandem flapping foil configuration closely resembles an effort to replicate the performance benefits detailed before. Several parameters have been found to dominate the overall hydrodynamic performance based on the tandem interactions: the spacing between wings Kumar and Hu (2011), and the phase-lag in the motion of the moving elements (Rival et al., 2011; Sampath et al., 2020). Several studies have combined both, finding a strong correlation between the spacing/phasing of the wings, and its propulsive performance (Geder et al., 2017; Lua et al., 2016; Younsi et al., 2022; Broering and Lian, 2012; Gravish et al., 2015; Lin et al., 2019). A proper coordination between the two elements of the arrangement can induce large benefits, but, on the other hand, if the phasing/spacing criteria is not tuned, the hind foil can observe a large performance detriment. Muscutt et al. (2017a) analysed the effects of the mentioned phasing/spacing combination at different *St* values, observing that, as the *St* changes, the optimum configuration for the tandem operation changes. The hydrodynamics observed in the previous studies points towards the interactions between the hind foil and the incoming vortices as the reason behind the performance augmentation or detriment. Figure 2.4 (Muscutt et al., 2017a) introduces the jet developed during a tandem operation for a high-performance and low-performance arrangement. The high-performance configuration increases the velocity of the flow and the thrust. While the low-performance foil encounters vortices during its path, leading to low forces production, the high-performance case waves between the main vorticity structures of the wake. By avoiding the vortices, the foil takes advantage of the reverse von Kármán street, without suffering the penalties of strong foil-wake encounters.

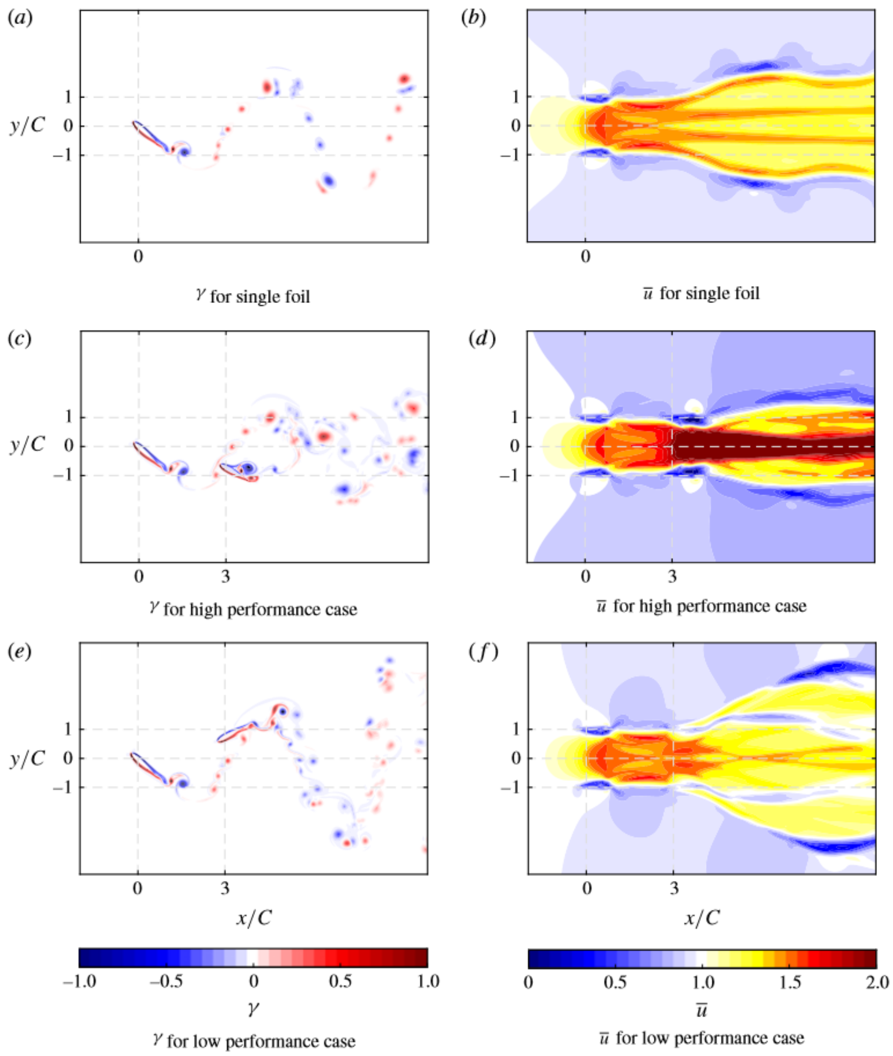

FIGURE 2.4: Wakes of single flapping foil, and a high-performance and low-performance tandem configuration. Muscutt et al. (2017a)

The performance benefits of the tandem operation presented in the previous studies can only be achieved if the optimal conditions are known in advance. If the route that augments the performance is unknown, the tandem operation could not only not provide benefits, but add penalties to the performance of the foil. In this thesis, we aim to develop methods to predict the optimum phasing for a foil, in order to maximise its performance.

2.5 Machine Learning techniques applied to flapping foils.

As described before, a flapping foil swimming inside a tandem arrangement can drastically increase its swimming performance if its motion is properly tuned to incoming wake. We have also discussed that the basis behind the tandem arrangement rely on fish-schooling, which is known to be a highly unsteady scenario. If the upstream conditions change, the foil needs to adjust its trajectory to maintain the performance gains. We believe that, in order to achieve that capability, first the propulsive performance of the foil needs to be predicted in real-time. If the foil can detect in advance a change in the wake conditions, it will be able to adjust accordingly.

Several models have been developed to estimate the performance of a flapping foil. Theodorsen and Mutchler (1935) derived the first expressions for the forces time evolution to predict aerodynamic flutter. Garrick (1936), used the equations defined by Theodorsen to approximate the propulsive forces, and Lighthill (1969) completed the work done by Garrick applying its equations to a lunate tail of a fish. The main disadvantage of the previous methods is that they all assume small amplitude kinematic motions, rectilinear vortex wake and perfect fluid, conditions highly unlikely to be found in a real-world applications.

Several approaches have been conducted to account for the presence of unsteadiness in the incoming flow. Muscutt et al. (2017a) developed a quasi-steady model able to estimate the averaged forces parameters by including the velocity of the wake upstream of the flow. Still, for a real-time application, the force model has to be able to deal with instantaneous forces. Kurt et al. (2020) developed a variation of Garrick (1936) to estimate the performance of the hind foil by including the wake velocity components.

Nowadays, the developments on Machine Learning techniques and system identification tools have opened the path to deal with the complex flow dynamics inside the tandem operation or fish-schooling. For example, Li et al. (2022) were able to predict multiple transient physical fields, transient aerodynamic characteristics of a flapping-based energy extracting device using deep-learning techniques. Zhu et al. (2022a) reported that a swimmer inside dense-schooling formations could learn to maintain stable formations using Deep Reinforcement Learning. Zhu et al. (2022b) used similar tools to train a fish to reach a target destination from random initial locations, by discovering efficient navigation strategies.

By using DRL techniques, Gunnarson et al. (2021) found that a swimmer could exploit the unsteadiness in the surrounding flow. Zhu et al. (2021) trained a fish to adapt its motion to different task, such as prey capture, rheotaxis and Kármán gaiting. Using complex techniques such as Deep Reinforcement Learning can develop promising results able to deal with the highly-unsteady scenario of tandem flapping foils. The same tool was used by Verma et al. (2018), who reported that swimmers can exploit unsteady flow fields to obtain substantial energetic benefits.Still, those methods are usually cost-expensive and difficult to generalise.

In recent years, more work has been done to reduce the computational expense of Machine Learning techniques applied to hydrodynamic scenarios. Weymouth and Yue (2013) studied the applications of physics-based learning models (PBLM) to ship hydrodynamics. By the use of physical knowledge of the system, the authors improved the predictions obtained by simple regression models at a considerably less expense than high-resolution numerical predictions. Another approach gaining relevance nowadays relies on Koopman-Based tools. The Koopman approach aims to represent linearly complex nonlinear dynamical systems, which could lead to prediction, or control applications (Brunton et al., 2021). In this line, Brunton et al. (2016b) proposed the ”Sparse Identification of Nonlinear Dynamics (SINDy) approach. By the use of a generic library of terms, and properly selected inputs, the approach can recover the dynamics of complex systems. The main advantage relies on the sparsity of the discovered governing equations, which could lead to a deeper understanding of the physics of the problem to be studied, as opposed to Machine Learning black-box algorithms, such as LSTM or NODE (Hochreiter and Schmidhuber, 1997; Chen et al., 2018).

In this thesis, we aim to use user-interpretable system identification tools to recover the dynamics of the propulsive performance of a flapping foil inside unsteady incoming flow. By applying physical knowledge to the process, we aim to recover accurate governing equations able to predict the performance of the foil in real time, which could lead to control applications, and to a deeper understanding of the physics behind the performance gains of fish-schooling and tandem operations.

2.6 Applications

The field of application of flapping foils is vast. From energy harvesters to micro-vehicles, the motion presented in the previous chapter can be adapted to many circumstances. Although it is still in a theoretical stage, there are some examples where actual systems have been built. Licht et al. (2004b) designed a vehicle that used flapping foils as a sole source of propulsion. The vehicle was found to be suitable for thrust generation under unstable circumstances. Bandyopadhyay et al. (1997) quantified the gap in manoeuvrability between micro vehicles and fish by the use of a dual flapping device mimicking the dorsal fins of a fish. Long Jr et al. (2006) developed a robot with a configuration consisting of four flippers in order to study the phasing between each of them. The authors found that maximum thrust was achieved when all four flippers were in motion.

In the field of micro air vehicles, Ratti and Vachtsevanos (2011) analysed dragonfly-inspired vehicles. The characteristics of those systems allow them to an important range of applications, such as intelligence and surveillance or border patrol.

Chapter 3

Methodology

3.1 Computational

Computer Fluid Dynamics (CFD) simulations are useful to researchers to conduct large parameter sweep studies at a relatively low cost compared to experiments. In this thesis, numerical simulations have been conducted to develop the database needed to produce force-models and/or optimise trajectories (Chapter 5 and Chapter 6), and as the basis for experiments (Chapter 5). In this section we describe the details of the solver used, we conduct a sensitivity analysis of the grid, and validate the model against existing literature.

3.1.1 Solver

In this thesis we have used a FORTRAN-based CFD solver, called Lotus. This solver has been shown to simulate accurately complex geometries and moving bodies at a various range of Reynolds numbers, in both 2D and 3D domains. This solver uses the Boundary Data Immersion Method (BDIM,Weymouth and Yue (2011)) to simulate the time-evolution of the viscous Navier-Stokes using a convolution over the fluid and any immersed dynamic geometries. The convergence of this method is quadratic, and has been previously validated for flapping foil systems in several studies Maertens and Weymouth (2015); Lagopoulos et al. (2019); Zurman-Nasution et al. (2021a).

3.1.2 Grid analysis

The main characteristics of the grid used in this thesis are similar to the one used by Lagopoulos et al. (2019). Nevertheless, the Re used in this thesis ($Re = 7000$) differs from Lagopoulos et al. (2019) ($Re = 1173$), hence, a full grid sensitivity analysis will be

Points per chord	$\overline{C_X}$	% Error
64	0.455	14%
128	0.414	3.4%
192	0.412	2.9%
256	0.400	0

TABLE 3.1: Grid density study

conducted in order to ensure a correct balance between simulation accuracy and computational cost. The mesh is made of a rectangular cartesian grid, with a dense uniform grid for the areas of interest of the study (body and near wake), and exponential grid-stretching for the far field. The details of the grid are presented at Figure 3.1, extracted from Lagopoulos (2021). The domain consists of uniform inflow, with free-slip conditions on the lower and upper boundaries.

The first analysis to be conducted to ensure the correct setup of the grid is a grid sensitivity study. The mesh density is defined as points per chord (c/X). A more dense approach will lead to more resolved simulations, but at a higher computational cost. To evaluate the optimum balance between accuracy and cost, we perform simulations of a flapping foil swimming at uniform upstream flow ($h/c = 1$, $St = 0.36$, $Re = 7000$) at four different resolutions: 64, 128, 192, and 256 points per chord. To evaluate the sensitivity effects on the resolved forces, we evaluate the $\overline{C_X}$ for all cases and compare it with the highest-density grid (256 points per chord). Assuming the latter as the truth value, we evaluate the relative error achieved with the lower-dense resolutions. Table 3.1 introduces the results of the sensitivity analysis.

Based on the results obtained during the grid sensitivity analysis, and to use a grid configuration that has been validated in previous studies (Lagopoulos et al., 2019), we select a grid spacing of $\Delta X = \Delta Y = c/192$. After selecting the points per chord to be used in the study, the next step is to evaluate the convergence capabilities of the solver. Figure 3.2 introduces the C_X evolution at different cycles achieved by the solver. In line with Lagopoulos (2021), a good convergence is achieved after Cycle 5, highlighting the capabilities of the solver to model moving objects.

3.1.3 Validation

In this section, we validate the solver against existing literature data. As discussed before, LOTUS has been used in multiple studies for different applications. The solver has been validated for a range of $Re = 10^3 - 10^4$ values, for applications varying from towing cylinders Weymouth (2014), vorticity shedding of shrinking cylinders (Weymouth and Triantafyllou, 2012), boundary layer instabilities (Maertens and Weymouth, 2015), and bodies executing rapid manoeuvres Polet et al. (2015). The same code has been

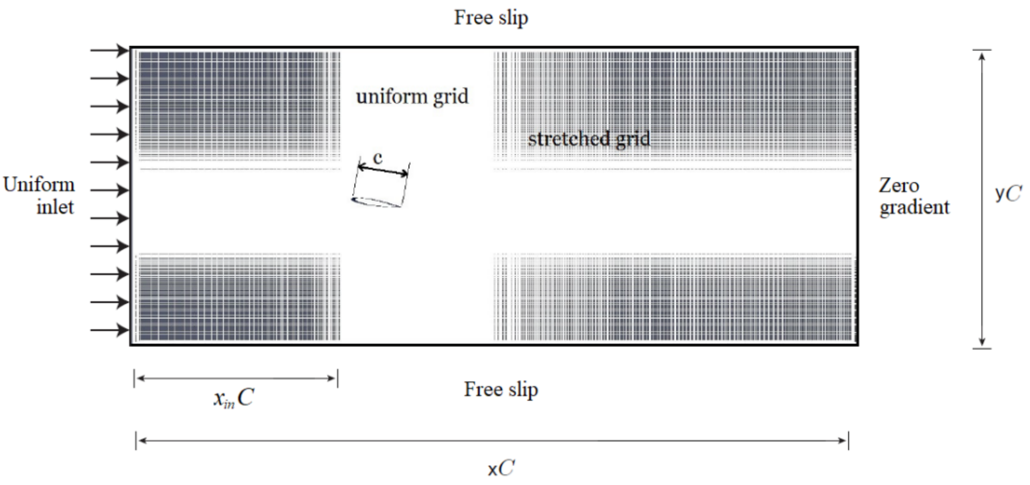

FIGURE 3.1: Schematics of the grid used in this thesis. Extracted from Lagopoulos (2021)

.

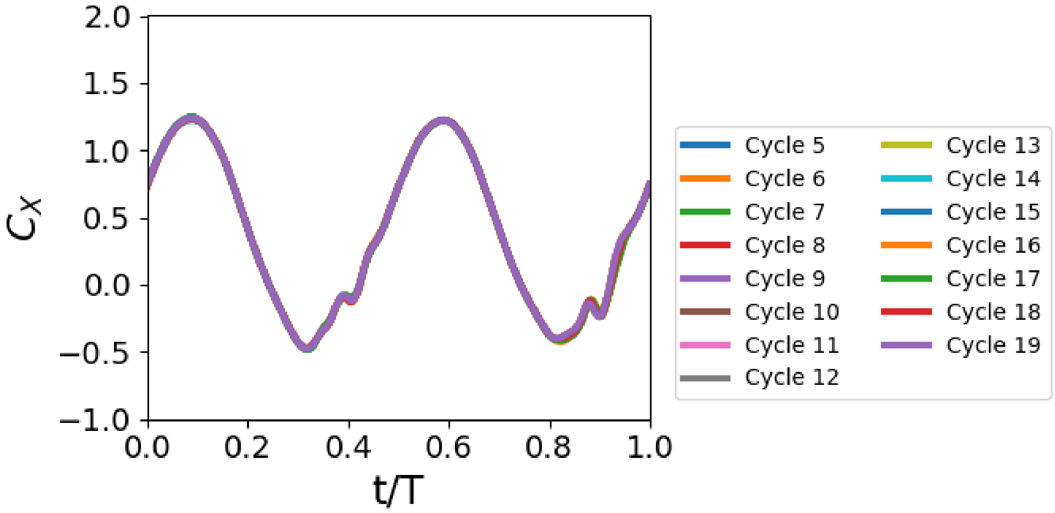

FIGURE 3.2: Analysis of the convergence achieved by the lotus simulations for a grid spacing of 192 points per chord. The figure presents a comparison between the instantaneous C_X produced at consecutive flapping cycles.

used for flapping foil applications, ranging from 2D to 3D, for solo and tandem flapping foils, and with different kinematics: from coupled motions (Muscutt et al., 2017a; Lagopoulos et al., 2020, 2019; Zurman-Nasution et al., 2020, 2021a,b).

We introduce at Figure 3.3 a comparison between the results presented at Anderson et al. (1998) and values obtained using the solver Lotus. We also include at the figure the validation conducted by Muscutt (2017) with a similar solver. As denoted by Muscutt (2017), a good agreement can be seen between the existing experimental data and the simulations conducted with our solver, proving the feasibility of the CFD tool for flapping foil applications.

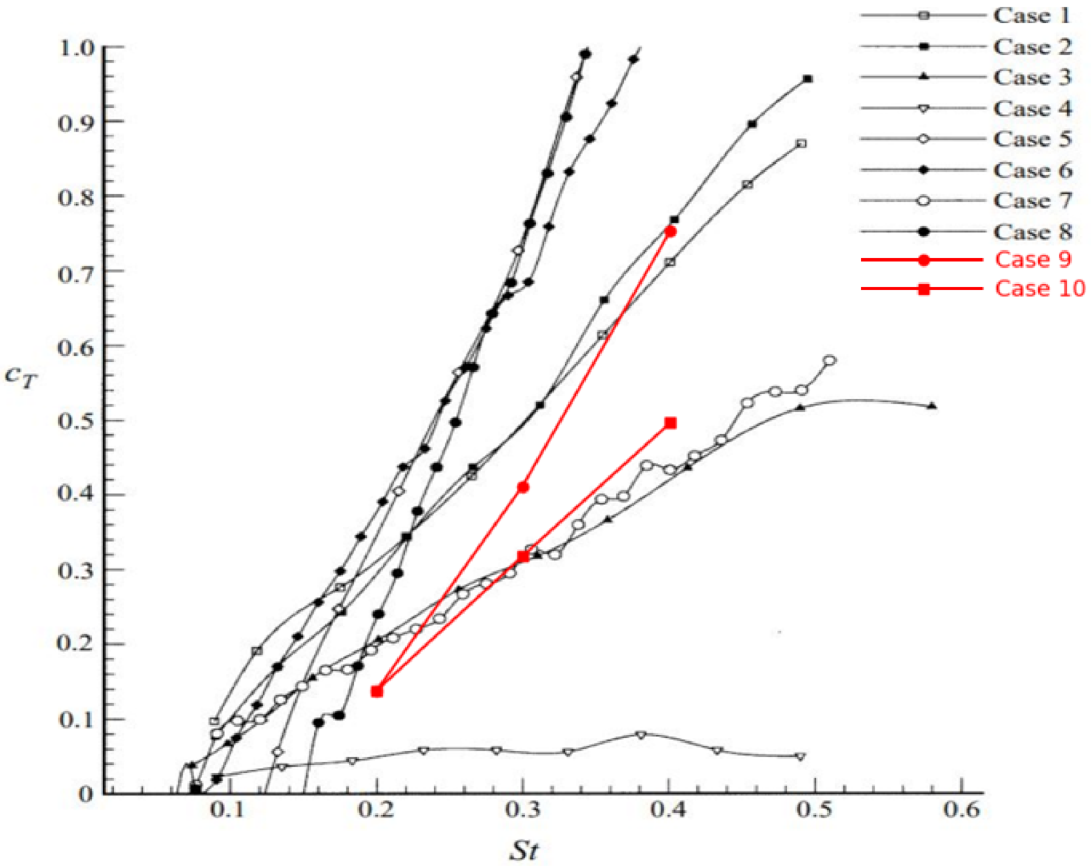

FIGURE 3.3: Comparison between the $\overline{C_X}$ values described by Anderson et al. (1998) for a solo flapping foil (Cases 1-8). Case 9, extracted from Muscutt (2017) follows the same kinematics as Case 5. Case 10 is equivalent to Case 7.

3.2 Experimental

This section introduces the facilities and tools used to conduct the experiments described in this thesis. The experiments have been conducted at the University of Southampton recirculating water flume. The methodology developed in this thesis includes the execution of prescribed motions, the acquisition of forces and locations, and Particle Image Velocimetry (PIV) techniques.

The information presented here will be complemented with the Methodology sections of Chapters 4 and 5

3.2.1 Recirculating water tunnel

The experiments presented in this thesis are conducted in the recirculating water flume in the Department of Aerodynamics and Flight Mechanics, at the University of Southampton. The test section of the flume is 8.1 m length, with a width of 1.2m and a depth of

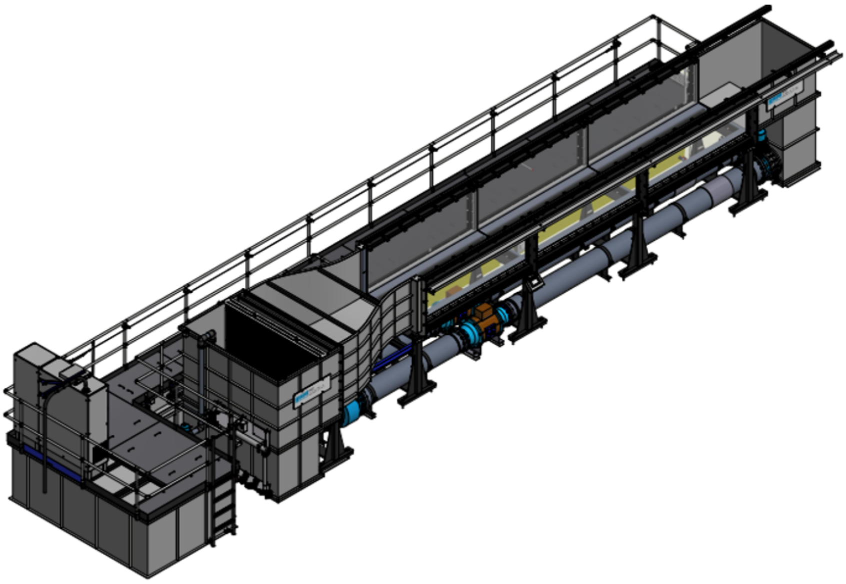

FIGURE 3.4: Schematics of the University of Southampton recirculating water flume.

0.9 m. The flow is driven by two parallel axial propeller pumps that can circulate the water at a maximum velocity of 1m/s.

3.2.1.1 Experimental flapping equipment

The flapping experiments are conducted using a modified version of the ’robotic plesiosaur’ designed by Muscutt (2017). The system is installed on top of the recirculating water flume, and can provide two axes of motions for two different flippers, one for pitching and one for heaving. The system contains two traverse bars located across the water flume that execute the heaving motion through the use of a stepper motor (Applied Motions STM32R) and a belt. The system is designed so that it can hold the foil, and the equipment needed to execute the pitching motion and acquire forces and locations. The schematics of the flapping carriage are presented at Figure 3.5.

3.2.1.2 Flapping arm

A flapping arm has been designed and built to execute the pitching motion of the foils, as depicted at Figure 3.6. The arm is capable of following a prescribed kinematic, and to record the instantaneous location and forces produced by the foil. Two different sets of steppers have been used in this thesis. The experiments described at Chapter 4 were done with an Applied Motions STM23S, while the tandem motion detailed at Chapter 5 is executed with an Applied Motions STM32R. A gear-box (ratio 5:1) is coupled with the stepper to increase the torque and resolution of the motion. The attitude of the foil, both the heaving and pitching trajectories, is recorded using encoders, as depicted

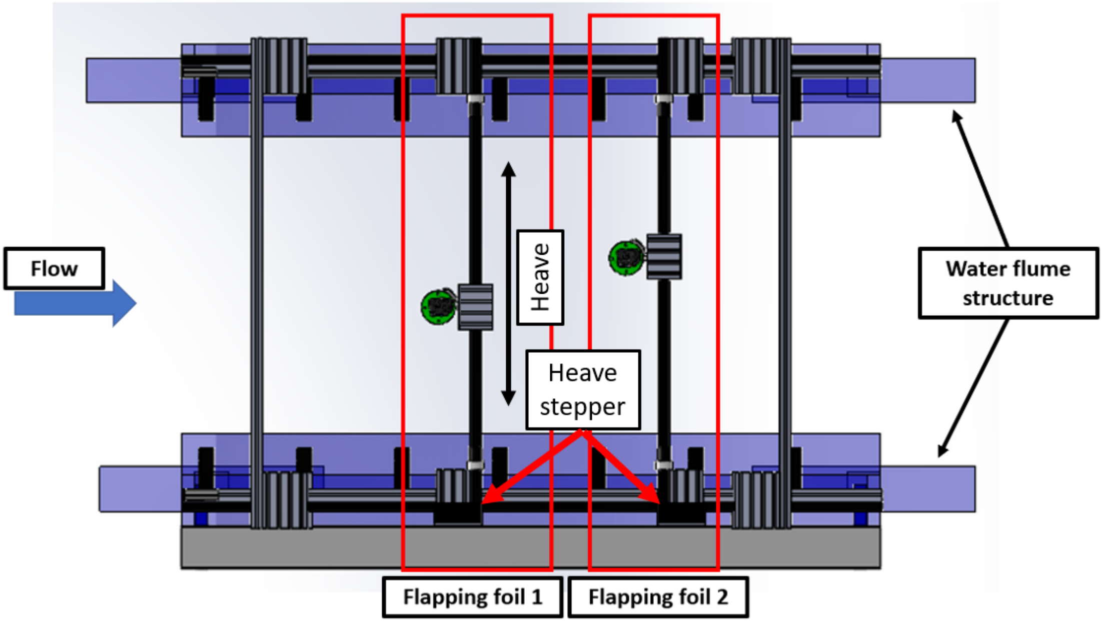

FIGURE 3.5: Schematic of the flapping carriage used to perform the heaving/pitching motions.

at Figure 3.6. The pitching motion of the foil is captured using a rotary incremental encoder (US Digital E5) attached to the motor shaft. The resolution of the encoder is 5000 cycles per revolution. The heaving displacement is acquired using a SoftPot membrane potentiometer located in a transversal bar, normal to the direction of the flow. A wiper is placed in the flapping arm to capture the instantaneous lateral location of the foil.

The forces and moments that act on the foils are measured with a six-axis force sensor (ATI Gamma IP65). The load-cell provides a resolution of $1/80N$ in the X, Y axes, $1/40N$ in the Z axis, $10/13333Nm$ in the X,Y, Z moments, for a maximum load of 65 N in the X,Y axis, 200 N in the Z axis, and 5Nm for the X,Y,Z moments. The forces and moments are calibrated using the calibration file provided by ATI for the specific load cell utilised. All the experiments are repeated several times to report errors in the data. Finally, a surface plate is installed at the foil tip and the foil is placed right above the bottom wall to prevent tip vortex formation and enforce nominally two-dimensional flow over the foil.

3.2.2 Kinematics control and forces acquisition

The core of the experimental setup relies on the control system used to prescribe and execute the motion, and to acquire the instantaneous forces and locations. Two different systems have been used during this thesis to perform such task. For Chapter 4, we have developed an approach using MATLAB environment. The data described at Chapter 5

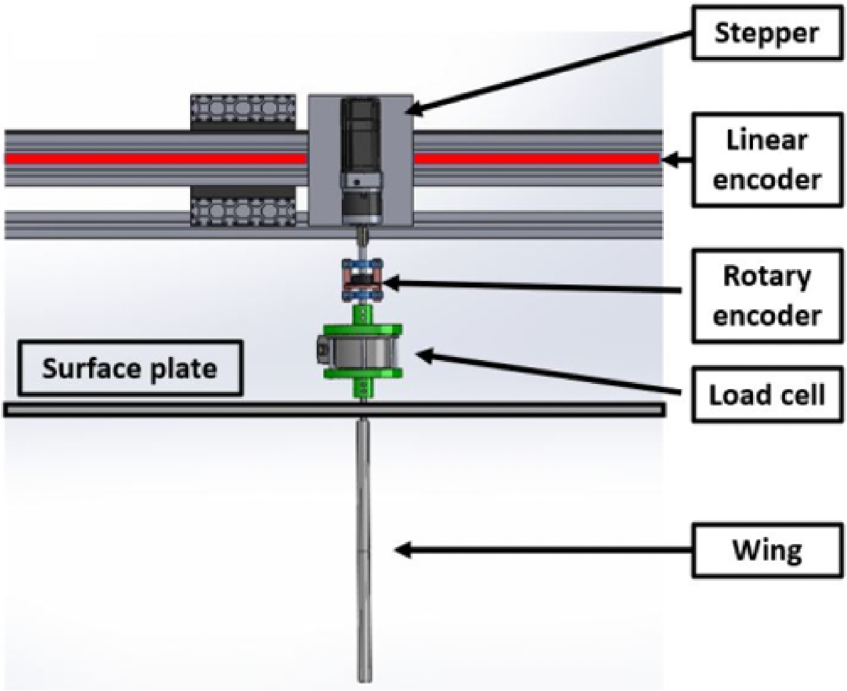

FIGURE 3.6: Schematics of the flapping arm built for this thesis.

has been acquired with a combination of the mentioned new MATLAB code, and the existing Labview-based cRio environment.

3.2.2.1 cRIO

An existing Labview-based control system, has been adapted to accommodate the requirements of this thesis. The system uses a CompactRIO (cRIO) 9067 chasis (National Instruments), which comprehends a real-time processor with reconfigurable field programmable gate array (FPGA). The chasis contains a total of 8 slots that can house various modules, based on the requirements of the study. The structure of the cRIO is depicted at Figure 3.7, extracted from Muscutt (2017). The original system was able to control and execute two axis of motion for a set of two flippers, and to acquire forces from a gauge-cell. The system was further developed to accommodate linear encoders, and a six forces and moments ATI load cell. This experimental capability was used to prescribe the motion of the foils detailed at Chapter 5. The forces and encoders data were acquired with a MATLAB code that will be introduced next.

3.2.2.2 SCL protocol

The second control system has been developed using a MATLAB environment, and Serial Command Language (SCL) protocol. The SCL is able to control aspects such as the location of the stepper, or the velocity and acceleration of the motion. The kinematics

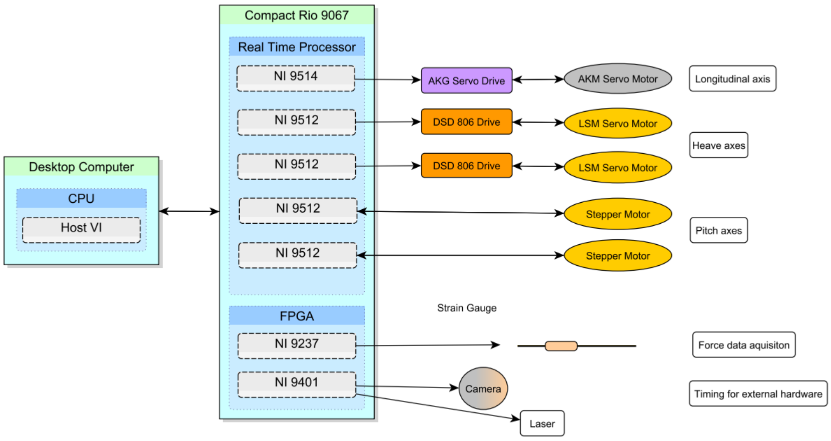
Compact Rio 9067
Real Time Processor
NI 9514
NI 9512
NI 9512
NI 9512
NI 9512
FPGA
NI 9237
NI 9401
Desktop Computer
CPU
Host VI
AKG Servo Drive
DSD 806 Drive
DSD 806 Drive
AKM Servo Motor
LSM Servo Motor
LSM Servo Motor
Stepper Motor
Stepper Motor
Longitudinal axis
Heave axes
Pitch axes
Strain Gauge
Force data aquisiton
Camera
Timing for external hardware
Laser

FIGURE 3.7: Schematics of the original labview-based cRio control system, extracted from (Muscutt, 2017)

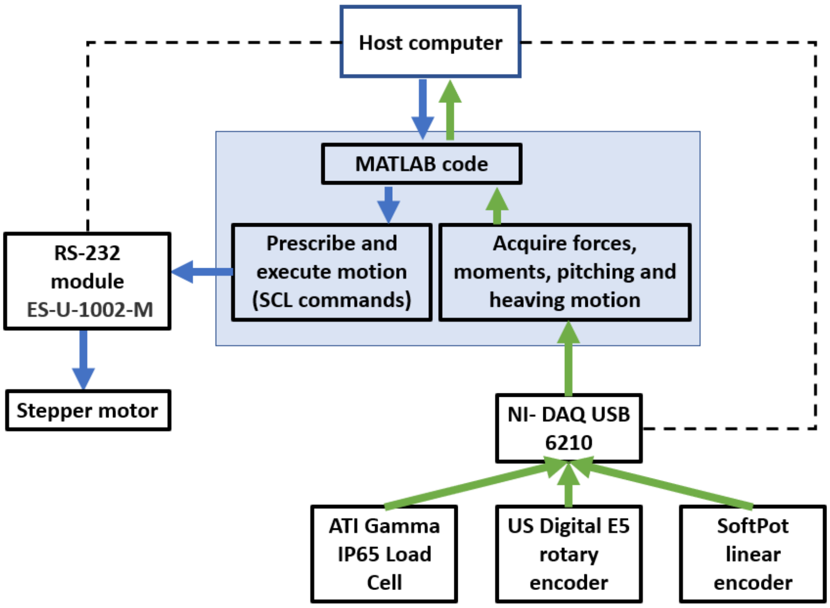
Host computer
MATLAB code
Prescribe and execute motion (SCL commands)
Acquire forces, moments, pitching and heaving motion
RS-232 module ES-U-1002-M
Stepper motor
NI- DAQ USB 6210
ATI Gamma IP65 Load Cell
US Digital E5 rotary encoder
SoftPot linear encoder

FIGURE 3.8: Schematics of the MATLAB-based SCL control protocol.

signal are divided into steps and sent from a host computer (MATLAB code), through a RS-232 module (ES-U-1002-M) to the driver of the stepper. The MATLAB code communicates through a NI-DAQ USB 6210 with the encoders and load cell and records in real time the forces and locations of the foil. The schematics of the system are presented at Figure 3.8 This protocol has been used to carry out the experiments (motion and data acquisition) conducted at Chapter 4 and to acquire the forces and data of the experiments conducted at Chapter 5.

3.2.3 PIV techniques

The MATLAB code presented in the previous section was able to communicate with a PTU LaVision system to perform simultaneous forces acquisition and Particle Image Velocimetry (PIV) techniques. For the experiments conducted at 4, we conducted flow measurements using a planar PIV system. The cameras used for the experiments were two 4-megapixel *LaVision MX* with 50 mm *Nikon* lenses ($f = 5.6$). Both cameras were placed underneath the water channel. The distances between the bottom wall of the channel and the cameras was around 80 cm. The arrangement of the cameras was side-by-side, in the streamwise direction, to capture a field-of-view of about $2c \times 1c$ with $0.2c \times 1c$ overlap between the camera frames. The field-of-view was aimed to obtain images of the entire cross-section of the foil, and an additional $0.5c$ in the foils' upstream and downstream regions. The field of view was illuminated using a laser beam output by a *Litron Nano PIV* laser head with 200 mJ power output at 532 nm wavelength, through a set of sheet-forming optics at the foils' mid-span. The laser and camera triggers was synchronised using a pulse timing unit (PTU) via *DaVis 10* software to record the image pairs. The flow was seeded with polyamide particles with a nominal diameter of 55 μm. The seeding density was iteratively adjusted to have a satisfactory number of particles in the field of view. The image pairs were captured at full resolution (2048 × 2048 pixels) at a frequency of 10 Hz. To cross-correlate the image pairs, the software *DaVis 10* was used, with the final interrogation window size of 24×24 pixels and 50% overlap. The acquired velocity fields from each camera were combined and blended using half a Hamming window over the overlapped region.

3.3 Machine learning and System Identification techniques

In this thesis, we will use several system identification and Machine Learning tools in an effort to better understand the dynamics of a flapping foil under unsteady conditions system. We will explore several approaches, ranging from black-box algorithms (LSTM, NODE), to user-interpretable approaches (SINDy). The contents detailed in this section will be used to predict the forces experienced by a flapping foil for a given route inside the incoming wake (Chapter 5 and Appendix A)

3.3.1 Machine Learning tools

This section introduces the techniques used to recover and predict the forces experienced by a flapping foil immersed inside unsteady incoming flow, and the optimisation tools selected to find optimum manoeuvring methods.

The Long Short-Term Memory (LSTM) method, developed by hochreiter1997 is suitable for this analysis as it can pass the information obtained at a given state, or $x(t)$ to the next iteration. By doing so, it can estimate the state of a given parameter at a $(t + \Delta(t)$ time step, what makes the model suitable for predictive - and manoeuvrability - applications.

The LSTM model, developed using the package Keras Chollet et al. (2018), is trained using pieces of the time-signal inputs, also known as windows, where the goal is to predict the state of the same inputs, but ahead in time.

3.3.1.1 Neural ODE

The Neural Ordinary Differential Equations (NODE) approach, developed by Chen et al. (2018) obtains an output layer solution by solving an ODE initial value problem with the use of a black-box differential equation solver.

Neural ODEs are a suitable application for time series prediction, especially when the data is irregularly sampled or insufficient Rubanova et al. (2019). Although that is not the case of our study, where all the time signals are made up of equally-spaced time steps, recent work has proved that it could provide a better estimation to forces signal than the LSTM. Following the work done by Chen et al. (2018), an encoder-decoder ODE network has been used in order to predict, like in the LSTM section, the states of several physical parameters ahead of time. The model has been developed using the package TorchDiffEq Chen et al. (2018). Due to the approach followed on this research, most of the characteristics of the network are kept similar to those presented at Chen et al. (2018). Also, and to keep consistency with the LSTM approach, a sweep in the ODE layer hidden-units has been made. Finally, no dropout layer has been applied, as it has been found that it does not adapt properly to neural ODE networks Liu et al. (2019a).

3.3.2 System identification

3.3.2.1 Sparse Identification of nonlinear Dynamics (SINDy)

The last machine learning method that is going to be used in this study is the Sparse Identification of Nonlinear Dynamics (SINDy) Brunton et al. (2016b). This approach aims to discover governing equations from measured data and, by assuming that only a few important terms govern those dynamics, SINDy uses sparse regression in order to output user-interpretative models. By doing so, it can overcome one of the main disadvantages of black box algorithms which, although can provide accurate answers in terms of controlling and manoeuvring performance estimation, do not provide a great amount of physical knowledge in return due to the characteristics of their output models.

The use of SINDy requires the selection of inputs to recover the governing equations of the system. In this thesis, we will develop several models to analyse how, by adding physically-relevant information, the accuracy of the models can increase. The package *PySINDy* de Silva et al. (2020) has been used.

Chapter 4

Effects of surface roughness on the propulsive performance of pitching foils

University of Southampton

Abstract

Faculty of Engineering and Physical Sciences
School of Engineering

Doctor of Philosophy

Flow past flapping foils:
Surface texture and unsteadiness effects

by Rodrigo Vilumbrales Garcia

The hydrodynamic influence of surface texture on static surfaces ranges from large drag penalties (roughness) to potential performance benefits (*shark-like skin*). Although it is of wide-ranging research interest, the impact of roughness on flapping systems has received limited attention. In this work, we explore the effect of roughness on the unsteady performance of a harmonically pitching foil through experiments using foils with different surface roughness, at a fixed Strouhal number and within the Reynolds number (Re) range of $17,000 - 33,000$. The foils' surface roughness is altered by changing the distribution of spherical-cap shaped elements over the propulsor area. We find that the addition of surface roughness does not improve the performance compared to a smooth surface over the Re range considered. The analysis of the flow fields shows near identical wakes regardless of the foil's surface roughness. The performance reduction mainly occurs due to an increase in profile drag. However, we find that the drag penalty due to roughness is reduced from 76% for a static foil to 16% for a flapping foil at the same mean angle of attack, with the strongest decrease measured at the highest Re. Our findings highlight that the effect of roughness on dynamic systems is very different than that on static systems, thereby, cannot be estimated by only using information obtained from static cases. This also indicates that the performance of unsteady, flapping systems is more robust to the changes in surface roughness.

4.1 Introduction

Surface roughness is ever-present in engineering applications, involving complex fluid-structure interactions. Its implications on the flow and the consequent drag generation have been widely studied in the related literature. From the influence of roughness in pipe flow (Achenbach, 1971), to its effects on the trajectory of a golf ball (Chowdhury et al., 2016), roughness plays a vital role in any application involving fluid-structure interaction considerations. For example, surface roughness can be detrimental to the performance of wind turbines. Sagol et al. (2013) found that the accumulation of contamination agents in the blades leads to a reduction in power extraction, while Ehrmann et al. (2017) reported a performance decrease linked to an increase in roughness density and height. On the other hand, the use of roughness elements can lead to a drag reduction and certain performance gains for unsteady propulsion systems. Previous studies inspired from swimmers and flyers show that, from shark skin (Dean and Bhushan, 2010) to feathers on a wing of a gliding bird (Van Bokhorst et al., 2015), roughness in varying shapes and texture modifies the fluid flow over propulsor surfaces, leading to a reduction in drag or a decrease in flow separation. In engineering applications, Gad-el Hak and Bushnell (1991) analysed the effects of roughness turbulators and found an increase in the ratio between the lift and the drag coefficient when compared to a smooth foil for chord based Reynolds number lower than $100,000$. Also, the use of surface riblets can lead to a decrease in skin friction when aligned in the flow direction (Bechert et al., 1997), achieving a drag reduction of up to 8% (Walsh, 1982). An important roughness parameter to consider is the roughness Reynolds number H^+, defined as $H^+ = Hu_\tau/\nu$ where H is the height of the rough element, ν is the kinematic viscosity, and u_τ is the friction velocity. For H^+ values less than 70, the flow is usually characterised as transitionally rough. When $H^+ > 70$, the rough elements extend into the logarithmic region, the smooth-wall viscous sublayer is assumed to have been completely destroyed and the surface is considered to be fully rough (Bakken et al., 2005).

Recent studies have analysed the effects of superhydrophobic coating on the surface of pitching foils. Mallah et al. (2021) reported an increase in the lift and thrust production for a pitching foil at low Strouhal values when compared to a smooth foil, which could lead to improved manoeuvrability and propulsive efficiency.

When configured properly, surface roughness can be beneficial. It can reduce drag production and potentially improve the overall performance. Surface roughness can also have detrimental effects. Tailoring the surface roughness to have an improved performance requires a better understanding of the effect of shape, size, and area distribution of roughness elements on both the force production and the flow.

The drag-reduction potential of surface roughness on aquatic swimmers have been explored mainly for static surfaces. For example, sharks can reduce their skin friction when their riblets are aligned with the flow (Dean and Bhushan, 2010). Bixler and

Bhushan (2013) pointed out that the riblets lift and pin the vortices generated in the viscous sublayer, leading to a decrease in drag. Bechert et al. (2000) observed a drag reduction for interlocking 3D riblets. Afroz et al. (2016) concluded that 'shark-like' textures can act like a passive flow separation control mechanism. Du et al. (2022) found smaller separated regions and adverse pressure gradients for the flow over a foil covered with tilted biomimetic shark scales. The effect of the shape and size of the rough elements were analysed by Domel et al. (2018a), highlighting the importance of the denticle shape, as they found a drag reduction only for the smaller of the three considered. Although surface roughness has shown promising potential for static bodies, its role in unsteady systems is still not clear. Shark-skin surfaces have been shown to increase the self-propelled swimming speed and reduce the drag of a flapping foil (Oeffner and Lauder, 2012; Domel et al., 2018a), but only when small denticles are used, whereas the larger elements can lead to an increase in drag. Wen et al. (2014) reported a reduction in energy consumption due to a formation of stronger leading-edge vortices. Guo et al. (2021) found that, for static foils towed at a constant velocity, the roughness elements resulted in a considerably thicker boundary layer when compared to the smooth foil, while, for static foils in acceleration, the changes due to roughness in the wake characteristics were considerably smaller. Mostly, previous work concludes that shark-inspired surfaces can improve the performance of an unsteady body, but the potential benefit is strongly dependent on the shape and size of shark denticles, which often appear in highly complex geometries. Therefore, it is still to be seen if such performance improvement can be achieved with simple, commercially available roughness elements, located on the surface of an unsteady foil in harmonic motions.

In this study, we analyse experimentally the effects of surface roughness on the propulsive performance of a pitching foil by using simple roughness elements. In Section 2, we define the methodology and experimental setup used to actuate three different foils with varying roughness characteristics. We investigate the effects of chord-based Reynolds number in the range of $17,000 \leq Re \leq 33,000$ and report the propulsive performance of a pitching hydrofoil in terms of thrust production (C_X) and efficiency (η). In Section 3, we detail the force and flow measurement results obtained for flapping foils, and draw a comparison between dynamic and static foil cases.

4.2 Experimental setup and methodology

Force and flow measurements are conducted in a recirculating water flume at the University of Southampton, with a test section of 8.1 m length, 1.2m width and 0.9m depth. A surface plate is installed at the foil tip and the foil is placed right above the bottom wall to prevent tip vortex formation and enforce nominally two-dimensional flow over the foil as shown in Figure 4.1A.

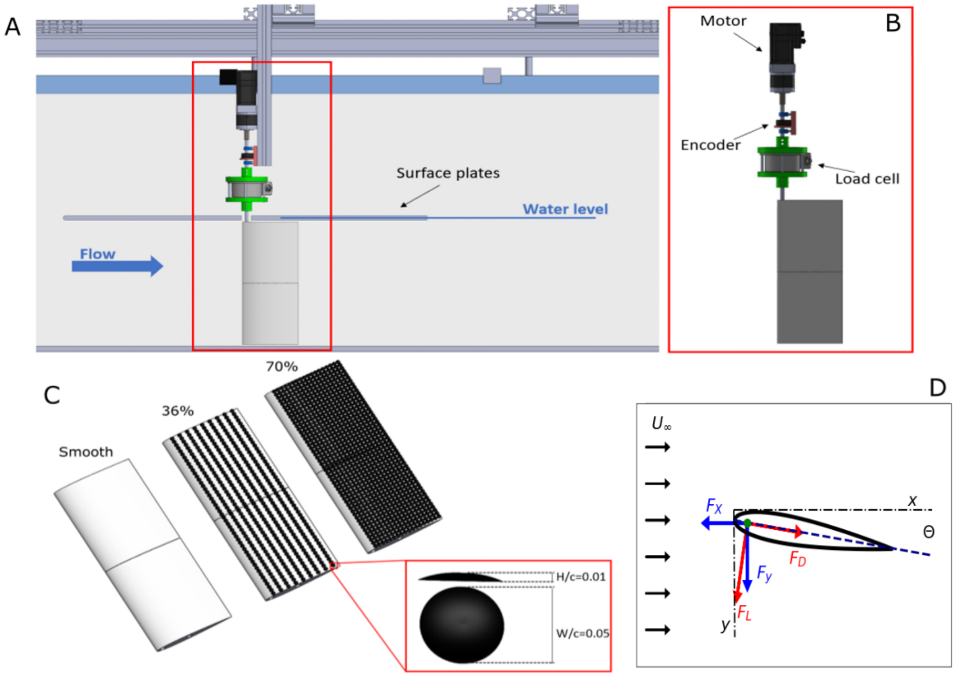

FIGURE 4.1: Schematics of the experimental setup in the water flume (A), the actuation arm (B), foils with three different roughness area coverage ratio (C), and the forces acting on the foil (D).

Three foils with a rectangular planform and a NACA0012 cross-section were 3D-printed using PolyLactic Acid (PLA) filaments with an infill density of 70%, a chord-length of $c = 0.16m$ and an aspect ratio of $AR = 2.5$. Spherical-cap shaped roughness elements with a width (diameter) of $W = 0.05c$ and height of $H = 0.01c$ (Domel et al., 2018b) were placed on pressure and suction sides of the foils. As shown in Figure 1C, in addition to the smooth foil, two different roughness levels are considered by varying the area occupied by the spherical-cap elements to 36% and 70% of the foil planform area. The rough elements were distributed in uniform streamwise rows on both sides of the foil to ensure symmetry, with the amount of rough elements designed to achieve the coverage areas defined before.

Each foil was actuated with a stepper motor (Applied Motions STM23S) in sinusoidal pitching motions, about a point $0.08c$ distance from the leading edge. The prescribed motion is defined by $\theta(t) = \theta_0 sin(2\pi f_0 t)$, where θ_0 is the pitching amplitude and f_0 is the flapping frequency. The pitching amplitude θ_0, Strouhal number $St = 2Af/U_\infty = 2csin(\theta_0)f_0/U$, where A is half the amplitude of the trailing-edge motion, and reduced frequency $k = 2\pi f_0 c/U$ were fixed all throughout the experiments at $\theta_0 = 7.5^\circ$, $St \approx 0.22$ and $k \approx 5.2$, in line with previous studies (Mackowski and Williamson, 2015; Senturk and Smits, 2019; Kurt and Moored, 2018; Fernandez-Feria and Sanmiguel-Rojas, 2020). A Reynolds number sweep ($Re = Uc/\nu$ where ν is the kinematic viscosity) was conducted within the range of $17,000 \leq Re \leq 33,000$ by varying the flow velocity, U. It

Re	17,000	22,000	28,000	33,000
U [m/s]	0.12	0.15	0.19	0.23
f_0 [Hz]	0.62	0.80	1.00	1.20
θ_0 [°]	7.5	7.5	7.5	7.5

TABLE 4.1: Experimental parameters used in the current study

has been reported in previous studies (Senturk and Smits, 2019) that Re can have a major impact on the propulsive performance of a pitching foil, although as Re is increased over $Re = 16,000$ the thrust production appears to reach a constant value. A summary of the parameters used in this study is given in Table 4.1.

The forces and moments acting on the foils were measured with a six-axis force sensor (ATI Gamma IP65). The motion was tracked using a rotary, incremental encoder (US Digital E5) attached to the motor shaft (Figure 4.1 B). Each trial was conducted for a total of 100 flapping cycles (where $t/T = 1$ cycle) and repeated five times. The measured forces were filtered using a Butterworth filter with a low-pass frequency of seven times the flapping frequency. The power was calculated as a multiplication of the pitching moment and the angular velocity, which was derived from the measured angular displacement. The instantaneous and time-averaged performance metrics are the average values from 500 flapping cycles, measured over five trials ($N = 5$). The confidence intervals are calculated following a t-distribution with 5 samples, as $\overline{x} \pm 4.60\sigma/\sqrt{N}$, where $\overline{x}$ is the sample mean, σ is the sample standard deviation, and N corresponds to the number of repetitions (five). To distinguish instantaneous forces from time-averaged results, the latter is denoted by $\overline{(.)}$. instantaneous forces meassured by the load cell (F_L and F_Y) are projected onto the normal and streamwise component (F_X, F_Y), as defined by 2.5. The reported streamwise force (thrust) (C_X) and power (C_P) coefficients, and efficiency (η) are defined as,

$$C_X = \frac{F_X}{\frac{1}{2}\rho U^2 sc}, \qquad C_P = \frac{P}{\frac{1}{2}\rho U^3 sc}, \qquad \eta = \frac{C_X}{C_P} \tag{4.1}$$

where ρ is the density of water, s is the hydrofoil span, and U represents the free-stream flow velocity.

The force measurements were synchronised with planar Particle Image Velocimetry (PIV) measurements (cameras: *LaVision MX 4MP*, lasers: *Litron Nano PIV*). The field-of-view captures the entire foil and up to one chord-length in foil's wake. The software *Davis 10* was used to cross-correlate the acquired particle image pairs (with 24×24 pixels with 50% overlap). The flapping cycle was divided into twenty-two phases, and twenty-five cycles were acquired per phase. The velocity fields corresponding to each phase were then averaged over 25 cycles.

4.3 Results

4.3.1 Flow-field and force production analysis of foils with different roughness area coverage ratios

Figure 4.2 compares the out-of-plane vorticity and the instantaneous performance coefficients, C_X and C_P for all the roughness cases considered at $Re = 28,000$. The first column (A,D), the second column (B,E) and the third column (C,F) present the evolution of the vorticity field around three pitching foils with 0%, 36% and 70% surface roughness at $t/T = 0.15$, and $t/T = 0.50$, respectively. Surprisingly, change in the roughness does not lead to any significant alteration in the vorticity fields. Regardless of the roughness coverage, all foils produce a reverse von Karman-street where two counter-rotating vortices per flapping cycle are shed from the trailing edge into the wake, as widely observed in the related literature for smooth foils (Muscutt et al., 2017a; Kurt and Moored, 2018; Schnipper et al., 2009; Anderson et al., 1998). Figure 4.2 G-H presents the evolution of cycle-averaged thrust and power coefficients over one flapping cycle. Similar to the flow fields, the performance coefficients show only minor differences between the smooth foil and the foils with roughness. Although we have only revealed the analysis associated with a single Re, these results hold across the Re range considered here. Overall, these results from force and flow field measurements show that incorporating surface roughness does not have a strong influence on the development of the wake. Other parameters, such as Strouhal number or kinematics (Schnipper et al., 2009), are known to significantly affect the evolution of the vortex structures, which can minimise the adverse effects on performance induced by the roughness elements.

Figure 4.3 introduces the spectral analysis conducted for the raw, pre-filtered C_X forces. The power spectra of the thrust force at $Re = 28,000$ is shown in (A). The crosses indicate the location of the peak frequency for each foil. In (B), we introduce the dominant frequency ratio in the form of f/f_0, where f_0 is the prescribed pitching frequency across the Re range considered. This analysis shows that the dominant frequency in thrust production corresponds to two times the pitching frequency f_0 for all the Re values and contains similar energy density for all the foils. This result, combined with the similarities observed in both the wake and the instantaneous forces, indicates that the performance of the foils is highly dominated by f_0, hence, by the kinematics. The dominant effects of the frequency and the kinematics on the development of the propulsive forces have been seen before. For example, Zurman-Nasution et al. (2021b) found that, compared to the flapping frequency and kinematics, shape-related parameters such as sweep angle have negligible effects on the propulsive performance. We believe that the influence of the rough elements is small compared to the effects that the kinematics and St have on the C_X and C_P evolution.

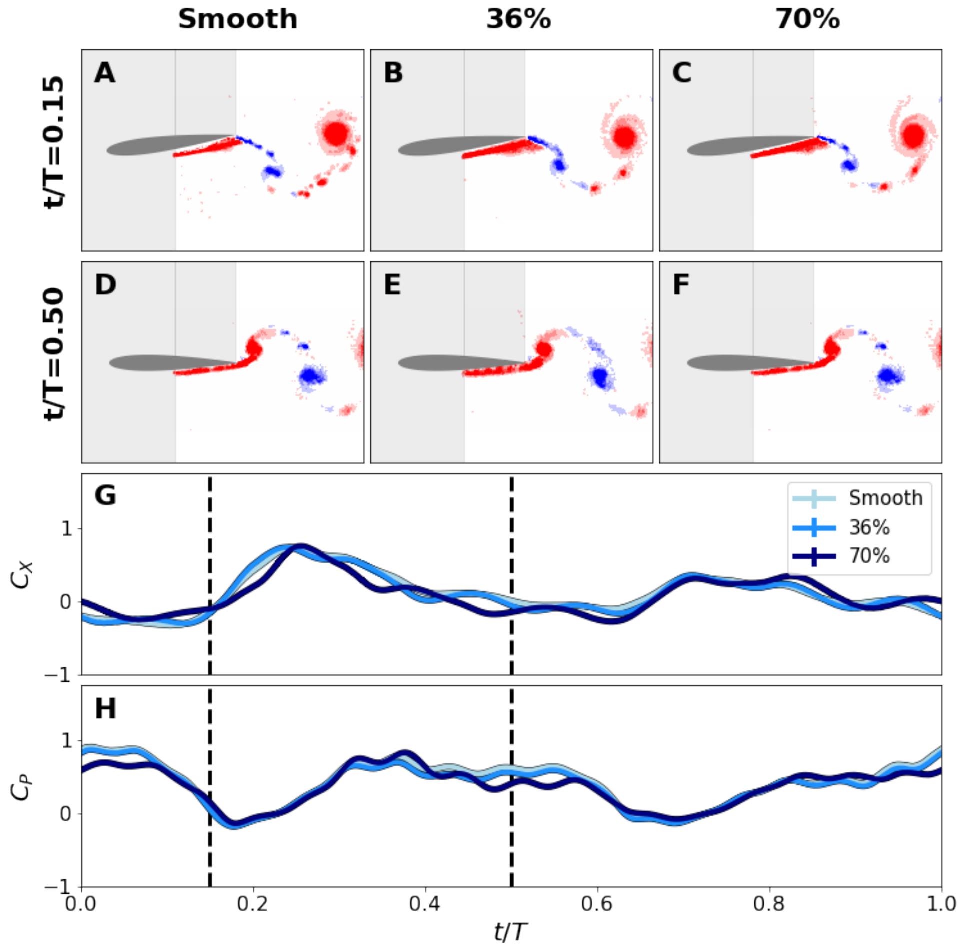

FIGURE 4.2: PIV results for $Re = 28,000$. $t/T = 0.15$ (A,B,C) and $t/T = 0.50$ (D,E,F) for the Smooth (A,D), 36% (B,E) and 70% (C,F). Instantaneous C_X (G) and instantaneous C_P (H). Figure 2 (G,H) contains confidence intervals calculated as $CI = 4.6\sigma/\sqrt{N}$.

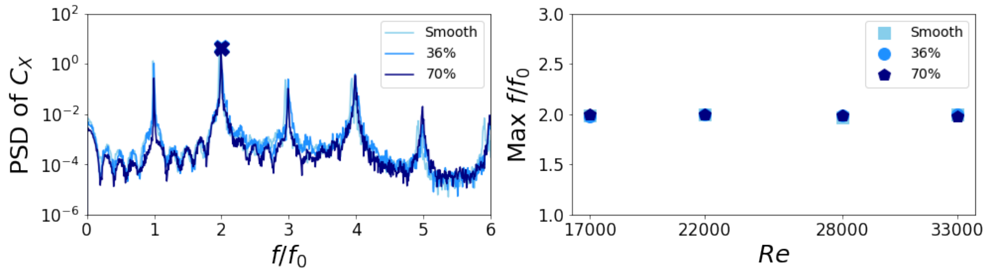

FIGURE 4.3: (A) Power Spectral Density (PSD) analysis of the instantaneous C_X at $Re = 28,000$. The cross indicates the location of the peak for each case. (B) Peak frequency across the Re values considered. A value of 2 denotes that the thrust force signal peak f is equal to two times the input pitching frequency f_0.

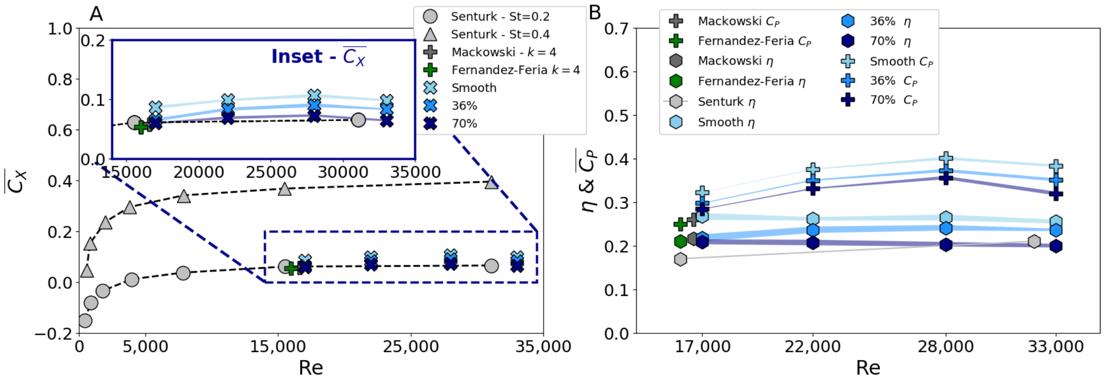

FIGURE 4.4: A) $\overline{C_X}$ obtained in the current study (red range) and compared with previous studies against Re: Senturk and Smits (2019) (gray). The data enclosed by the blue box presents an inset of $\overline{C_X}$ data for the Re range of $17,000 \leq Re \leq 33,000$. B) $\overline{C_P}$ results (hexagon) and η (cross) for current and previous studies: Mackowski and Williamson (2017) (dark-gray) for $Re = 16,600$, $k = 4$, $PP = 0c$ and $\theta_0 = 8^o$. Senturk and Smits (2019) (gray) for $500 \leq Re \leq 32,000$, $St = 0.2 - 0.4$, $PP = 0.25c$, $\theta_0 = 8^o$. Fernandez-Feria and Sanmiguel-Rojas (2020) for $Re = 16,000$, $k = 4$, $PP = 0c$ and $\theta_0 = 8^o$. The shadow region introduces the confidence intervals calculated as $CI = 4.6\sigma/\sqrt{N}$.

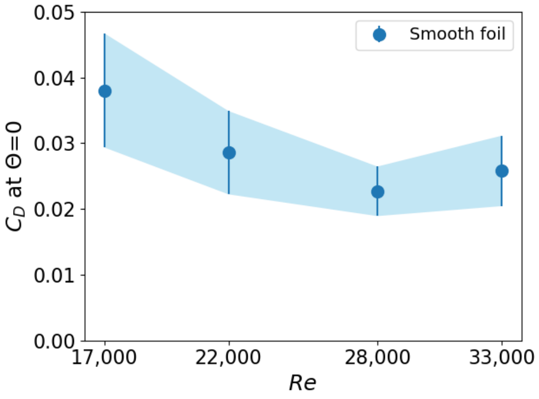

FIGURE 4.5: Averaged C_D values obtained for a static smooth foil at $\theta = 0^o$. The shadow region introduces the confidence intervals calculated as $CI = 4.6\sigma/\sqrt{N}$.

Figure 4.4 presents the change in cycle-averaged performance coefficients for foils with different roughness coverages against Re. We compare our results with other NACA0012 studies conducted by Mackowski and Williamson (2017) ($Re = 16,600$, $k = 4$), Senturk and Smits (2019) ($500 \leq Re \leq 32,000$, $0.2 \leq St \leq 0.6$), and Fernandez-Feria and Sanmiguel-Rojas (2020) ($Re = 16,000$, $4 \leq k \leq 60$). The thrust, $\overline{C_X}$, obtained for the smooth foil increases in the $17,000 \leq Re \leq 28,000$ range, in line with previous studies (Senturk and Smits, 2019). The trend then reverses at $Re = 33,000$. This change can be explained by looking at the evolution of the averaged-drag C_D calculated for a static foil at $\theta = 0$ (Figure 4.5), where we observe a similar behaviour. The raise in the averaged C_D at $Re = 33,000$ explains the decrease in $\overline{C_X}$ reported for the pitching foil at Figure 4.4. Nevertheless, the thrust values obtained in the current study fall within the findings by Senturk and Smits (2019) at $St = 0.2$ and $St = 0.4$. The main differences in the overall thrust production - higher in our study - can be associated with the effects of the pivot point (PP) location ($PP = 0.08c$ here, and $PP = 0.25c$ at Senturk and Smits (2019)), since as the PP moves towards the leading edge, a higher thrust production is expected (Mackowski and Williamson, 2017). Finally, in the inset enclosed by a blue box, it is shown that $\overline{C_X}$ decreases consistently with the addition of surface roughness across the Re range. In Figure 4.4B we introduce the averaged power $\overline{C_P}$ and efficiency η. For each roughness case, $\overline{C_P}$ increases in the $17,000 \leq Re \leq 28,000$ range. The trend is then reversed, in line with the $\overline{C_X}$ values. Regardless of the Re, we observe that an increase in roughness causes a decrease in $\overline{C_P}$. About the efficiency, our results indicate higher η values than Mackowski and Williamson (2017), Fernandez-Feria and Sanmiguel-Rojas (2020), and Senturk and Smits (2019), which could be due to differences in the pivot point location (at $x/c = 0.08$ distance from the leading edge in our study, and at $x/c = 0.25$ distance in Senturk and Smits (2019)), or the reduced frequency k ($k = 5.2$ here and $k = 4$ at Mackowski and Williamson (2017) and Fernandez-Feria and Sanmiguel-Rojas (2020)).We observe that any change in η with Re for the smooth case fall within the confidence intervals. Although Senturk and Smits (2019) point to an increase in η against increasing Re for a smooth pitching foil, other studies have reported a limited impact of Re on the propulsive performance of a pure-pitching foil for $Re \geq 8,000$ (Deng et al., 2016). It might very well be a limitation of experimental measurements to delineate the difference in efficiency with increasing Reynolds number since it is a notoriously difficult quantity to measure accurately.

In relation to the rough foils, the efficiency also decreases as the surface roughness increases, similar to thrust and power. Although the flow fields show negligible alterations with the change in roughness, the cycle-averaged forces point to a performance reduction as the roughness increases. The thrust decrease observed for 36% and 70% roughness coverages compared to smooth foil can be related to an increase in the profile drag. To further explore this effect, in the next section, we have compared our flapping foil results with static foil measurements carried out using the same foils within the same Re range.

4.3.2 Comparison between static and flapping regimes

In this section, we introduce the data collected for static foils and compare it with the pitching foil results to further explore why there is a change in thrust production with a change in roughness coverage. The static data was acquired within the same Re range and roughness coverages as the flapping cases, for an angle of attack (θ) range of $-4^\circ \leq \theta \leq 20^\circ$. To compare both scenarios, we have selected an angle of attack value equal to the average θ experienced by the foil during half the pitching cycle (red dashed-line in Figure 4.6A, denoted as θ_s). Next, we develop a comparison parameter or *penalty*, that evaluates the change in streamwise force generated by the smooth

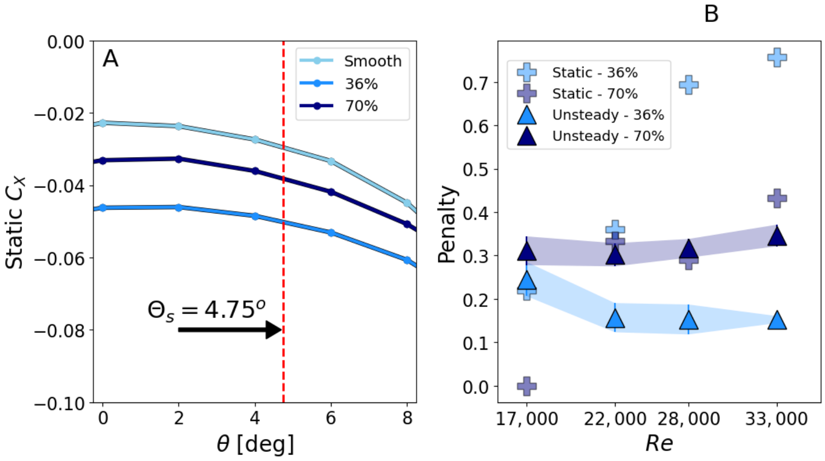

FIGURE 4.6: A) Static C_X vs angle of attack Θ measured using static foils at $Re = 28,000$. Smooth foil is presented in light blue, 36% in medium blue, and 70% in dark blue. The red dashed line indicates the θ used to compare with the unsteady regime, defined as $\theta_s = 4.75°$. B) Thrust and drag penalty due to roughness for both the flapping (triangles) and static results (crosses) for the 36% case (medium blue) and the 70% case (dark blue). The shadow region introduces the confidence intervals calculated as $CI = 4.6\sigma/\sqrt{N}$.

and rough foils. Given that static state will produce drag (for all three foils) and the unsteady scenario will generate thrust, we present the penalty in its absolute value to help with the comparison. Since we have found surface roughness to be detrimental for $\overline{C_X}$ for all cases considered, a positive penalty value in the static state indicates an increase in drag due to roughness elements, while $Penalty > 0$ in the flapping regime means a decrease in thrust caused by the roughness elements. Here, $Penalty$ is defined as the relative change in thrust for a rough foil compared to the smooth, $|(C_{X,rough} - C_{X,smooth})|/C_{X,smooth}$.

The penalty parameter is presented in Figure 4.6 for static foil (crosses) and flapping foil measurements (triangles). The addition of surface roughness increases the drag production in the static state across the Re range considered. At $Re = 33,000$, it reaches a 76% drag penalty for the 36% roughness and 43% penalty for the 70% roughness coverage, compared to the smooth foil. The drag performance of the foils at the static regime depends not only on the area covered by bumpers but also on the arrangement of the rough elements. Although the 70% presents more coverage than the 36%, the interactions between the flow and the intermittent distribution of the spanwise rows of rough elements at the 36% foil surface are responsible for the higher drag penalty. On the other hand, the flapping foils with roughness generate less thrust across the Re range compared to the smooth foil. At $Re = 33,000$, the thrust decreases by 35% and 16% for 70% and 36% roughness coverages, respectively. However, the flapping state appears to be more robust to Re changes. It reduces the penalty observed for static foils, especially for the 36% coverage. At $Re = 33,000$, foils with 36% coverage experiences a roughness penalty of 76% in the static state compared to a 16% penalty

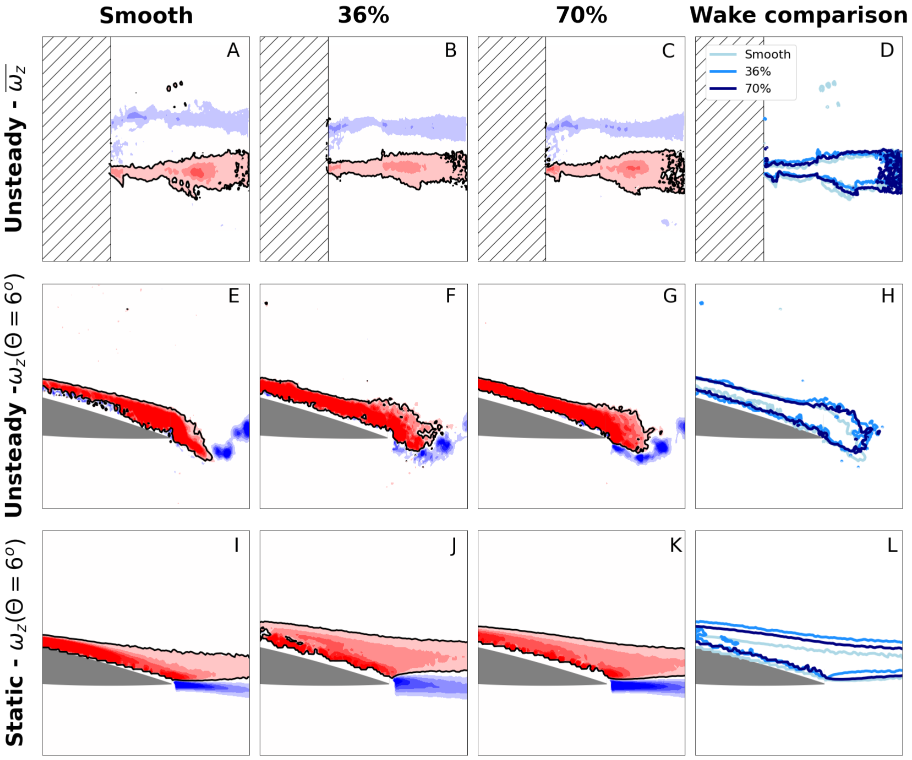

FIGURE 4.7: Pitching cycle-averaged vorticity (A,B,C), pitching instantaneous vorticity at $\theta = 6°$ degrees (E,F,G) and static PIV results at $\theta = 6°$ (I,J,K). Smooth foil (A,E,I), 36% (B,F,J), and 70% (C,G,K). The comparison of the wakes generated by the foils at each of the conditions is presented at (D,H,L). All data obtained at $Re = 28,000$.

in the flapping state. Previous work has shown that parameters such as the kinematics or the Strouhal number have a strong influence on the propulsive performance of an oscillating foil (Zurman-Nasution et al., 2021b). In line with this, we believe that the motion characteristics of this study could be minimising the impact of the roughness elements on both the wake development and force production.

To further analyse the data presented in Figure 4.6, we present the out-of-plane vorticity (ω_Z) in Figure 4.7. The first row consists of the cycle-averaged unsteady pitching ω_Z, and the positive vorticity regions are enclosed with isolines. In second and third rows, we present the flow-field data measured at $\alpha = 6°$ for a pitching foil and a static foil, respectively. The first three columns correspond to 0% (smooth), 36% and 70% roughness coverages, respectively. The fourth column introduces a comparison between different roughness cases with overlapped ω_Z isolines. The comparison of all three flapping cases suggests that the addition of surface roughness does not introduce major changes in shedding shear layers. The mild effects could be explained considering the fact that the foils are operating at Reynolds numbers where the boundary layer is transitional (from laminar to turbulent). Adding roughness essentially induces an early development of a turbulent boundary layer, and it would be transitionally rough (if at all) in all these conditions. Hence, we would expect that increasing the size of the roughness elements could have a major impact on the wake characteristics of the pitching foil. In contrast, in the static state, foils with 36% and 70% roughness have thicker shear layer in time-average compared to the smooth case, similar to the findings by Guo et al. (2021). The presence of thicker shear layers, which are caused by the additional pressure drag incurred by the roughness elements, can be responsible for the 76% drag penalty shown in Figure 4.6.

4.4 Conclusions

In this study, we have analysed the influence of surface roughness on the propulsive performance of flapping foils, using force and flow measurements. Three NACA0012 foils with different roughness coverage ratios have been constructed, and tested within the Reynolds number range of $17,000 \leq Re \leq 33,000$. We have found that the addition of surface roughness is detrimental to thrust production and efficiency of a pitching foil. The foils with 36% and 70% roughness produce 16% and 35% less thrust, respectively, compared to the smooth foil. We have determined that Re does not play an important role on neither the thrust nor efficiency for the Re range and roughness coverage ratios considered. Although we have seen no significant change in the wake flow, the foils with roughness experience a decrease in thrust and efficiency, which can be explained by an increase in profile drag associated with the roughness elements. We have compared the effects of roughness on static and flapping states, finding that the former is considerably more sensitive to it. The roughness penalty for 36% roughness coverage is reduced from 76% in the static state to 16% for flapping. The strongest decrease occurs at the highest Re, highlighting that the effect of roughness on flapping systems is very different than on static systems. This shows that the performance of flapping systems is more robust to the changes in surface roughness.

Declaration of Interests: The authors report no conflict of interest. **Acknowledgements**

This research was supported financially by the Office of Naval Research Global Award N62909-18-1-2091, the Engineering and Physical Sciences Research Council (Grant No: EP/R034370/1) and the doctoral training award.

Data availability statement

All data supporting this study will be made openly available from the University of Southampton repository upon publication.

Chapter 5

Force models for a flapping foil under unsteady upstream conditions

University of Southampton

Abstract

Faculty of Engineering and Physical Sciences
School of Engineering

Doctor of Philosophy

Flow past flapping foils:
Surface texture and unsteadiness effects

by Rodrigo Vilumbrales Garcia

Fish can significantly improve their swimming performance if their kinematics are adequately adapted to its surroundings. It is difficult to adapt kinematics in an efficient way as the manoeuvre required to reach the optimum kinematics is unknown and the first step to realise this is to accurately predict the performance that could be obtained for several candidate manoeuvres. In this work, we develop different types of force models with Koopman-based system identification tools for a foil executing transition manoeuvres in its kinematics. We show that a first order ODE in force coefficient is sufficient to capture the dynamics for a single foil in clean flow provided the phase information is used as an input. We find that such a model is erroneous (up to 25%) when used in unsteady surroundings since the signals are strongly influenced by vortices in the oncoming flow. This is overcome by enhancing the model with information about the surroundings, specifically, by providing the relative location between the foil and the large-scale vortices in the incoming flow. This improves the predictions highlighting the importance of adding relevant physical information about the surroundings in these force models. Finally, we use these different models to test different manoevures to identify the the optimum-path at different operating conditions (unseen by the model during development). The model containing wake information can predict the optimum path with a Pearson Correlation Coefficient higher than 80% for all the cases considered. We conducted an experimental implementation of the transition approach. A good agreement is seen between numerical and experimental data. This highlights the importance of carefully selecting the inputs to recover accurate governing equations for a flapping foil operating in an unsteady flow. This also provides a pathway for developing manoevuring capabilities in control applications.

5.1 Introduction

Fish can significantly improve their swimming performance if their kinematics and paths are adequately adapted to the incoming flow. Previous studies have shown that the endurance of an individual travelling inside a school can increase up to six times when compared to an animal swimming alone Weihs (1973). Due to the high unsteadiness of the schooling operation, a proper understanding of the surrounding flow is essential. To maintain the performance gains, the swimmers must adapt to any changes in the incoming flow. The importance of adapting implies that, to replicate this ability of fish to manoeuvre and extract a performance augmentation of the unsteady upstream conditions, first we need to be able to predict fluid forces in real-time. Tandem flapping foils have been widely used to replicate the characteristics of fish schooling. By carefully tuning the motion between the two objects of the arrangement, a large performance benefit can be achieved Akhtar et al. (2007); Kurt and Moored (2018). For a given longitudinal distance between foils, the phasing between the motions of the leader and follower, together with the *St* value, governs whether the hind will achieve a performance augmentation or detriment Muscutt et al. (2017a).

Although the mechanisms behind the performance augmentation of tandem flapping foils have been widely studied, when the optimum trajectory that maximises the performance inside the wake is unknown, a prediction stage has to be carried out. The forces that would be produced if the foil were to follow a certain path inside the wake need to be estimated. If accurate predictions can be made for a set of route candidates, we can later select the motion that maximises the performance. A first approximation to model the evolution of the forces generated by a flapping foil can be seen at Theodorsen and Mutchler (1935) to predict aerodynamic flutter. Garrick (1936), extended the equations derived by Theodorsen and Mutchler (1935) to approximate the propulsive forces, and Lighthill (1969) completed the work done by Garrick applying its equations to a lunate tail of a fish. The main disadvantage of the previous methods is that they all assume small amplitude kinematic motions, rectilinear vortex wake and perfect fluid, making them not suitable to predict the forces of a foil inside unsteady incoming flow. In this study, the foil is not only subjected to unsteadiness but it needs to adjust its trajectory to reach the optimum route, meaning that a manoeuvre motion needs to be executed. Flapping foils have been found to execute manoeuvring motions in an efficient way Read et al. (2003); Schouveiler et al. (2005); Kato (2000); Ahlborn et al. (1991). The manoeuvring phase of the motion, essential to achieve the performance augmentation, will induce a rapid change in the forces that will increase the unsteadiness of the problem, which needs to be taken into account by the force-prediction models. In the recent years, the use of Machine Learning (ML) for control applications has greatly improved. Weymouth and Yue (2013) found that the use of physical knowledge of the system could improve the predictions obtained by simple regression models at considerably less expense than high-resolution numerical predictions. Another recent approach is the Sparse Identification of Nonlinear Dynamical systems (SINDy) Brunton et al. (2016a), where user-interpretable governing equations can be discovered. This tool has been used for a solo pitching foil, identifying the governing equations for attached flows and separated flows Sun et al. (2021). Still, it is yet to be seen if the approach can be used for the considerably more complex system of tandem foils. By combining physical knowledge and novel system identification tools, we expect to not only accurately predict the performance of the foil, but also to gain knowledge about the problem.

In this study, we develop force models to predict the path that maximises the performance of a flapping foil swimming inside unsteady incoming flow. In Section 2, the problem definition is explained. We conduct several simulations of a foil executing transition motions in its kinematics and record the forces to be used for the construction of the models. In Section 3, we present the forces predicted for a foil in the solo scenario. Next, in Section 4, we test the models with different inputs in a tandem arrangement. In Section 5, we test the optimum-path prediction capabilities of the models at different incoming-wake conditions. The predictive performance, in terms of time-signal estimation and prediction error is studied, and the limitations of the models discussed. Finally, we present an experimental implementation of the transition approach conducted at the University of Southampton recirculating water tunnel.

5.2 Methodology

In this study we consider a set of two NACA0016 flapping foils in tandem configuration. The arrangement consists of one foil at the front, fore (f), and another at the back, hind (h). The foils are immersed in a flow with free-stream velocity U_∞, at a Reynolds number $Re = Uc/\nu = 7000$, where c is the chord, and ν is the kinematic viscosity. The foils are separated by a constant longitudinal distance equal to three times the chord. The motion of the foils is prescribed by sinusoidal heaving (h) and pitching (θ) motions acting at $x/c = 0.25$, as defined by Eq. 1

$$\begin{aligned} h_f &= Asin(2\pi ft), & \theta_f &= \theta_A cos(2\pi ft), \\ h_h &= Asin(2\pi ft + \phi), & \theta_h &= \theta_A cos(2\pi ft + \phi). \end{aligned} \tag{5.1}$$

where f is the oscillating frequency, $A = c$ is the heaving amplitude, ϕ is the phasing between the motions of the fore and hind foil, and θ_A is the pitching amplitude. The latter is selected to ensure the maximum effective angle of attack $\alpha_e = arctan(\dot{h}/U_\infty) - \theta = 10^\circ$, in line with previous studies Muscutt et al. (2017a). The Strouhal number can be defined as $St = 2Af/U = 0.36$. In this study, the hind foil executes transition

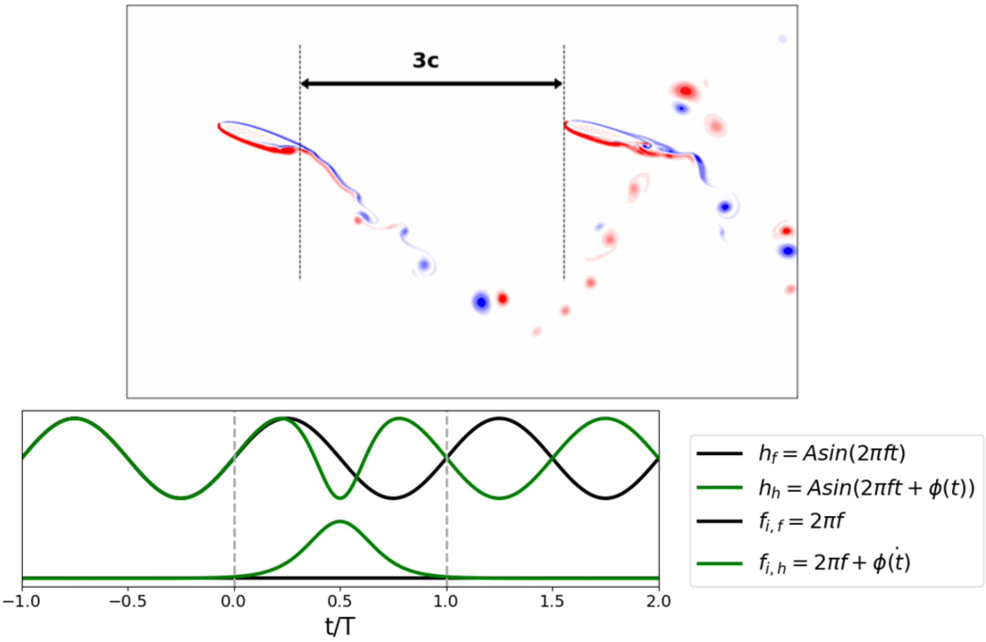

FIGURE 5.1: Sketch of the tandem arrangement considered in this study. The bottom part of the figure introduced the manoeuvre motion executed by the hind foil (green) in its kinematics during cycles 0 to 1.

manoeuvres inside the incoming wake to explore several possible routes. The transient motion consists of an instantaneous change on the ϕ component denoted at Eq. 2.1. The motion of the foil can be divided into three parts, as depicted at Figure 5.1. An initial cycle (t/T =-1 to 0), defined by a constant phasing ϕ_0. A transition period (t/T= 0 to 1), where the foil will adjust its kinematics, and a final new state (t/T= 1 to 2), defined by a constant ϕ_1. The transition motion is defined following a first order logistic function as follows (Yin et al., 2003):

$$\Delta(\phi(t)) = \frac{\xi}{1 + e^{(-k(t-t_0))}} \tag{5.2}$$

where t_0 is the midpoint of the functions, ξ is the ϕ increment, and k is the growth rate. The time (t) used to develop the models is in dimensionless form as $t* = tU/c$, ,where c is a characteristic length, or the chord in this study, but for display purposes, we present the figures as $t* = t/T$. Figure 5.1 introduces a comparison between the motions of the fore and hind foil for a case where the latter is subjected to transition motions. As shown by the evolution of h_h, there is an instantaneous adjustment of kinematics that leads to a different state of ϕ_1 between the foils. To further explain this evolution, we introduce as a parameter the instantaneous frequency $f_i = 2\pi f + \dot{\phi(t)}$. While for the fore this value is constant through the three cycles, the $f_{i,h}$ presents an acceleration/deceleration period, allowing the foil to change its state with respect to the wake during the noted transition cycle. To explore several scenarios, we develop a database of 64 cases consisting of 8 different ϕ_0 and ϕ_1, from 0π to 1.75π. The performance of the models will be assessed against 150 test cases, not seen during the training phase, at 10 different ϕ_0 and 15 ϕ_1, from 0π to 1.75π. In this study, we aim to find the route that maximises the lift performance of the hind foil, defined as $C_L = 2F_L/\rho U_\infty^2 c$, where F_L is the instantaneous lift force, as described in Figure 2.3. The precision of the predictions will be presented based on the normalised root mean square error ($NRMSE = RMSE/(y_{t,max} - y_{t,min})$.

An in-house CFD solver is used to generate the benchmark data to study this system. This solver uses the Boundary Data Immersion Method (BDIM,Weymouth and Yue (2011)) to simulate the time-evolution of the viscous Navier-Stokes using a convolution over the fluid and any immersed dynamic geometries. The convergence of this method is quadratic, and has been previously validated for flapping foil systems in several studies over a wide range of kinematics Maertens and Weymouth (2015); Polet et al. (2015). A rectangular Cartesian mesh is used with a grid spacing of $\Delta X = \Delta Y = c/192$ near the foils and in the inter-foil region with grid stretching used in the outer fluid domain Lagopoulos et al. (2019).

To develop force models capable of predicting the optimum path inside the unsteady wake of the incoming storm, we follow the approach presented by Brunton et al. (2016b). The method aims to identify sparse nonlinear dynamical systems from measured data. The system can be defined as follows:

$$\frac{d}{dt}X = f(X,U) \tag{5.3}$$

where X is the state vector and U are the control inputs. The method builds a library of candidate functions $\Theta(X,U)$ to solve $\dot{X} = \Theta(X,U)\Xi$, where Ξ is a sparse matrix of coefficients. Once the $\dot{X}$ model is recovered, it can be use to project forward in time the C_L forces, for a given set of initial conditions.

5.3 Force models for a foil immersed in uniform upstream conditions

We start by identifying the governing equations for a *solo* foil that executes transitions in its motion. To obtain a first idea of the inputs to include in the library of functions, we can analyse the equations of a sinusoidal signal with changing phase, Y:

$$Y = Asin(2\pi ft + \phi(t)) \tag{5.4}$$

$$dY = (\dot{\phi}(t) + 2\pi f)Acos(2\pi ft + \phi(t)) \tag{5.5}$$

Model	State vector	Control
Delay raw	C_L, $\dot{C}_L$ (raw)	f_i , $\dot{\phi}$, $\ddot{\phi}$,
Delay filtered	C_L, $\dot{C}_L$ (filtered)	f_i , $\dot{\phi}$, $\ddot{\phi}$
Kinematics	C_L (raw)	f_i , $\dot{\phi}$, $\ddot{\phi}$, h, $\dot{h}$ θ, $\dot{\theta}$

TABLE 5.1: Parameters used to recover the force models.

$$ddY = \phi\ddot{(t)}cos(2\pi f t + \phi(t)) - (\phi\dot{(t)} + 2\pi f)^2 Asin(2\pi f t + \phi(t)) \tag{5.6}$$

Based on the terms of previous equations, we define the state vector as $X = [C_L, \dot{C}_L]$, and the control inputs as a combination between ϕ terms and the instantaneous frequency f_i. Since the SINDy approach has been found to be sensitive to noise in the data Fasel et al. (2022), we compare the effects of identifying the system with both raw and filtered C_L. As defined by Eq. 5.3, the system identification will aim to recover $\dot{X} = [\dot{C}_L, \ddot{C}_L]$. The presence of higher-order terms is expected to maximise the impact of the noise in the data. Finally, we develop another model that contains as control inputs the kinematics of the foil (h, θ). The impact of those parameters on the forces evolution of a flapping foil has been well documented in the past Theodorsen and Mutchler (1935). Table 5.1 introduces the details of the three models considered.

Figure 5.2 introduces the projections at three selected cases achieved by the Delay model (filtered -blue- and raw -pink -), and the kinematics model (-red-) (Table 5.1). We present three cases with increasing transition strength ($\Delta(\phi)$= [0π, 0.5π, and π]). As insets in the figure, we provide the main coefficients and terms found by each of the models. The system identification is recovering, for the case of the delay models (raw and filtered), the main components presented at Eq 5.4-5.6. Still, the effects of the noise are clear. The model that contains the raw input data is not able to accurately lock the frequency of the signal, with the discrepancies being maximised as the strength of the transition increases. On the other hand, and after filtering the data, the accuracy improves for all the test cases by 33%. The filtering is imposing a slight delay in the predictions, increasing as $\Delta(\phi)$ is maximised. Nevertheless, we observe that, by carefully selecting the inputs used in the system identification process, the robustness of the model to noise and the predictions accuracy is greatly increased. The kinematics model overperforms the delay filtered at every case, and, although is not able to capture the entire peak in the forces generated during the strongest manoeuvre, achieves an overall error of 9% across all the validation cases.

To better understand the system identified by the kinematics mode, we present at Figure 5.3 the contribution of each of the parameters recovered by the approach on the reconstruction of the $\dot{C}_L$ signal. The figure introduces at the first row the contribution of the main component, $\dot{h}^3$, and compares it with the target (light gray). We observe that the contribution of this term is equally important in the two phases of the forces evolution, the transition and the new state. The second row includes the contribution

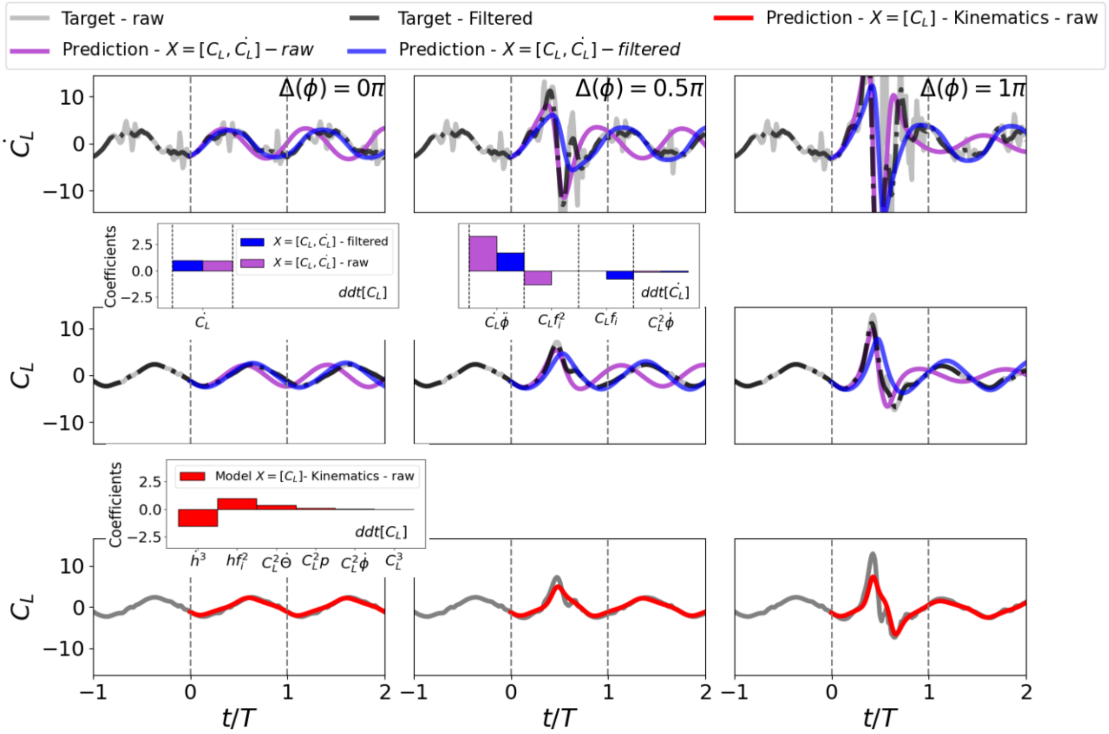

FIGURE 5.2: Comparison between the projections for three selected test cases and the target data. Delay - raw model (pink), delay - filtered (blue) and kinematics model (red). The insets contain the components recovered for each of the models during the system identification process.

of the i_f term. The new component is slightly modelling the second peak of the transition, and combines with $\dot{h}$ to recover the lift produced at the new state. The overall contribution during the transition is minor when compared to the first term, as can be seen by comparing the light-yellow and orange contours of Figure 5.3, second row.

The third row adds the contribution of the $\dot{\theta}C_L$ term. Its impact is major on capturing the second transition peak, but it loses importance as we progress towards the new state phase. The contribution of the rest of terms, for this test case is negligible. This highlights the importance of carefully selecting the inputs to recover the dynamics of a highly unsteady system.

5.4 Force models for a flapping foil immersed in unsteady upstream conditions.

The performance of a foil submerged in an unsteady incoming wake has been studied in the past. The interactions between its motion and the incoming vortices can lead to important performance benefits, or to large detriments Kurt and Moored (2018); Muscutt et al. (2017a); Boschitsch et al. (2014). The reasons behind the performance detriment/augmentation can be associated to the foil/wake interactions. As seen by

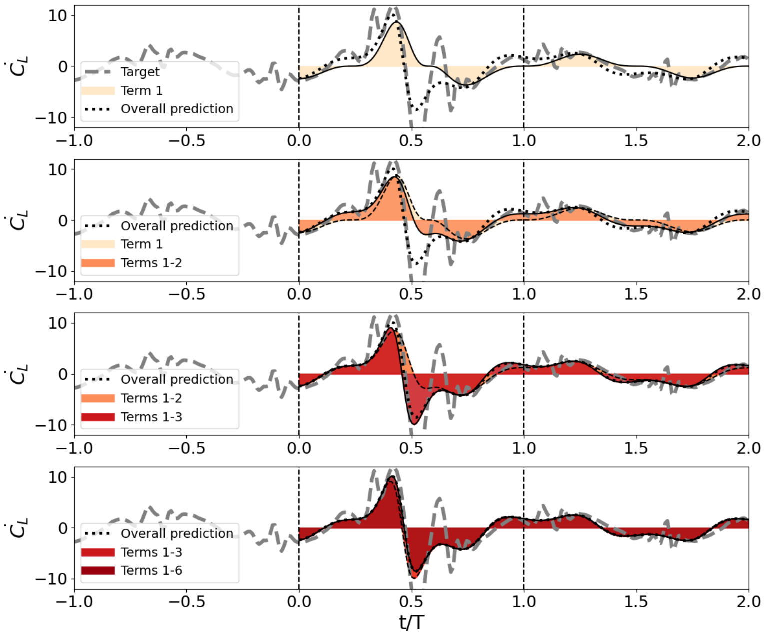

FIGURE 5.3: Analysis of the components recovered by the kinematics model for the solo foil scenario. Each row introduces the sum of the contributions of each of the elements presented at the inset of Figure 5.2.

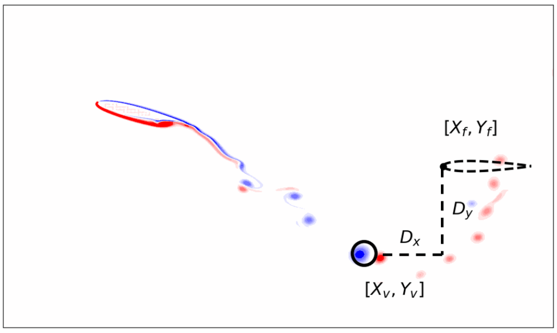

FIGURE 5.4: Schematics of the virtual simulations used to track the evolution of the wake. The information is included as a control input in the wake info model.

Muscutt et al. (2017a), when the foil encounters the main incoming vorticity structures, a performance detriment is achieved. On the other hand, if the hind body is able to swim in-between the Karman Street, a performance augmentation can be obtained.

Considering the importance of the interactions between the foil and the incoming vortices, we develop a new model that includes in the library of controls the relative distance between the foil and the main vorticity structures of the flow, as depicted in figure 5.4. To reduce the computational expense of the study, we perform a simulation with a virtual foil submerged in the unsteady incoming wake at $St = 0.36$. We then use it to track the evolution of the vortices and compute the relative distance with the foil as follows:

$$d_x(t) = X_F(t) - X_V(t) \tag{5.7}$$

$$d_y(t) = Y_F(t) - Y_V(t) \tag{5.8}$$

5.4.1 Force prediction capabilities

Figure 5.5 shows a comparison between the projections achieved by the models for the solo foil and tandem scenarios at three comparable test cases. The first column presents the solo foil C_L evolution at two different transition cases. The second and third column introduce the predictions achieved by the kinematics and wake info models. The first test case, presented in the top row, corresponds to a situation with mild foil-wake interactions. In this case, the kinematics model is not able to achieve the same level of accuracy as for the solo foil, the reason being the higher unsteadiness of the problem. Although the improvement of adding wake information can be seen in this case, the accuracy augmentation is more evident in the second test case. In this scenario, the strong interactions between the foil and the vortices are dominating the forces evolution, and the kinematics model is not able to adapt to it. On the other hand, the wake info can detect and accommodate for the lower amplitude in the C_L evolution.

This increase in the accuracy achieved by the wake info model is highlighted when comparing the performance for all the test cases. We present the overall error ranked accordingly to the C_L amplitude at the ϕ_1 state. For comparison, we include the values obtained for the solo foil case. The lift amplitude reduces as the interactions with the incoming vortices become stronger, leading to an important raise in the accuracy obtained by the wake info model. A similar behaviour is observed as the hind foil C_L production is maximised. Hence, adding relevant wake information is helping with the predictions. The overall error, calculated as the averaged NRMSE for all test cases, is reduced from 24% for the kinematics model to 18% for the wake info across the validation cases.

To better understand the influence of the wake components recovered by the system identification tool, we present at Figure 5.6 an analysis of the wake info model. First, we observe that the transition phase is still dominated by the kinematics terms. This finding can be explained considering that the raise in the C_L production is coming from the accelerations experienced by the foil. On the other hand, the kinematics components by itself can not account for the rapid changes in C_L once the foil encounters the vortices at ϕ_1. Adding the wake components does not have a major impact on the transition, but corrects the C_L production at ϕ_1. This points to the importance of adding relevant inputs when recovering the dynamics of a highly unsteady system, that contains states with such different dynamics as here.

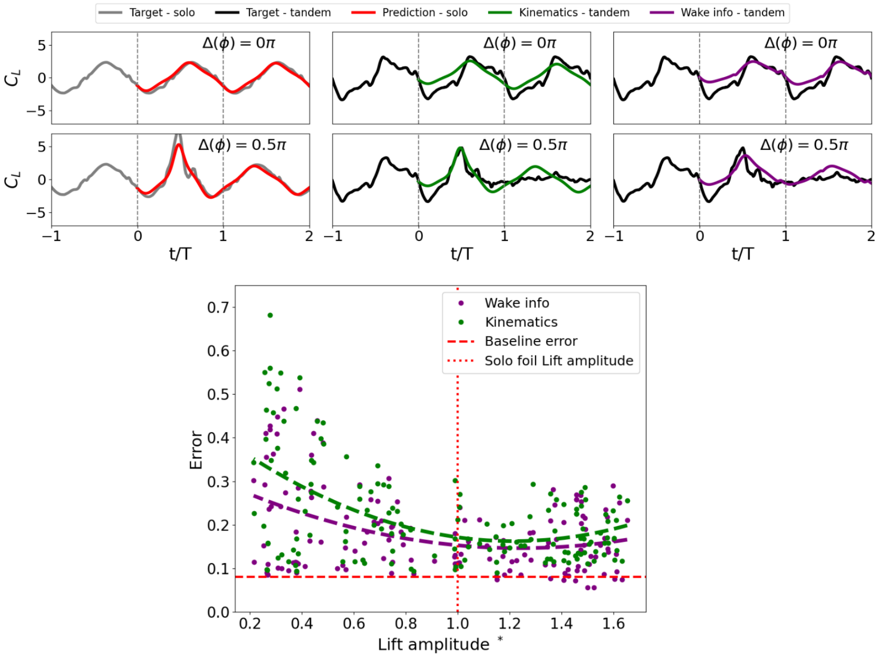

FIGURE 5.5: Comparison between target data and projections for the solo and tandem scenarios. Kinematics solo model (red), kinematics tandem model (green), and wake info (purple). The bottom figure introduces a comparison of the error achieved for all the test cases between the wake info and kinematics model.

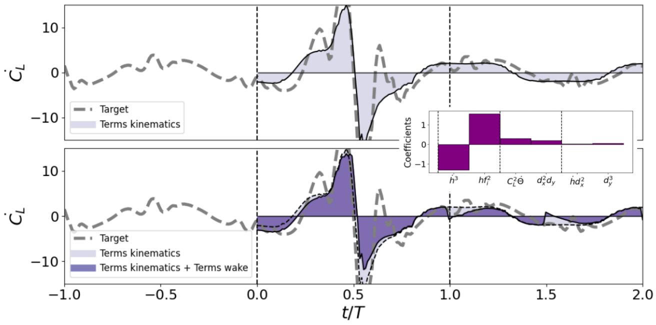

FIGURE 5.6: Analysis of the components recovered by the wake info model for the tandem foil scenario. The first row presents the contribution of the kinematic terms, while the second adds to the previous the wake terms, as seen on the inset.

Figure 5.7 introduces three instantaneous vorticity fields for the test cases introduced at Figure 5.6. We appreciate three distinctive flow characteristics based on the attitude between the foil and the incoming wake. At the first instant, corresponding to a high-lift producing case, we observe the vortex being detached at the peak of the foil motion. Next, as the foil moves past the transition cycle, the foil shows a large vorticity region near the leading edge caused by the sudden acceleration needed to reach ϕ_1. Another effect of the mentioned change in motion can be observed by the quasi vertical wake produced by the foil. Finally, at the last instant, the foil has reached the new delay. In this cases, it corresponds to a detriment attitude with respect to the wake. We can observe a large vortex being detached from the bottom surface of the foil caused by the interactions with the wake vorticity.

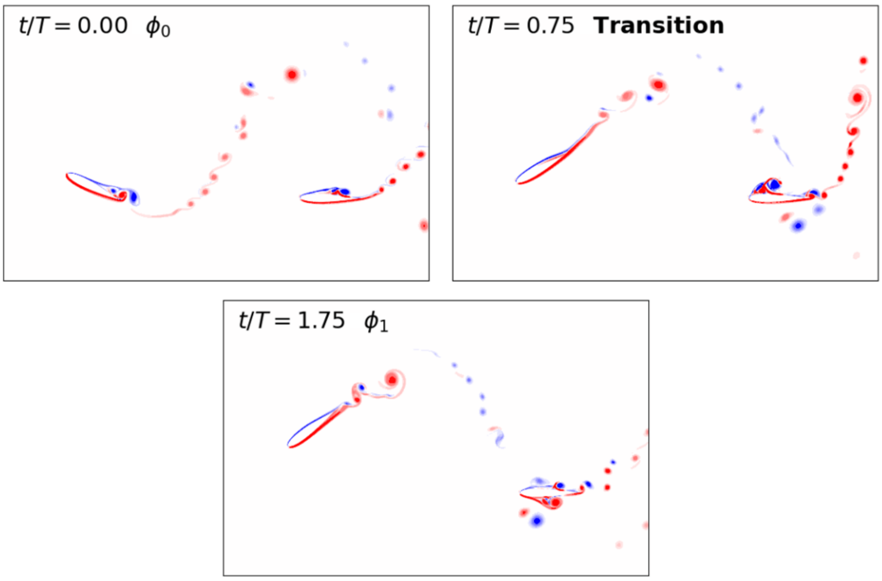

FIGURE 5.7: Instantaneous vorticity at three different time stamps for the test case presented at Figure 5.6.

5.4.2 Optimum path finding capabilities

The performance of a flapping foil immersed inside unsteady incoming flow is highly dependant on its interaction with the upstream wake. By correcting its trajectory and locating itself in the optimum path, the foil can achieve a surplus in its propulsive performance. After assessing the accuracy in the projections achieved by the models for $St = 0.36$, we test the capabilities of selecting the optimum path among several candidates at different wake conditions. To do so, we predict the C_L performance using the models trained at $St = 0.36$ for 10 ϕ_0 and 15 ϕ_1 at $St = 0.30, 0.36, 0.40$. We rank the predictions based on the lift amplitude achieved at ϕ_1, and compare the performance of the models against the target data using the Pearsons Correlation Coefficient (PCC).

Figure 5.8 introduces the rankings for the two models at each of the St values.

The incapability of the kinematics-only model to recover the dynamics of the cases with strong foil-wake interactions is maximised when assessing the ranking of the paths. The model can not identify the optimum ϕ_1 region, and its predictions are biased by the transition phase. The extrapolation capabilities are also limited, as it is producing a similar prediction for the three St considered. Adding wake information greatly increases the accuracy of the projections, achieving a PCC higher than 80% for all three St. By understanding the profile of the incoming wake, the model can identify the range of paths that maximise the lift production of the foil for all the initial conditions. As the St changes, the model is being able to notice the new optimum path location. What these results suggest is that the wake info model recovered for a foil flapping inside unsteady incoming wake is reliable to discover the path inside the vortices that maximises its performance. Also, the selection of physically-relevant parameters in the

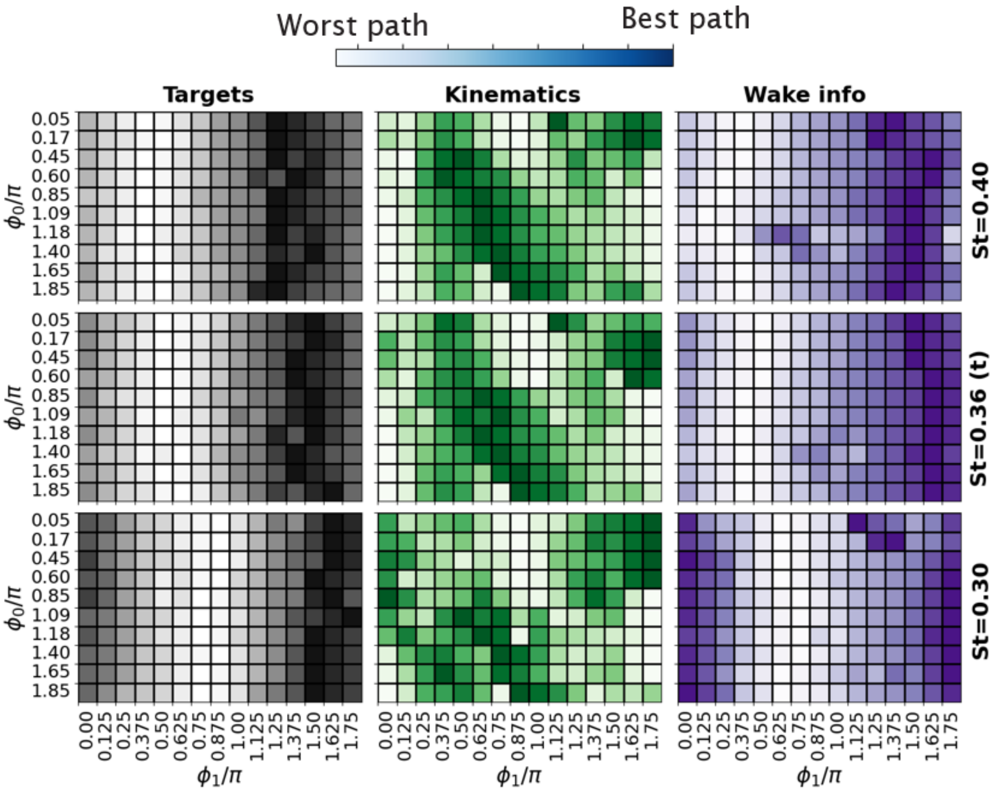

FIGURE 5.8: Study of the optimum path selection capabilities of the models. Target data (black), wake info (purple) and kinematics (green), at three different St values: 0.36 (training), 0.30 and 0.40. Light squares indicate routes with large performance detriment. Darker squares indicate optimum path inside the wake

system identification process is maximising the extrapolation capabilities, as the model is able to perform accurate ranking results for St cases not seen during the training phase.

To further assess the optimum path finding capabilities of the models, and the independence of the initial conditions, we prescribe 35 new initial conditions (ϕ_0), and perform projections for 50 different ϕ_1. We then select the path that maximises the lift production and perform a CFD simulation. Figure 5.9 presents the results obtained for the wake info model (top row) and the kinematics model (bottom row). As expected, the latter is not able to find a consistent optimum path for any of the St. On the other hand, the wake info model converges, at $St = 0.36$ and 0.40, to the route that maximises the lift production. This effect can be seen by observing the coloured lines surrounding the forces evolution. Although at ϕ_0 the variance is large, after the transition, all the paths converge to a high-performance forces scenario. The same model is not able to predict with equal level of accuracy the lowest St, which could be due to the differences between the training and testing conditions.

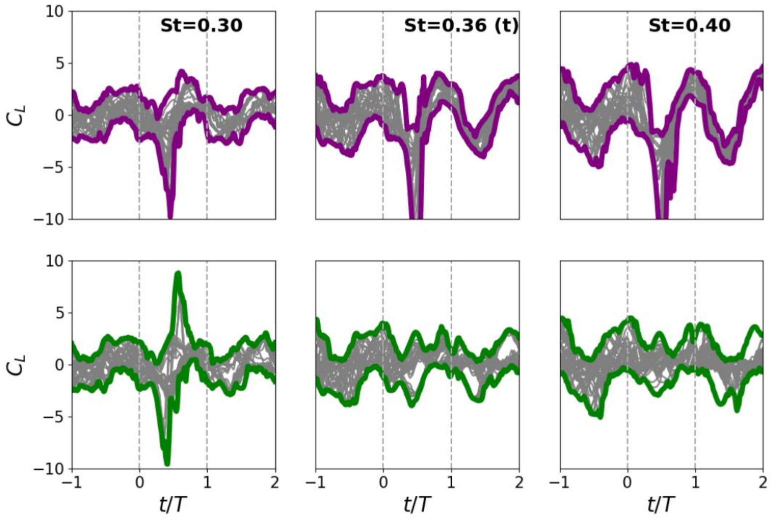

FIGURE 5.9: Application of the optimum paths prediction capabilities. Each of the lines starts at a different ϕ_0 and corresponds to a simulation based on the optimum path found by the models. The top row introduces the wake info, and the bottom the kinematics. The coloured lines surrounding the forces data highlight the convergence capabilities of the wake info, specially for $St = 0.36$ and $St = 0.40$

5.5 Experimental implementation

After assessing the performance of the models trained with the computational database, we aim to validate the results experimentally. To do so, force and flow measurements are conducted in a recirculating water flume at the University of Southampton, with a test section of 8.1 m length, 1.2m width and 0.9m depth. Two foils with a rectangular planform and a NACA0016 cross-section were 3D-printed, with a chord-length of $c = 0.10m$ and an aspect ratio of $AR = 4$. The arrangement consists of one foil at the front, fore (f), and another at the back, hind (h). The foils are immersed in a flow with free-stream velocity U_∞, at a Reynolds number $Re = Uc/\nu = 10,000$, where c is the chord, and ν is the kinematic viscosity. The foils are separated by a constant longitudinal distance equal to three times the chord. A surface plate is installed at the foil tip and the foil is placed right above the bottom wall to prevent tip vortex formation and enforce nominally two-dimensional flow. Each foil was actuated with two stepper motor (Applied Motions STM24S 3RG), one for the pitch and another for the heaving motion. The motion is prescribed by sinusoidal heaving (h) and pitching (θ) motions acting at $x/c = 0.25$, similar to CFD simulations. The Strouhal is as $St = 2Af/U = 0.36$. The forces and moments acting on the hind foil were measured with a six-axis force sensor (ATI Gamma IP65). The pitching attitude was tracked using a rotary, incremental encoder (US Digital E5) attached on the motor shaft. The heaving kinematics of the fore and hind foils was recorded using a SoftPot membrane potentiometer, as depicted in (Figure 5.10). The hind foil executes a transient motion consisting of an instantaneous change on the ϕ component denoted at Eq. 5.2, similar to the simulations conducted at this Chapter. The matrix of cases followed for this study is detailed at

Foil	Re	St	ϕ_0	ϕ_1
NACA0016	$10,000$	0.36	0π	8 steps from 0 to 1.75π

TABLE 5.2: Experimental parameters used in the current study

Table 5.2. Each trial was conducted for a total of 41 flapping cycles (where $t/T = 1$ cycle) and repeated five times. 20 cycles correspond to ϕ_0, one for the transition, and the rest for ϕ_1. The measured forces were filtered using a Butterworth filter with a low-pass frequency of ten times the flapping frequency. The power P was calculated as $P = F_Y(t)\dot{h}(t) + M_Z(t)\dot{\theta}(t)$, where $\dot{h}$ and $\dot{\theta}$ are the heaving and angular velocity, which were derived from the measured linear and angular displacement. The instantaneous and time-averaged performance metrics are the average values measured over five trials ($N = 5$). All the parameters are presented together with confidence intervals calculated as $CI = 2.58\sigma/\sqrt{N}$. To distinguish instantaneous forces from time-averaged results, the latter is denoted by $\overline{(.)}$. In this section, we compare the computational and experimental normal and thrust force (C_Y and C_X), as defined by Equation 2.5. The reported normal force C_Y, streamwise force (thrust) (C_X) and power (C_P) coefficients are defined as,

$$C_Y = \frac{F_Y}{\frac{1}{2}\rho U^2 Sc}, \qquad C_X = \frac{F_X}{\frac{1}{2}\rho U^2 Sc}, \qquad C_P = \frac{P}{\frac{1}{2}\rho U^3 Sc} \tag{5.9}$$

where ρ is the density of water, S is the span of the foil, and U represents the free-stream flow velocity.

5.5.1 Results

In this section we introduce the main results obtained during the experimental implementation of the manoeuvring methodology. First, we replicate the ϕ_1 sweep conducted at previous sections, and analyse the optimum route found for the flapping foil. The experimental forces are compared against the numerical data. Next, we evaluate different ways of transitioning, in an effort to reduce the power cost associated with the manoeuvre.

For a given St and longitudinal distance, the performance of a flapping foil immersed in an unsteady incoming wake is governed by the phasing between its kinematics and the incoming vorticity structures. In the previous section we have observed an important difference in terms of propulsive performance based on the mentioned ϕ parameter. To analyse experimentally the findings of the previous section, we present in Figure 5.11 the projected forces (thrust and normal force) C_Y (as defined in the amplitude at the ϕ_1 state. In line with previous findings (Muscutt et al., 2017b), a sinusoidal evolution

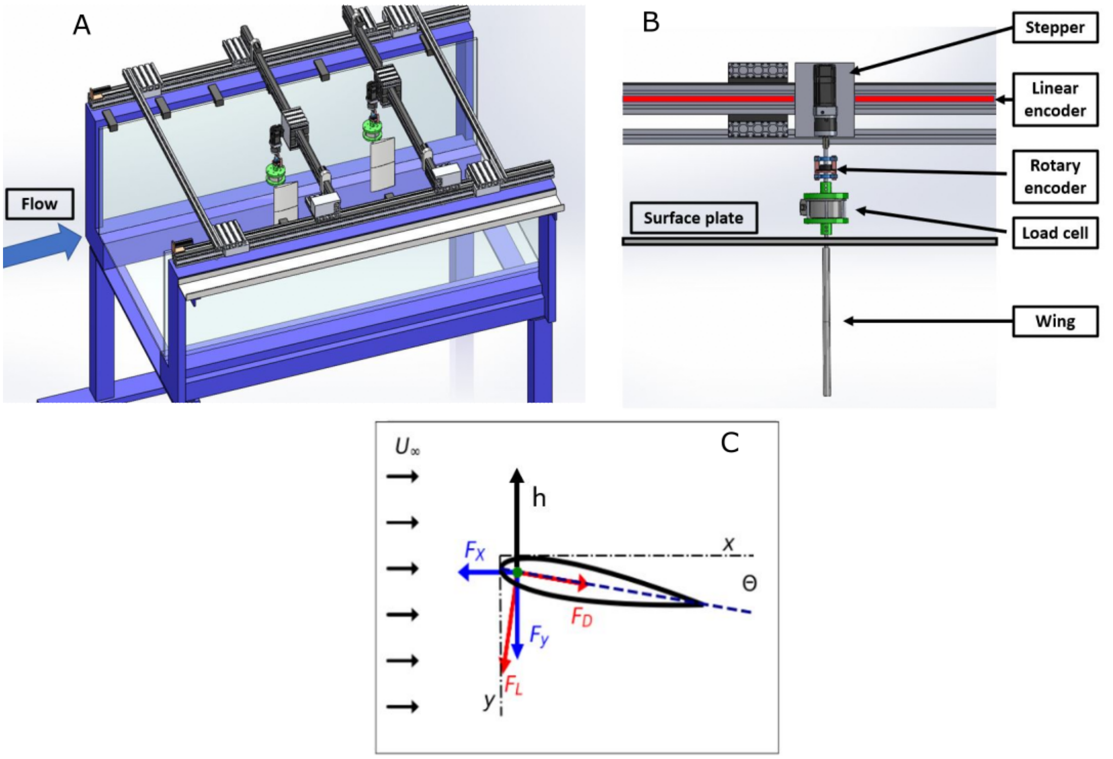

FIGURE 5.10: Schematics of the tandem flapping foil experiments. A) depicts the details of the water tunnel setup. B) Introduces the flapping arm components. C) Presents the schematics of the forces

is observed, with two distinct ares in terms of forces production. When the foil trajectory is delayed in the range of 0.25π to 0.75π, the C_Y amplitude drops, corresponding to a low-performance area. On the other hand, we find in the experimental analysis an optimum range to maximise the forces production located in-between 1.25π and 1.75π. This result is in line with the analysis presented at Chapter 4, and highlights the importance of adapting the trajectory to the surrounding flow in order to extract a performance augmentation from the flow.

Figure 5.12 presents the experimental C_X, C_Y and C_P (green) for three selected ϕ_1: 0π (first column), 0.5π (second column) and 1.25π (third column). We compare the forces obtained experimentally with the simulations carried out in this chapter. First, a good agreement is observed for all three forces and test cases between the numerical and the experimental results. The experimental data follows the trend captured by the computational simulations for all C_X, C_Y, and C_P. Both approaches agree well even for the cases where the thrust production, or C_X, is at its minima (second column), caused by strong foil-wake interactions. Second, the reasons behind the low-performance trajectory can be appreciated by comparing the second and third column of the figure. The transition from $0to0.5\pi$ leads to a state of low forces production, associated to strong interactions between the foil and the incoming vortices. On the other hand, when the transition reaches 1.25π, the foil can augment the performance achieved during the

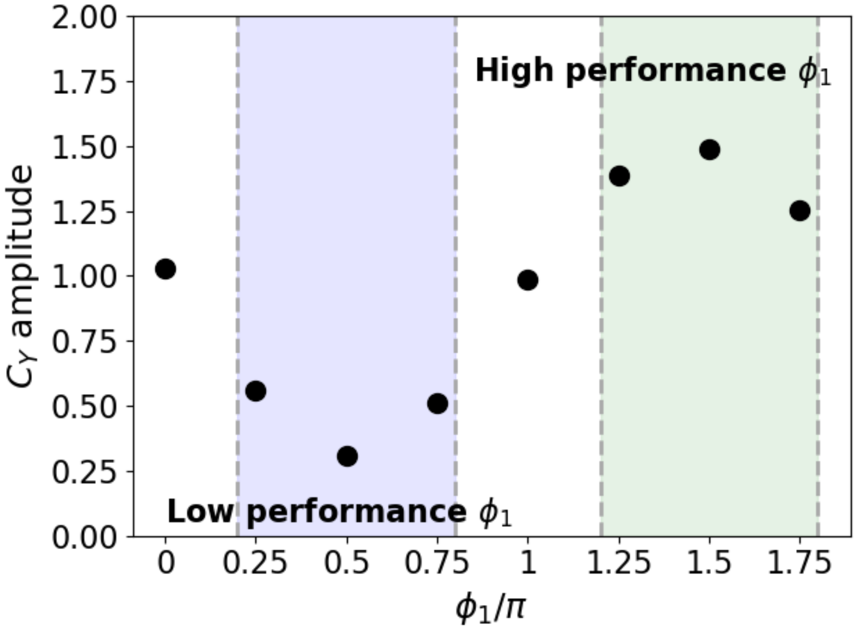

FIGURE 5.11: Lift amplitude obtained at the ϕ_1 state. The blue region correspond to low-performance kinematics. The green region highlights high-performance situations.

pre-transition phase. These results validate the computational approach, and further highlight the importance of adapting to the incoming flow to reach the optimum path inside the wake.

Although the performance of a flapping foil swimming inside unsteady incoming flow can be improved by tuning its motion with respect to the incoming wake, the manoeuvring trajectory needed to reach the optimum path can come associated with a large power cost. To analyse this effect, we present at Figure 5.14 a test case where the foil executes the transition motion during different periods of time. While the increase in the forces production is clear when reaching ϕ_1, it comes associated with a large power penalty. In all the examples carried out at Chapter 4, and Figure 5.12, the maximum time to transition was limited to one flapping cycle. This manoeuvre required a fast acceleration to reach the new state, which increased the $\dot{h}$ and $\dot{\theta}$ components, leading to a raise in the power component, as displayed in Figure 5.14. Although this power cost is unavoidable, we aim to analyse if the transition motion can be executed in a more efficient way. As a first way of testing this idea, we increase the total transition time (t_T) to 1.5 and 2 cycles. Due to the incapability of performing the one cycle transition experimentally, we compare the data with the numerical findings of an equivalent case. The first effect can be seen at the C_Y forces evolution. The peak generated during the transition cycle is greatly reduced, which comes associated to a lower maximum C_P. If the transition time is advanced to 2 cycles, the overall power evolution is reduced to one main peak.

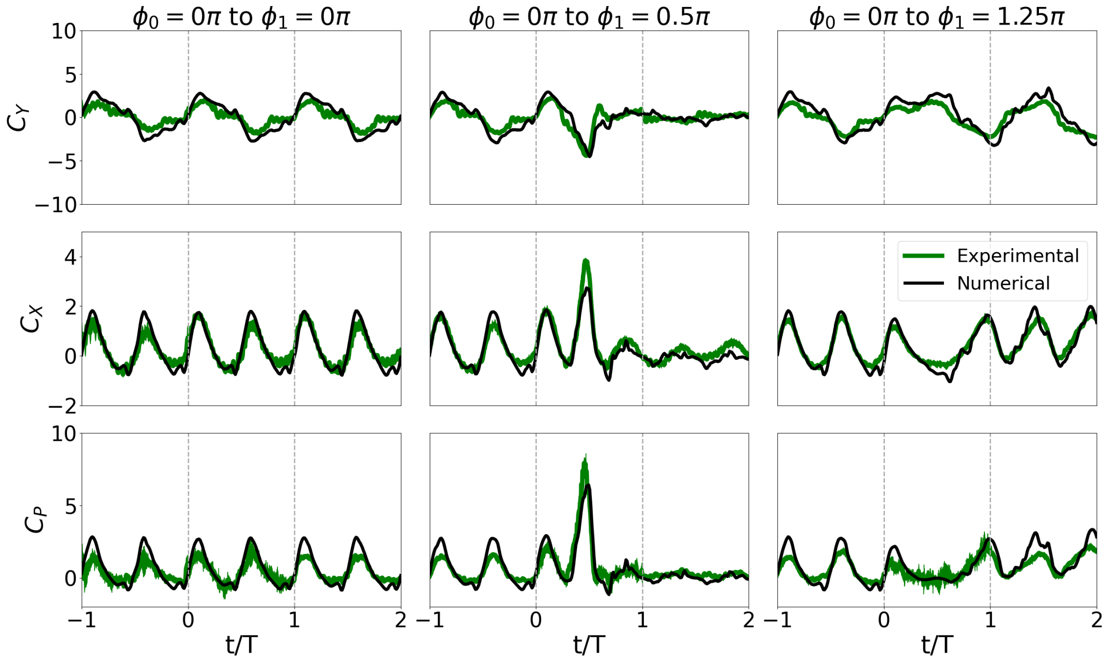

FIGURE 5.12: Instantaneous C_X, C_Y and C_P obtained during the experiments (green) and simulations (black) for three selected transition cases.

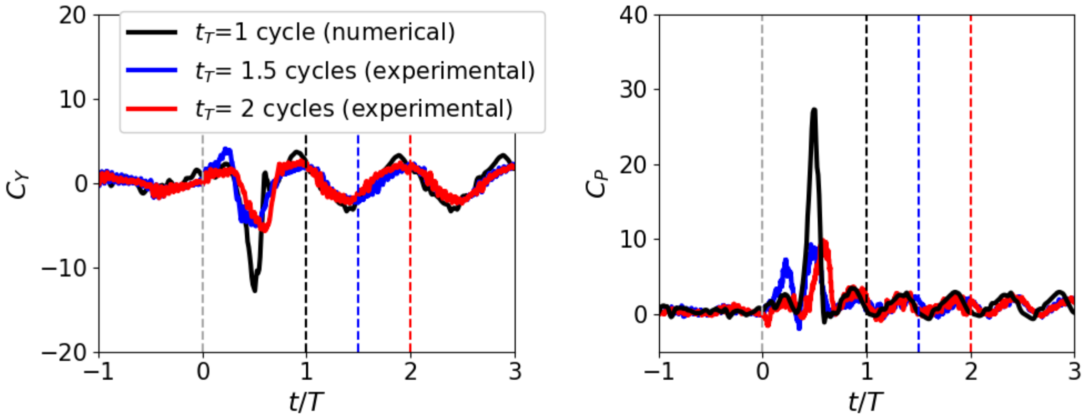

FIGURE 5.13: Instantaneous C_Y and C_P for three selected transition lengths. One cycle (black, numerical), 1.5 cycles (red, experimental) and 2 cycles (blue, experimental).

To evaluate the power cost associated to the transition phase, we can define a cost parameter as $\int_0^{t_T} C_P \, dt$. By increasing the transition time to two cycles, the overall cost is reduced by 18%. A similar decrease is observed for the one and a half cycle manoeuvre. This finding suggests that a foil can execute a transition to maximise its performance, but at a lower power cost. In the next chapter we will explore this idea in detail.

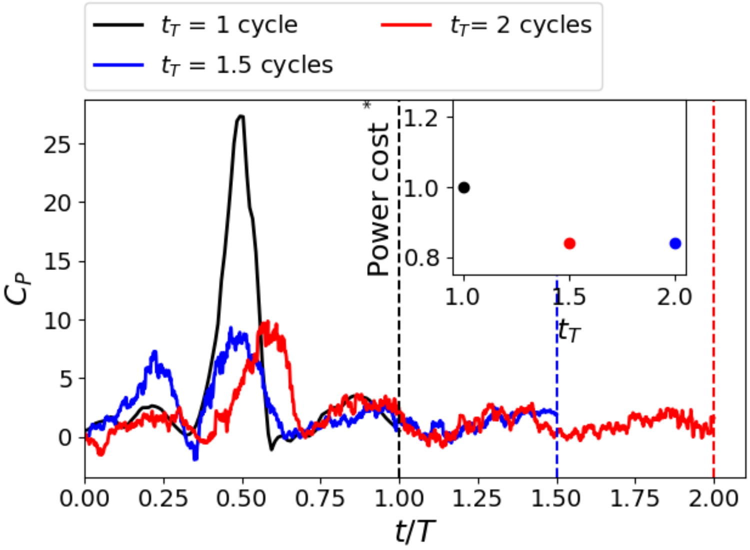

FIGURE 5.14: Analysis of the power cost used during the transitions. One cycle (black, numerical), 1.5 cycles (red, experimental) and 2 cycles (blue, experimental).

5.6 Conclusions

In this study, we have developed several force models to predict the optimum path for a flapping foil swimming inside unsteady incoming flow. CFD Simulations of two NACA0016 foils in tandem arrangement have been carried out, where the hind foil executes transition manoeuvres in its motion. First, we have analysed the influence of the control inputs used to recover the models for a solo foil scenario, finding that by adding the foil kinematics, the models are more accurate and more robust to noise. Next, we have recovered and tested the model for a tandem arrangement. The lack of understanding about the unsteadiness in the incoming flow makes the kinematics-only model unreliable. After including the relative distance between the foil and the incoming vortices, the error has been reduced by 25%. Finally, we have tested the optimum route finding capabilities of the models by ranking a set of route candidates, based on lift production. The model containing wake information has been able to achieve a correlation coefficient higher than 80%, for St values not seen during the training phase, highlighting the extrapolation capabilities of the model. Also, we have implemented experimentally the transition approach, finding a good agreement with the computational findings. This study highlights the importance of carefully selecting the inputs to recover accurate governing equations for a flapping foil submerged inside unsteady flow. Also, the optimal route-finding capabilities open the path for a real-time control implementation that would maximise the performance of a flapping foil under unsteady circumstances, and at various flow conditions or flapping regimes.

Chapter 6

Trajectory optimisation for flapping foils under unsteady inflow conditions

6.1 Abstract

Flapping foils submerged inside an upstream incoming flow can greatly improve their swimming performance if their kinematics are tuned to the incoming wake. Still, when the foil is not initially located at the best route, a transition manoeuvring needs to be executed to reach the correct kinematics. Although the benefits are clear once the foil has reached the optimum kinematics, the manoeuvring motion can come associated to large power costs. In this Chapter, we use a differential evolution approach to optimise the transition manoeuvre. We define the phase evolution ($\phi(t)$) as a combination of Hermit splines, and allow the optimiser to modify its characteristics. When the total transition time is limited to one cycle, the optimiser finds a quasi-linear trajectory, able to reduce the overall power cost by 12% when compared to a simple logistic function manoeuvre. After allowing the transition to take place in up to three cycles, we observe that the optimiser is adapting the accelerations of the manoeuvre to arrive to an overall benefit of 18%. The characteristics of the new optimised transition are analysed, and details are given about the physical reasons behind its different stages.

6.2 Introduction

The benefits of fish-schooling on the propulsive performance of its individuals have been widely documented in the past Weihs (1973). Still, the schooling configuration is found to be a highly-unsteady, constantly changing environment. Assuming that the benefits on the fish swimming performance are coming from adequate interactions with its surroundings Verma et al. (2018) implies that, if the conditions change, a manoeuvring motion is needed to adapt to the new circumstances. Tandem flapping foils have been used as a simple way of replicating the fish-schooling arrangements. Important propulsive benefits have been found, but only if the motion of the hind foil is properly tuned with the incoming wake Muscutt et al. (2017a), pointing again to the necessity of adapting to real-time changing conditions. At Chapter 5, we developed a novel manoeuvring approach that was able to locate a flapping foil in the optimum route for performance gains. Still, the transition phase was associated with large power costs, that could reduce, or even neglect, the potential benefits of reaching an optimum route. In this section we focus on optimising the transition manoeuvre needed to locate a flapping foil at the route that maximises its propulsive performance.

Several studies have been conducted to optimise the kinematics of a flapping foil: Liu et al. (2019b) used a multi-fidelity evolutionary algorithm to optimise a flapping-based power generator. Gehrke et al. (2018) develop a genetic algorithm approach to improve the efficiency and lift production of wing rotations in hover. Other researches have utilised Deep Reinforcement Learning techniques to optimise the tandem arrangement Verma et al. (2018); Zhu et al. (2022a). Soueid et al. (2009) proposed a combination of CFD and a quasi-Newton approach to optimise the motion of a flapping NACA0012.

Still, some of this techniques require large amounts of data to perform the optimisation, involving that the use of CFD simulations will induce large computational costs. To overcome this limitation, we propose the use of a simplified force model able to estimate and predict the power produced by the foil for a set of kinematics. With this approach, we aim to reduce drastically the overall expense of the process.

In this study, we aim to optimise the manoeuvring motion needed to maximise the performance of a flapping foil. The problem definition and methodology followed is explained in Section 2. In Section 3, we present the results regarding the optimised trajectories, and analyse them based on forces evolution and flow characteristics. The accuracy of the optimiser is validated against CFD, and the overall performance gains and limitations are discussed.

6.3 Methodology

In this study we consider a set of two NACA0016 flapping foils in tandem configuration. The arrangement consists of one foil at the front, fore (f), and another at the back, hind (h). The foils are immersed in a flow with free-stream velocity U_∞, at a Reynolds number $Re = Uc/\nu = 7000$, where c is the chord, and ν is the kinematic viscosity. The foils are separated by a constant longitudinal distance equal to three times the chord.

The motion of the foils is prescribed by sinusoidal heaving (h) and pitching (θ) motions acting at $x/c = 0.25$, as defined by the following equations:

$$\begin{aligned} h_f &= Asin(2\pi ft), & \theta_f &= \theta_A cos(2\pi ft), \\ h_h &= Asin(2\pi ft + \phi), & \theta_h &= \theta_A cos(2\pi ft + \phi). \end{aligned} \tag{6.1}$$

where f is the oscillating frequency, $A = c$ is the heaving amplitude, ϕ is the phasing between the motions of the fore and hind foil, and θ_A is the pitching amplitude. The latter is selected to ensure the maximum effective angle of attack $\alpha_e = arctan(\dot{h}/U_\infty) - \theta = 10°$, in line with previous studies Muscutt et al. (2017a). The Strouhal number is set as $St = 2Af/U = 0.36$. The approach followed in this study consists of a foil executing transition manoeuvres inside the wake generated by another foil. The transient motion will imply an instantaneous change on the ϕ component, for a given initial ϕ_0 and final ϕ_1 delays. In Chapter 5, the transition motion was prescribed by a logistic sigmoid evolution, controlled by an acceleration rate and a intermediate point. Although that manoeuvring motion was successful in locating the foil in the optimum propulsion path, it came associated with large power consumption. Here, we change the approach in the transition motion by defining the evolution of ϕ as a combination of Hermite splines:

$$\phi(t) = h_{00}(t)\phi_k + h_{10}(t)(x_{k+1} - x_k)m_k + h_{01}(t)\phi_{k+1} + h_{11}(t)(x_{k+1} - x_k)m_{k+1} \tag{6.2}$$

where:

$$\begin{aligned} h_{00}(t) &= 2t^3 - 3t^2 + 1, & h_{10}(t) &= t^3 - 2t^2 + t, \\ h_{01}(t) &= -2t^3 + 3t^2, & h_{11}(t) &= t^3 - t^2. \end{aligned} \tag{6.3}$$

The overall transition phase comprehends the motions executed by the foil in the time lapse between $t = 0$ and $t = t_T$, where $t = t_T$ corresponds to the instant when the foil has reached ϕ_1. A schematic of the motion is presented at Figure 6.1. The overall signal is divided into four parts, controlled by five nodes of given time (x) and ϕ values. The joints between the Hermite splines are controlled by the m values, and defined as: $m_k = (1 - c)\frac{\phi_{k+1} - \phi_{k-1}}{x_{k+1} - x_{k-1}}$, where c is a tension parameter. In this section we decided to explore a transition case associated to a low-performance ϕ_0, a strong $\Delta(\phi)$, and a high-performance ϕ_1. To allow the comparison with the results presented at Chapter 5, we fix the ϕ values of the first and last control nodes to $\phi_0 = 0.5\pi$ and $\phi_1 = 1.5\pi$.

For this study we have selected a Differential Evolution (DE) algorithm, implemented in the Python package "Pymoo" Blank and Deb (2020). DE are powerful tools in the category of evolutionary optimisers Price (2013). A set of candidates is evaluated based

Node	ϕ	x	c
Node 1	0.5π	0	1
Node 2	$[0, 2\pi]$	$[0, t_{max}]$	$[0, 1.00]$
Node 3	$[0, 2\pi]$	$[0, t_{max}]$	$[0, 1.00]$
Node 4	$[0, 2\pi]$	$[0, t_{max}]$	$[0, 1.00]$
Node 5	1.5π	$[0, t_{max}]$	1

TABLE 6.1: Table of parameters used in the optimisation. The values are presented in the bounds allowed to the optimiser. Variables coloured in red are fixed.

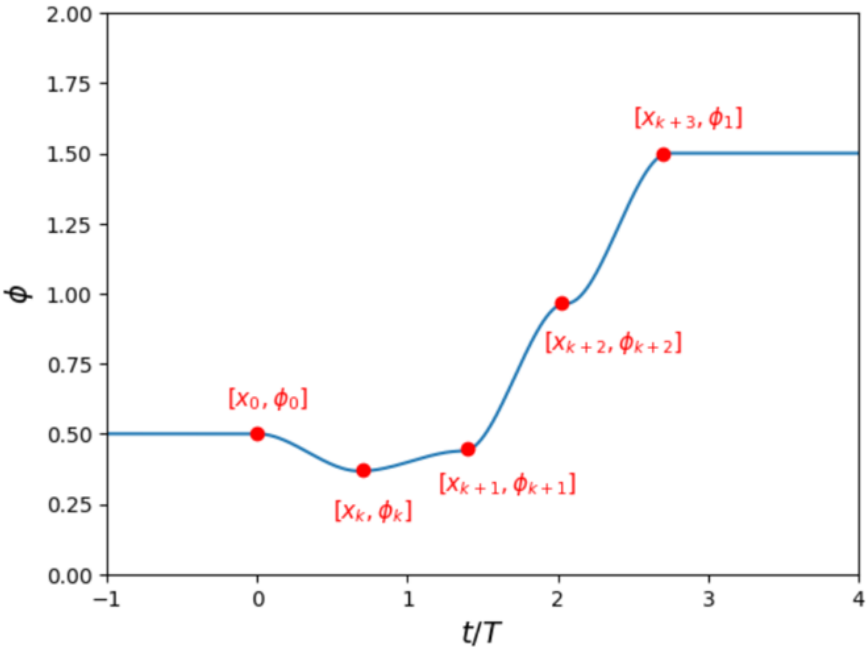

FIGURE 6.1: Schematics of the transition phase. The signal is constructed using Hermit spline, controlled by five nodes of different time (x) and ϕ values.

on a cost function, and the fittest individuals are kept for following iterations. The candidates are later combined and mutated to generate diversity in the sample and to explore new possibilities. There are three requirements for the optimiser: a set of variables to modify, a cost or reward function, and optimisation constrains.

The variables used during the optimisation process are the (x_k, ϕ_k, c_k) coordinates of the nodes, as introduced at Table 6.1. All the components of the initial node, and the derivatives and ϕ values of the last one are fixed, but the rest of the variables are free to change. Two different optimisations will be conducted, based on t_{max}: one where the foil can take up to one cycle to transition, and a second where $t_{max} = 3t/T$, where t is the time, T is the motion period, and $t/T = 3$ represents three flapping cycles. Since we aim to replicate this Chapter experimentally, the maximum accelerations allowed to the optimiser during the transition manoeuvre are limited to one and a half times the instantaneous frequency of the foil in the pre-transition phase.

To continue the analysis conducted on Chapter 5 about the effects of the overall transition time (t_{max}), we prescribe two cases: one where t_{max} is limited to one flapping cycle, which will allow to a direct comparison with Chapter 5, and a second case where t_{max} is opened up to three flapping cycles.

The cost function used by the optimiser is based on the force model developed in Chapter 5. The model with wake information was accurate to estimate the C_L evolution of the foil. Here, the goal is to reduce the overall power used during the transition. For that purpose, we can use the C_L predictions to approximate the power as a combination of the normal force and the heaving velocity: $C_P^* = C_L cos(\alpha)\dot{h}$. This simplification assumes small α values neglecting the contributions of the $C_D sin(\alpha)$ and $M_Z\dot{\theta}$ to the overall power. Still, we assume that the qualitative characteristic of the optimisation will make the C_P^* approximation enough to optimise the kinematics. The cost function is defined as the overall power consumption during the transition cycle: $\int_{t=0}^{t=t_T} C_P\, dt$. The results of the simulation will be validated using the CFD solver LOTUS. All the results involving CFD simulations present the full power consumption, denoted as $C_P = P/(0.5U^3c)$, where $P = F_Y\dot{h} + M_Z\dot{\theta}$. The grid and characteristics of the solver are similar to those used at Chapter 5.

6.4 Results

6.4.1 Convergence analysis of the optimisations

To ensure that the optimisations are independent of the initial population, we perform three trials at random initial values. After receiving the optimal kinematics from the optimiser, we run a Lotus simulation to obtain the real forces developed by the foils. As seen at Figure 6.2, limiting the transition time to one cycle provides with an optimum trajectory almost independent of the initial condition, which could be explained due to the lack of options considering the constrains. Although the 3 cycles case is more spread, a good convergence is found. The next section presents a deeper analysis of the results obtained for each of the cases.

6.4.2 Optimised trajectories for a maximum transition time of one cycle

An evolution of the optimised trajectories obtained for a $t_{T,max} = 1t/T$ are presented at Figure 6.3. The figure includes the power cost evolution during the iteration process normalised with the value at the last iteration: Power cost$^* = 1 + \frac{C_P^*(iter) - C_P^*(iter_{last})}{C_P^*(iter_{last})}$ (grey). We conduct CFD simulations at selected iterations (coloured dots) to validate the performance of the force model and the optimiser. The figure contains the ϕ,$\dot{\phi}$ C_L and C_P evolution for each of the simulations. For comparison purposes, we include

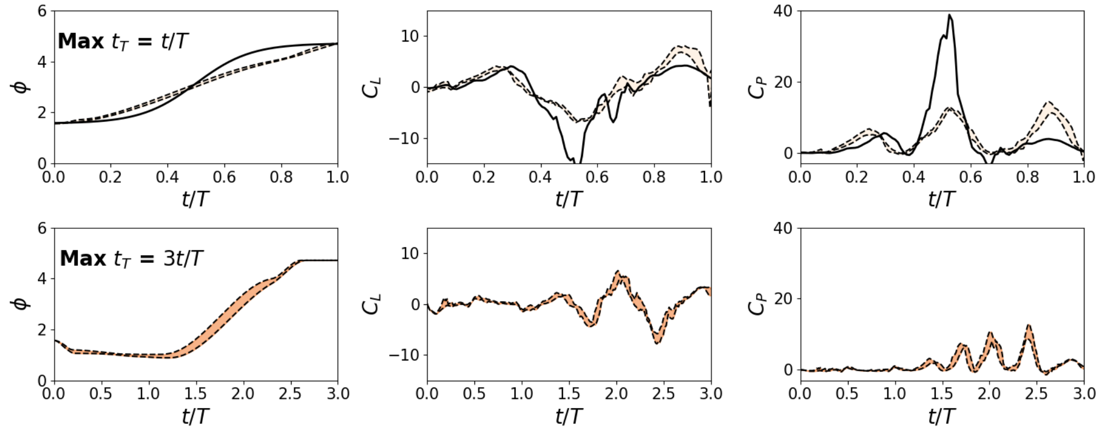

FIGURE 6.2: Instantaneous phasing ϕ, C_L and C_P results for different trials of the optimisation. The results are based on Lotus simulations conducted for the optimum trajectory recovered by the approach. The dashed-line at the top row presents an equivalent transition following a sigmoid evolution of ϕ, as described at Chapter 5. The top row introduces the results for a maximum transition time of one cycle. The bottom row presents the results for a maximum transition time of three cycles.

.

as dark dashed-line the kinematics and forces for an equivalent case with the transition motion described at Chapter 5. The validation performed with the CFD solver for various iterations suggests a good agreement with the optimiser. The force model used in this study is able to notice the reduction in power expense as the iteration process advances. The shape of the transition proposed by the optimiser suggests that, in order to reduce the power cost during the transition cycle, the foil needs to execute a quasi-linear manoeuvre. By doing so, the accelerations are spread across the cycle, reducing the maximum peaks in the forces suffered by the foil. This smoother way of manoeuvring is leading towards a constant power production across the transition phase. While the old way of manoeuvring was focusing the efforts towards the mid-point of the cycle, generating a large C_P peak at $t/T = 0.5$, the optimised trajectory promotes two power peaks of equal size. Overall, the total transition cost is reduced by 12%.

While the overall optimisation process has been validated against Lotus simulations, we still need to look into the performance of the force model. As described before, we are using an idealised version of the power cost, based on predictions performed for the C_L force. Figure 6.4 presents a comparison between the estimations developed by the force model (purple) and CFD data, for both C_L and C_P. Chapter 5 already discussed the performance of the force model for the instantaneous lift coefficient, but it is still interesting to see how the model can extrapolate to a different set of kinematics. While some of the C_L peaks are underestimated, the trend of the predictions agrees well with the simulation data. A higher difference can be appreciated at the C_P components. As described at the methodology region, the optimiser is using an idealised version of the C_P. The lack of the drag component and the large effective angle of attack seen by the

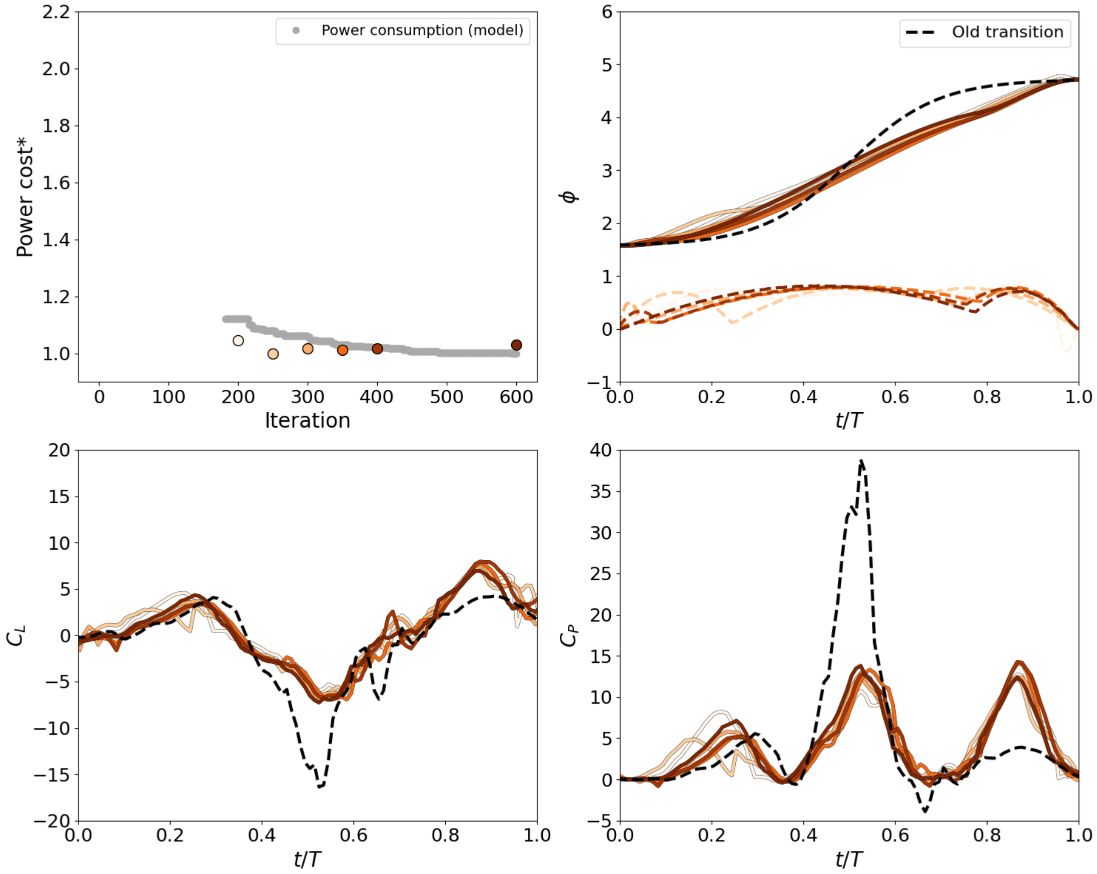

FIGURE 6.3: Optimised trajectories and forces for a maximum transition time of one cycle. Top-left compares the convergence process found by the optimiser (grey dots) against validation at selected iterations using Lotus (coloured dots). Top-right introduces the optimised transition kinematics (ϕ) and the instantaneous frequency $\dot{\phi}$. The trajectory is compared with a sigmoid evolution, as described at Chapter 5. The C_L and C_P evolution are shown at bottom-left and bottom-right sub-figures.

foil during the acceleration periods leads to an underestimation of the power cost when compared to the full C_P obtained with Lotus. Still, considering that the purpose of this study is to perform an optimisation, the idealised C_P projection, although with smaller absolute values, is able to reduce the power cost as the iteration process advances.

Overall, the optimisation process conducted for a maximum transition time of one flapping cycle has been able to reduce the overall power cost by 12%. Even when the optimisation has been conducted using an approximate version of the power, the approach is able to converge towards a minimum value. To evaluate the reasons behind the power reduction, we present at Figure 6.5 a comparison between the old kinematics and the optimised trajectory. The quasi-linear evolution of ϕ prescribed by the DE algorithm reduces the overall accelerations of the manoeuvre, leading to a lower C_P production during $t/T = 0.5$. At that time instant, the foil following a sigmoid evolution presents a large concentration on vorticity near the surface, leading to a large force production. As the foil is about to reach ϕ_1, the new trajectory induces a larger power

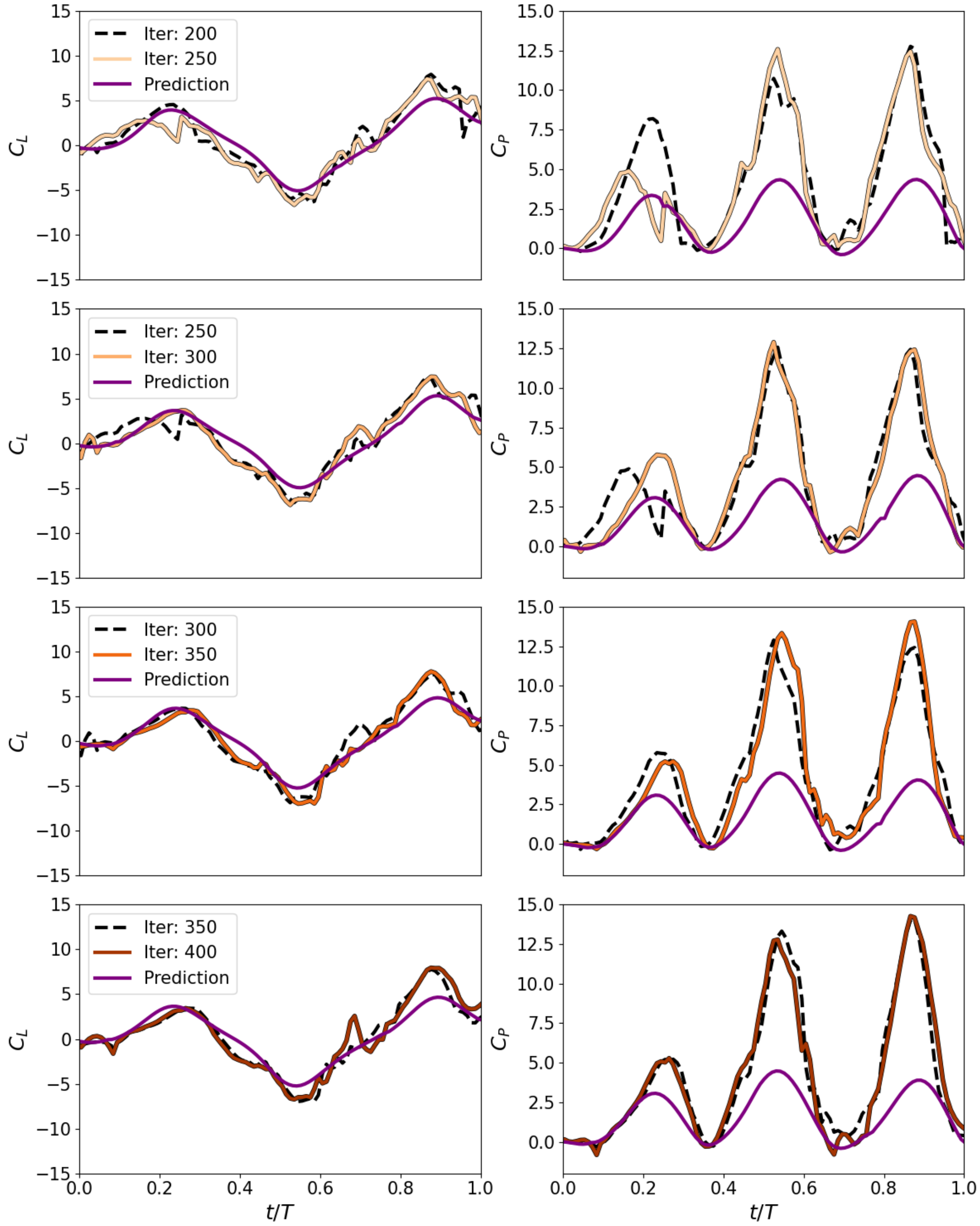

FIGURE 6.4: Comparison between the force model estimations for C_L and C_P^* (purple) and Lotus results (coloured lines) for C_L and C_P at different iterations.

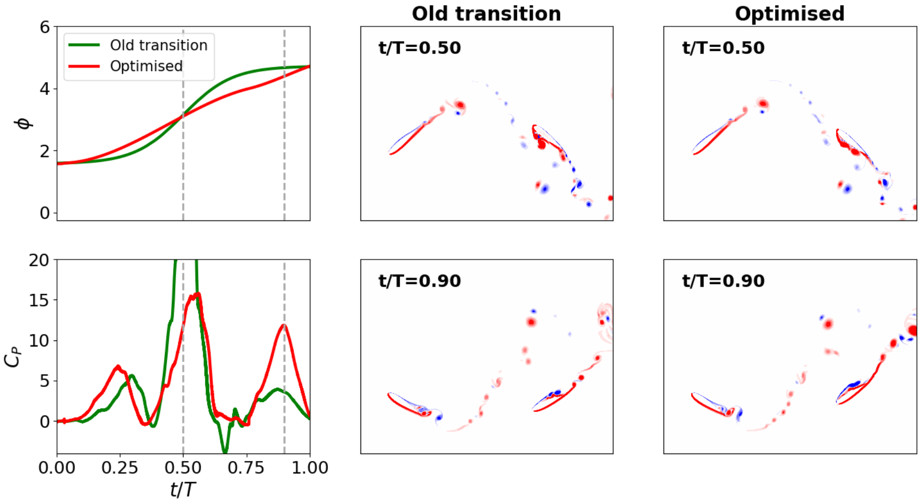

FIGURE 6.5: Instantaneous vorticity at two selected time instants for the transitions presented at Chapter 5 (green) and the optimised kinematics (Red)

consumption, but, as denoted before, a reduction of up to 12% in the overall expense is achieved.

6.4.3 Optimised trajectories for a maximum transition time of three cycles

An optimisation for a maximum transition time of one cycle has reduced the power cost for the transition motions prescribed at Chapter 5. In this section we allow the foil to take up to three cycles to reach the ϕ_1 state. In line with the previous section, we present at Figure 6.6 the convergence process of the optimiser, and we validate it with numerical data.

In line with the results for $t_{T,max} = 1t/T$, a good agreement can be appreciated between the optimiser convergence trajectory and the CFD validations. The main differences arise when analysing the optimised trajectory. First, it has to be noticed that the foil is not taking all the available time to transition, and is finding a $t_T = 2.65t/T$. The overall transition cost is penalised and, although slower manoeuvres could lead to smaller force peaks, they could involve a higher overall power expenditure. Second, while the previous section pointed out to a quasi-linear evolution of the ϕ component, when the maximum transition time is increased, the best trajectory recovered follows three distinctive stages: first, the foil starts a deceleration phase ($t/T = 0$ to $t/T = 1.3$). This is usually associated with negative power generation, which could minimise the overall cost Bluman et al. (2018). Next, the trajectory presents two acceleration parts separated by a second deceleration stage at $t/T = 2.3$.

To analyse the reasons behind the division in the acceleration stage, we compare at Figure 6.7 the optimised kinematics with an equivalent signal that reaches ϕ_1 in one

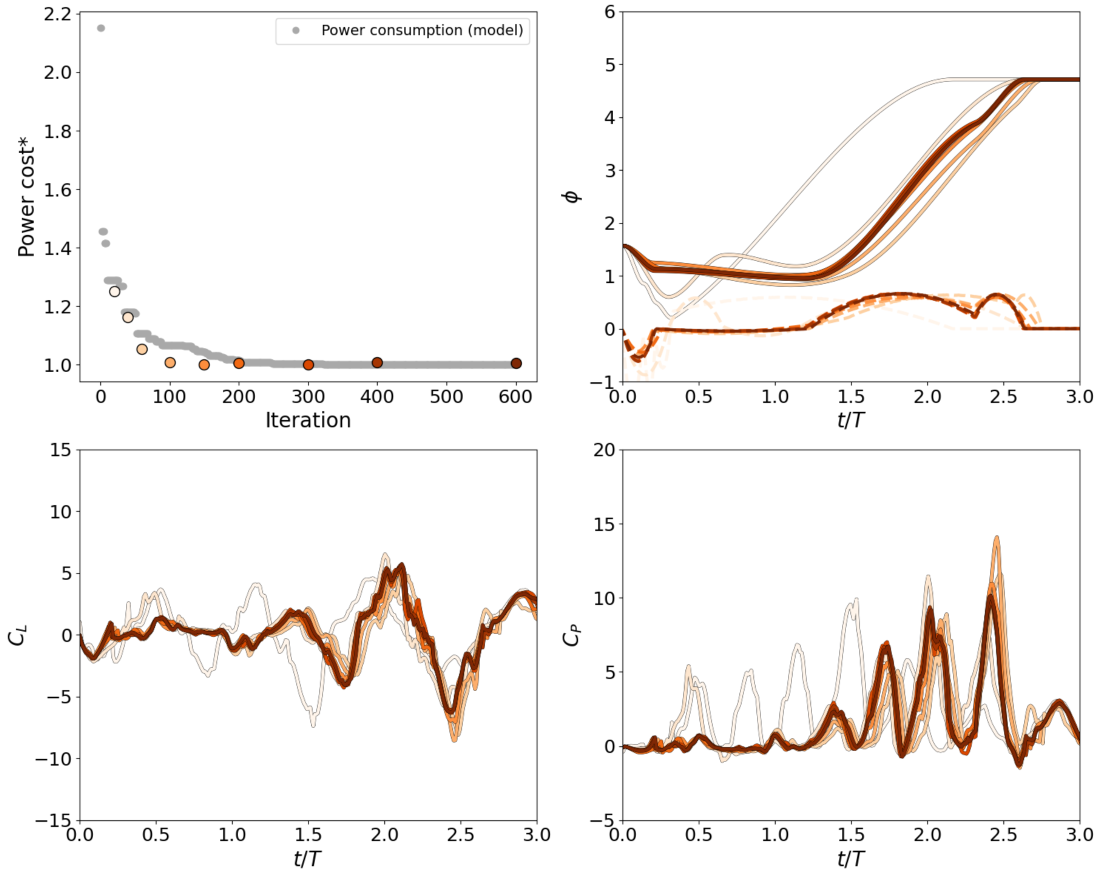

FIGURE 6.6: Optimised trajectories and forces for a maximum transition time of three cycles. Top-left compares the convergence process found by the optimiser (grey dots) against validation at selected iterations using Lotus (coloured dots). Top-right introduces the optimised transition kinematics (ϕ) and the instantaneous frequency $\dot{\phi}$. The trajectory is compared with a sigmoid evolution, as described at Chapter 5. The C_L and C_P evolution are shown at bottom-left and bottom-right sub-figures.

step. The C_P evolution shows that, at $t/T = 2.03$, executing a deceleration in the motion can reduce the maximum C_P production. At that time step, the foils are at maximum effective angle of attack (α), corresponding to maximum forces production. By slightly reducing the transition frequency, the 5 control case can limit the accelerations in the motion at that instant, leading to a lower power consumption. A stronger LEV for the 3 control, still attached to the surface of the foil, can be observed at the instantaneous $t/T = 2.03$, promoting the stronger forces suffered by the body. On the other hand, and to recover for the time used to decelerate, after $t/T = 2.4$, the 5 control case needs to perform a second acceleration, generating a higher C_P than the 3 control case. A mild reduction of 2.5% in the overall C_P cost is observed for the 5 control case across the presented ϕ evolution.

In the following section, we focus on understanding the overall shape of the optimised kinematics by slightly modifying the coordinates of the control points found by the optimiser.

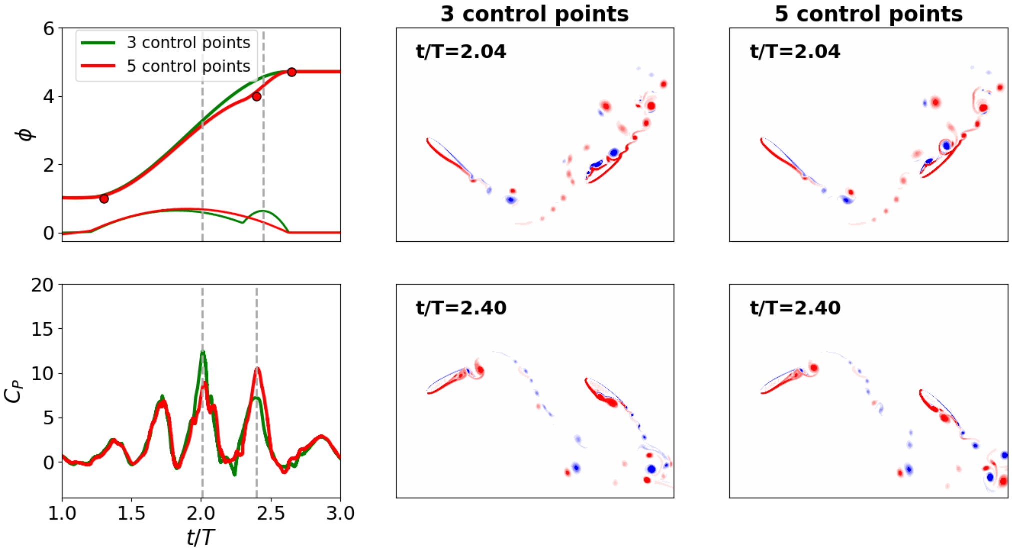

FIGURE 6.7: Comparison of the forces and flow fields for equivalent transition cases with 3 control points (green), and 5 control points (red). Top left figure introduces the ϕ and $\dot{\phi}$ evolution. Bottom left introduces the C_P evolution. The instantaneous vorticity is shown at the time steps denoted by vertical dashed lines.

6.4.4 Sensitivity analysis of the trajectory control points

As described before, the optimiser is finding for a $t_{T,max} = 3t/T$ a trajectory signal with three distinctive phases. A first stage when the foil decelerates, followed by two acceleration parts. In this section we aim to analyse the importance of those stages for the power reduction of the manoeuvre. Figure 6.8 introduces variations performed in the control points. By slightly modifying the x and ϕ values of the control points that prescribe the three distinctive stages of the cycle, we aim to understand the reasons behind the parameters found by the optimisation. The first row presents the modifications in the parameters of the control point that establishes the intermediate stage between accelerations. The black line corresponds to the optimised trajectory, while each of the coloured lines introduces a new transition based on a modification of the control point coordinates. We have changed both the location at which the crank appear, and the ϕ value of the stopping point. At the second row we perform a similar analysis, but focused on the control point that dominates the deceleration part of the cycle. In a similar manner as before, we vary the coordinates of the control points, and perform a CFD simulation for each of the new trajectories.

Figure 6.9 introduces the results for the first sensitivity analysis. The first row shows the x component variations, with the ϕ changes presented at the second row. The second column introduces the C_P signal for the transition period, and the third column compares the new trajectories against the optimised manoeuvre. Values below 1 indicate a better performance than the kinematics found by the optimiser.

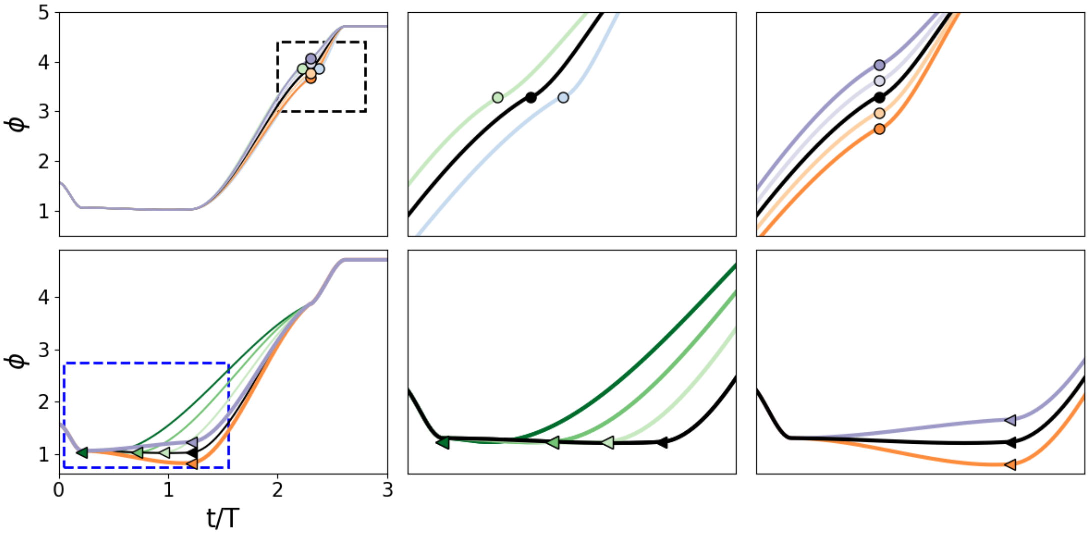

FIGURE 6.8: Sensitivity analysis conducted for the optimised trajectory. The first row presents the modifications on the coordinates of the fourth control node. The second row introduces the changes done on the coordinates of the third control node. Each of the new cases is run using the CFD solver

Advancing the time at which the transition crank occurs leads to a higher power consumption during the second cycle of the manoeuvre. By advancing the control point (green), the overall acceleration of the foil increases between $t/T = 1.3$ and $t/T = 2.3$. This effect leads to higher peaks before the crank. Although after the control point the instantaneous power is reduced (lower accelerations), the overall power cost $\overline{C_P^*}$ suggest that this case doesn't improve the performance of the optimised trajectory. By delaying the control point (blue), the foil is first reducing the accelerations, to then execute a faster motion. This effect leads to the opposite of the previous case. Lower initial peaks, and higher power consumption after the crank. The $\overline{C_P^*}$ value points towards a slight reduction in the overall power cost. Still, the accelerations of the new manoeuvre are beyond the threshold defined to the optimiser, which could explain why the optimiser didn't find a trajectory that appears to reduce even further the power cost.

Figure 6.10 introduces the sensitivity analysis for the control point that separates the deceleration/acceleration phases of the transition. In a similar manner, we introduces first the x variations, to conclude with the ϕ changes.

Varying the x location of the separation between acceleration/deceleration phases drastically modifies the shape of the transition signal. Instead of waiting until $t/T = 1.3$ to initiate the acceleration phase, now the foil is allowed to do it earlier. The first effect is clear at the instantaneous frequency evolution. The new cases are able to spread the motion across a longer period of time, reducing the maximum velocity prescribed to the foil. Still, the overall C_P^* appears to hold constant, pointing towards a different C_P distribution, but at the same overall cost. The last sensitivity study is conducted for ϕ variations in the control point. A small improvement of 2.5% is observed when the

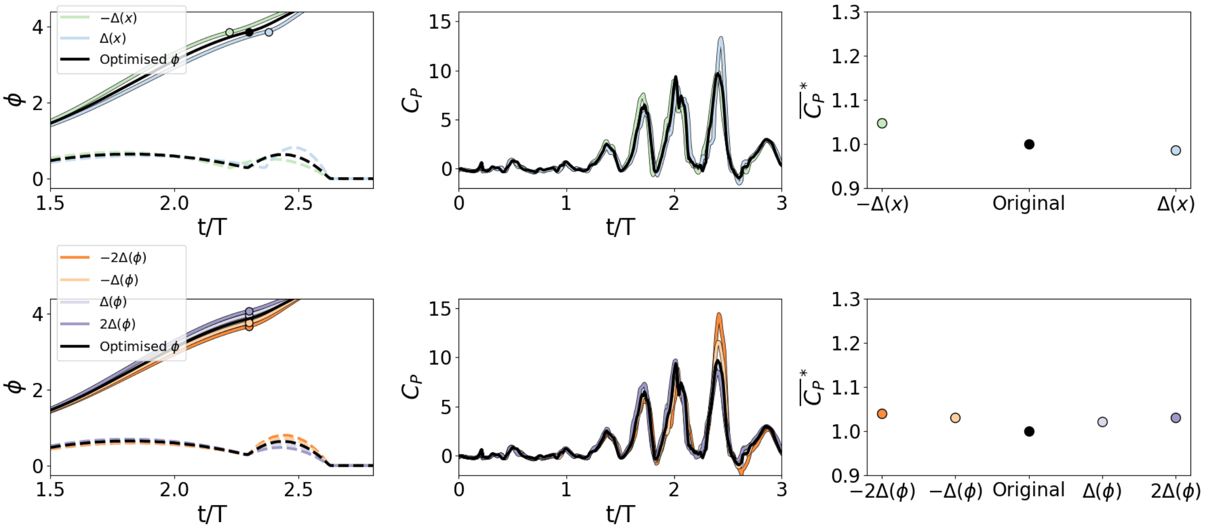

FIGURE 6.9: Results for the sensitivity analysis conducted at the node that controls the division in the acceleration stage. The black lines represent the base trajectory and forces. Each of the trajectories is run in Lotus, and the resultant C_P is presented here. The first column introduces the optimised and modified ϕ (continuous line) and $\dot{\phi}$ (dashed) evolution. The last column compares the obtained power cost compared to the optimum trajectory. The last column compares the obtained power cost compared to the optimum trajectory. Values below 1 represent an improvement in the power expense.

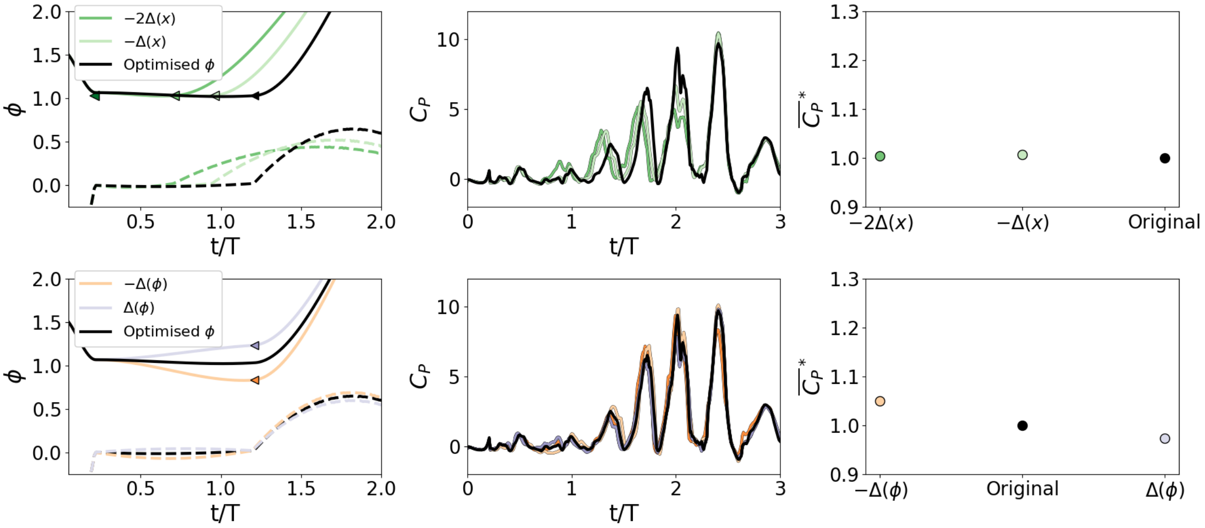

FIGURE 6.10: Results for the sensitivity analysis conducted at the node that controls the deceleration part of the trajectory. The black lines represent the base trajectory and forces. Each of the motions is run in Lotus, and the resultant C_P is presented here. The first column introduces the optimised and modified ϕ (continuous line) and $\dot{\phi}$ (dashed) evolution. The last column compares the obtained power cost compared to the optimum trajectory. Values below 1 represent an improvement in the power expense.

deceleration period is decreased (grey), which could suggest that, due to the underestimation of the large force peaks, the force model used by the optimiser is artificially augmenting the contribution of the negative $\dot{\phi}$ phase.

This section has analysed the optimum transition kinematics found by the optimiser for a maximum transition period of three cycles. By comparing the results with CFD simulations, it has been observed that the force model used during the process can generalise to different of kinematics, and still arrive to a decrease in the power used during the transition. This opens the path to future experimental implementations of real-life flapping control systems, able to maximise its propulsive performance, at the lowest power penalty.

6.5 Conclusions

In this study, we have optimised the manoeuvring motion executed by a flapping foil submerged in unsteady incoming flow. The study has been prescribed as two NACA0016 foils in tandem arrangement, where the hind foil executes a manoeuvring motion to maximise its propulsive performance. The manoeuvring motion has been defined as a variation of the phasing between the motion of the foil and the incoming wake. The evolution of ϕ has been prescribed as combination of Hermit splines, and a Differential Evolution approach has been used during the optimisation process. The cost function has been set as an approximation of the power, estimated using the force models developed at Chapter 5. When the maximum transition time is limited to one cycle, the optimiser recovers a trajectory characterised by a quasi-linear ϕ evolution, which controls the accelerations in the manoeuvre, and reduces the overall power consumption by 12% when compared to the equivalent case described at Chapter 5. The power reduction can be increased to 18% if the foil is allowed to take a maximum of three cycles to transition. The optimised trajectory contained three distinctive stages: a deceleration part, where negative power is recovered, followed by two acceleration steps. Finally, a sensitivity analysis of the optimum trajectory has been conducted, finding that the main reason behind the cost savings is linked to a more efficient distribution of the accelerations needed to perform the manoeuvre .This study provides a first insight into efficient ways of maximising the propulsive performance of flapping foils. As future work, we aim to implement this results experimentally, in an effort to develop real-time control applications based on efficient flapping foils.

Chapter 7

Conclusions

7.1 Conclusions

The aim of this thesis was defined as "to analyse the effects of surface texture and flow unsteadiness on the propulsive performance of flapping foils". During this research, we conducted numerical simulations and experiments aimed to provide a better understanding on the hydrodynamics of flapping foil, and to advance towards real-life control mechanisms able to maximise its performance under unsteady inflow conditions.

In Chapter 4 we analysed the influence of surface roughness on the propulsive performance of flapping foils. The use of bioinspired approaches to develop more efficient ways of propulsion has lead to several studies analysing the use of shark-skin textures for drag reduction purposes. Still, any potential benefit is highly dependent on the swimming conditions, or texture shape. To overcome these limitations, we selected a simplified denticle to generate the rough surfaces. We found that the addition of surface roughness was detrimental to thrust production and efficiency of a pitching foil, but we didn't observe major changes in the flow fields. We believe that the thrust reduction can be associated to an increase in the profile drag. To better analyse this effect, we conducted experiments of steady foils at various *Re* with the same roughness distribution. We observed that the unsteady regime is more robust to the effects of roughness across the *Re* range considered, which could be explained considering that other parameters like the kinematics or *St* might be neglecting the effects of the rough elements.

In Chapter 5 we studied the effects of incoming flow unsteadiness on the performance of a flapping foil. It is well known that the way the foil interacts with the incoming wake is strongly related to its propulsive performance. Swimming between vortices can lead to important performance benefits, but encountering those structures can be associated to large penalties. When the optimum path is unknown, we believe a recognition stage, where the foil explores several routes, is needed. To do so, we need rapid tools able to predict the forces evolution of a foil inside unsteady inflow conditions. In this chapter, we developed sparse force models using the approach SINDy. We found that the best accuracy in the models can be achieved by including relevant information, such as the foil kinematics or the location of the major vorticity structures. Also, incorporating physically-relevant inputs can lead to a better understanding of the physics of the problem. After constructing the force models, we tested the optimum route finding capabilities of the models by ranking a set of route candidates, based on lift production. We found that the model containing information about the wake was able to select the optimum path to follow with a correlation higher than 80% when compared to target data. Finally, we implemented experimentally the approach, finding a good correlation between the computational and experimental results. This study highlights the importance of carefully selecting the inputs to recover accurate governing equations for a flapping foil submerged inside unsteady flow. Also, the optimal route-finding capabilities open the path for a real-time control implementation that would maximise the performance of a flapping foil under unsteady circumstances, and at various flow conditions or flapping regimes.

In Chapter 6 we optimised the manoeuvring motion executed by a flapping foil submerged in unsteady incoming flow. Previous findings showed that a foil can maximise its propulsive performance by carefully manoeuvring towards optimum paths inside the unsteady incoming flow. Also, we analysed that those manoeuvrings could be highly-expensive in terms of power consumption. This increased cost effect can drastically impact, or even neglect, the potential benefits associated with the after-transition state, and, in this chapter, we analysed more efficient ways of executing the manoeuvre. To do so, we combine the use of a sparse force model with a Differential Evolution approach. The use of the force model was aimed to reduce the overall computational expense of the optimisation process. We find that the new manoeuvre can reduce the power consumption by 18% when compared to the original Chapter 5 reference case. To do so, the new transition comprehends a more efficient evolution of the accelerations, leading towards less cost manoeuvres.

In this thesis, we have focused on analysing the hydrodynamic effects of surface texture and unsteadiness on flapping foils. We have seen how those two conditions can affect the performance of a flapping foil, and we have advanced towards more efficient ways of swimming. We believe the results presented here provide an advancement about the knowledge behind tandem operations, and could serve towards real-life applications of flapping foils for propulsive augmentation, or control tools.

7.2 Future work

The main potential lines of investigation associated with this thesis are presented next:

- Real-time wake estimation tool: in this thesis, we found that providing information about the wake is essential to develop an accurate force model for a flapping foil inside unsteady conditions. Still, we provided the wake information as 'a-priori' data. A real-time recognition tool to estimate the location of the main vorticities with respect to the foil would be needed for a closed-loop implementation of the control approach.

- Experimental validation of the optimised kinematics: Chapter 6 presents a important improvement in the power cost of the manoeuvre required to maximise the performance of a flapping foil. Still, we believe that an experimental implementation would advance the research towards a real-life implementation of the procedure.

Appendix A

Physics-based and Machine learning predictions of maneuvering forces in unsteady inflow conditions

A.1 Introduction

Multi-vessel coordination and controlled maneuvering through upstream wakes is important to a wide range of marine applications; from surface ships to autonomous underwater vehicles. A proper understanding of the unsteadiness of the surrounding flow is essential, and it is a requirement for safety aspects or to develop operations involving several unmanned vehicles. Previous work has been done in the field of underwater vehicles manoeuvrability Kim et al. (2015) and ship-to-ship interactions Yu et al. (2019). In the biological area, studies have found important benefits in terms of travel performance in the case of fish-schooling Weihs (1973). What all the previous studies have in common is the importance of properly adapting to the surrounding environment in order to maximise the performance gains and to ensure a safe operation. To replicate this ability of fish to maneuver and take advantage of their unsteady upstream conditions, our engineered vessels need to be able to predict fluid forces in real-time.

As a model problem to study high-speed force predictions, we will investigate the unsteady forces on the back foil of a tandem flapping foil pair. In addition, tandem foils have been suggested for use in vessel manoeuvring because of their high force production capabilities Read et al. (2003). Several models have been developed to estimate the performance of a flapping foil. theodorsen1935 derived the first expressions for the forces time evolution to predict aerodynamic flutter. Garrick (1936), used the equations defined by Theodorsen to approximate the propulsive forces, and Lighthill (1969) completed the work done by Garrick applying its equations to a lunate tail of a fish. The main disadvantage of the previous methods is that they all assume small amplitude kinematic motions, rectilinear vortex wake and perfect fluid, conditions highly unlikely to be found in a real-world applications. A more complex scenario can be found in the tandem flapping foil operation, as one of those two objects is interacting with the wake of the other. If the motion of both bodies is properly tuned, the one in the back can achieve important performance gains. Muscutt et al. (2017a) Kurt and Moored (2018). muscutt2017performance predicted the performance of the mentioned hind foil by using a quasi-steady approach, providing accurate results in the cycle-averaged thrust production estimation, but not considering the real-time force signal prediction.

In the recent years, the use of Machine Learning (ML) for control, maneuvering and marine applications has greatly improved. Weymouth2013JOSR studied the applications of physics-based learning models (PBLM) to ship hydrodynamics. By the use of physical knowledge of the system, the authors improved the predictions obtained by simple regression models at a considerably less expense than high-resolution numerical predictions. Also, several ML tools have been developed for a vast range of applications, from text or image recognition, to forces prediction. Of especial interest for this study are two black-box approaches - where the output is complex and difficult to understand by the user -. The first one is the long short-term memory neural network (LSTM), able to interpret data in a temporal context Hochreiter and Schmidhuber (1997). By the use of previous system data, LSTM models can predict future states Chollet et al. (2018) Marban et al. (2019). The second approach is the Neural Ordinary Differential Equations (NODE) Chen et al. (2018), that can provide time-series approximation and predictions when the data is irregularly sampled or insufficient Rubanova et al. (2019). Another ML approach, this time in the "physics-based" ML group, is the Sparse Identification of Nonlinear Dynamical systems (SINDy) Brunton et al. (2016a), where user-interpretable governing equations can be prescribed.

In this study, we analyse several methods in order to develop a model able to estimate the performance of a flapping foil under unsteady upstream conditions. In Section 2, the problem definition is explained. Several flapping foil tandem configurations have been simulated, and the forces and flow conditions faced by the hind foil recorded, to later serve both as inputs for the models and as target. In Section 3, two physics-based approaches, the quasi-steady and Theodorsen models, are adapted in order to include the effects of the unsteadiness of the upstream flow. Next, in Section 4, we develop three Machine Learning models, LSTM, NODE and SINDy. In section 5, we study the capabilities of all five models and evaluate them against data obtained with an in-house CFD software. The predictive performance, in terms of time-signal estimation and prediction error is studied, and the limitations of the models discussed.

A.2 Problem definition and data generation

Our model problem for maneuvering in unsteady inflow conditions is a tandem foil configuration, as described at Figure 2.3. We define c as the chord length of the foil, $a = c/4$ is the pivoting point location for the pitching motion, $b = c/2$ is half the chord of the foil, U_∞ is the free-stream velocity and $h(t), \theta(t)$ are the heave and pitch of the foil, defined as

$$h(t) = A\sin(2\pi f t + \phi) \tag{A.1}$$

$$\theta(t) = \theta_{max}\cos(2\pi f t + \phi) \tag{A.2}$$

where $A = c$ is the heaving amplitude, f is the flapping frequency, and ϕ represents the phasing in the motion between the two foils. Finally, two other parameters need to be introduced. The first one is the Strouhal number $St = 2Af/U_\infty$ and the Reynolds number $Re_c = U_\infty c/v$,where v is the fluid kinematic viscosity. In this work we use $Re_c = 7000$ and $St = 0.3 - 0.5$ to match previous tandem foil studies Muscutt et al. (2017a).

The effective angle of attack of the back foil α depends on the uniform flow, the heave velocity and on the unsteady inflow conditions produced by the motion of the front foil

$$\alpha = \arctan\left(\frac{-\dot{h} - v_\gamma}{U_\infty + u_\gamma}\right) + \theta \tag{A.3}$$

where u_γ and v_γ are the horizontal and vertical velocity components induced by the vorticity of the upstream wake.

A range of tandem configurations are tested in order to study the effectiveness of the prediction methods for different foil-wake interactions. The varied parameters are the foils relative phase ϕ and their longitudinal spacing S. As discovered by Muscutt et al. (2017a), the combination of the previous parameters will have a strong influence in the performance of the hind foil and two specific setups have been selected as a test cases for the different force prediction approaches. The first one corresponds to a High-Performance hind foil (St=0.3, ϕ=1π, S=c), or a foil able to extract energy from the wake of the leader, and hence to achieve a performance augmentation. The hind foil has minimal interaction with the vortex structures of the fore-foil in this case. The second case is Low-Performance hind foil (St=0.3, ϕ=π, S=2.5c), where much less thrust is generated because the flow is strongly disrupted by the upstream vortex structures.

An in-house CFD solver is used to generate the benchmark data to study this system. This solver uses the Boundary Data Immersion Method (BDIM,Weymouth and Yue

TABLE A.1: Numerical cases

St value	0.3, 0.4, 0.5
Spacing	0.5, 1 ,1.5 ,2 ,2.5 ,3 ,3.5 ,4 ,4.5 ,5
Phasing	0π, 0.25π ,0.50π ,0.75π ,0π ,1.25π ,1.5π ,1.750π
Number of simulations	240 tandem cases

(2011)) to simulate the time-evolution of the viscous Navier-Stokes using a convolution over the fluid and any immersed dynamic geometries. The convergence of this method is quadratic, and has been previously validated for flapping foil systems in several studies Maertens and Weymouth (2015); Lagopoulos et al. (2019); Zurman-Nasution et al. (2021a). A rectangular Cartesian mesh is used with a grid spacing of $\Delta X = \Delta Y = c/192$ near the foils and in the inter-foil region with grid stretching used in the outer fluid domain. This is the same gird used and validated in Lagopoulos et al. (2019).

The CFD method was used to simulate a broad range of test conditions for the model problem defined above, Table A.1. For each of the tandem cases, the performance of the hind foil, in terms of the time histories of the force along the x-axis C_X=$2F_X/(\rho U_\infty^2 c)$ and the transverse force C_Y=$2F_Y/(\rho U_\infty^2 c)$, are recorded and used to assess the performance estimation models. In addition, the unsteady "inflow" velocity conditions u_γ, v_γ to the downstream foil are recorded for use in some the maneuvering force models.

A.3 Physics-based performance estimation approaches

This section covers two theoretical estimations, starting with a simple quasi-steady approach, and progressing towards a more complex model with foundations in Garrick and Theodorsen's analysis. In both methods, the effects of the flow unsteadiness has been introduced via the information gathered about the foil surroundings.

A.3.1 Quasi-steady model

Following Muscutt et al. (2017a), a baseline quasi-steady model for the instantaneous lift on the downstream flapping foil is defined as

$$C_L = -2\pi\alpha \tag{A.4}$$

where the local α is defined in Equation (A.3). Projecting this into the horizontal and vertical axis, C_Y and C_X are obtained as

$$C_Y = C_L cos(\theta - \alpha) \tag{A.5}$$

$$C_X = C_L sin(\theta - \alpha) \tag{A.6}$$

A.3.2 Adapted Theodorsen model

The second physics-based approach is developed from the work of Theodorsen and Mutchler (1935) and Garrick et al. (1937) for small amplitude unsteady foil motions. The unsteady lift force a foil in a uniform inflow (such as the upstream foil) is modelled as

$$L = -\rho b^2 (U\pi\dot{\theta} + \pi\ddot{h} - \pi b a\ddot{\theta}) - 2\pi\rho U b C(k)\left[U\theta + \dot{h} + b(1/2 - a)\dot{\theta}\right] \tag{A.7}$$

where Theodorsen's function $C(k)$ is a transfer function relating sinusoidal inputs of reduced frequency to their aerodynamic response Brunton and Rowley (2009) Theodorsen and Mutchler (1935).

To modify this function for unsteady inflow, we augment the vertical velocity produced by the heaving motion of the body $\dot{h}$ with the velocity induced by the wake along the transverse direction v_γ, and augment the horizontal inflow velocity U with the wake induced velocity u_γ. Combining this with the appropriate values of a, b and using our definition of the effective back foil angle of attack α gives the adapted version of equation A.7 for the back foil as

$$C_L = -\frac{c\pi}{2U}\left(\dot{\alpha} + \frac{c\ddot{\theta}}{4U}\right) - 2\pi\left(\alpha + \frac{c\dot{\theta}}{2U}\right) \tag{A.8}$$

This value of C_L can then be used to obtain the transverse force using,

$$C_Y = C_L cos(\theta - \alpha) \tag{A.9}$$

The propulsive force can be obtained using Garrick (1936),

$$C_X = C_L\theta + \frac{\pi S_x^2}{U^2} \tag{A.10}$$

Here S_x is the leading-edge suction component developed in Garrick (1936):

$$S_x = \frac{\sqrt{2}}{2}\left[2C(k)Q - \frac{c\dot{\theta}}{2}\right], \text{ where, } Q = U\alpha + \frac{c\dot{\theta}}{2} \tag{A.11}$$

To perform the predictions based on the equations presented before, an approach based on the work done by Muscutt et al. (2017a) has been carried out. It can be appreciated that all the parameters are in relation either to the kinematics of the foil, or to the upstream flow. And it is of special relevance that the second group can be defined by the velocity components, u_γ, v_γ, imposed by the wake on the foil, and the motion of the same body. In a normal approach, it would require of n-number of simulations to record the information needed for n-tandem cases, which would be computationally expensive. Instead, here we present what we have called "virtual probes simulation", presented schematically at Fig. A.1

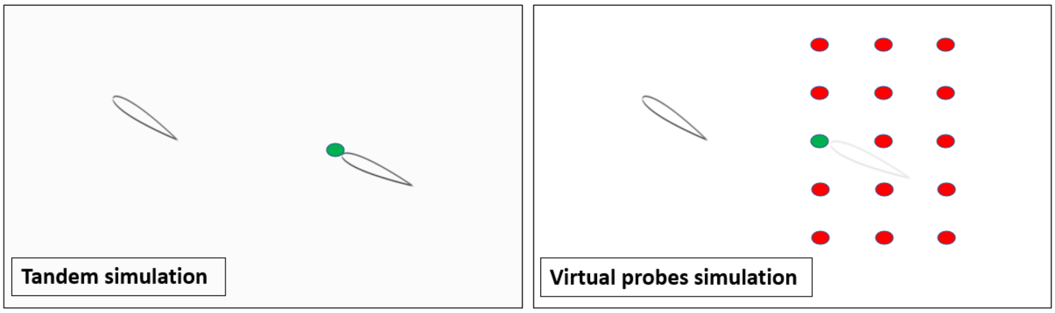

FIGURE A.1: Sketch and comparison of the virtual probes method and the tandem simulations. The red and green dots indicate virtual probes acting and moving as virtual hind foils. The red dot in the left hand size of the figure helps to represent that the virtual dots are place at the LE of their equivalent foil.

The left part of Fig. A.1 presents the classical disposition of a tandem simulation, where both the hind and fore foil are physically modelled. The right part of Fig. A.1 introduces the equivalent to the mentioned tandem. First, a virtual probe - in order to avoid disturbances to the flow - is placed in the location where the hind foil would have been (see green dot at Fig. A.1). Next, this probe is configured with the same kinematics as its equivalent in the tandem configuration. Finally, the powerful part of the method relies in the fact that not only, but multiple, virtual hind foils can be set-up in just one simulation. If each of the red dots of Fig. A.1, is prescribed with a different Spacing/Phasing with respect to the leader foil, in just one simulation, it is possible to acquire information for n hind foils, making the physics based models presented in this section computationally cheap.

A.4 Machine Learning performance estimation approaches

In this section, we study the use of three machine learning models predictions, LSTM, ODE and SINDy, for the C_X and C_Y force coefficients to complement the approximate physical models described above.

Note that the physical parameters used to predict the forces are: the effective angle of attack of the foil, α, the local pitch angle with respect to the x-axis, θ, U, and the derivatives $\dot{\alpha}$, $\dot{\theta}$ and $\ddot{\theta}$. In order to keep simplicity in the ML model, and due to its small contribution to the total forces, the term $\ddot{\theta}$ has been discarded as an input, but the rest, together with C_X and C_Y are used to to define the state vector Z for the ML models, see Table A.2. Choosing physically-relevant instantaneous flow metrics as the inputs for the ML models should help them generalize to the unseen test cases Weymouth and Yue (2013).

TABLE A.2: Machine Learning models: state vector

Z(t) =	$[U(\mathrm{t})\,,\alpha(\mathrm{t})\,,\dot{\alpha}(\mathrm{t})\,,\theta(\mathrm{t})\,,\dot{\theta}(\mathrm{t})\,,C_X(\mathrm{t})\,,C_Y(\mathrm{t})]$

TABLE A.3: LSTM parametric study

Input Layer	$Z(t_0)$, Table A.2
LSTM layer	Hidden Units [16,32,64,128,256]
Drop Out layer	DR [0.2,0.5,0.8,No DO]
Output Layer	$Z(t_0 + \Delta t)$, Table A.2

A.4.1 LSTM

The Long Short-Term Memory (LSTM) method, developed by Hochreiter and Schmidhuber (1997) is suitable for this analysis as it can pass the information obtained at a given state, or $x(t)$ to the next iteration. By doing so, it can estimate the state of a given parameter at a $(t + \Delta(t)$ time step, what makes the model suitable for predictive - and maneuverability - applications.

The LSTM model, developed using the package Keras Chollet et al. (2018), is trained using pieces of the time-signal inputs, also known as windows, where the goal is to predict the state of the same inputs, but ahead in time. In this study, 10 time step involving roughly a cycle period $t/T = 0.1$ have been used as an input in order to predict the next $t/T = 0.1$ of the cycle, in a moving prediction until the full cycle is covered. Due to the characteristics of this study, where the goal is to achieve a first approximation to ML for manoeuvring applications, no other windows shapes have been considered. Finally, the model takes into account all the variables and combines them in order to obtain the output layer but, as this is essentially a black-box model, the interpretation of the resulting model is not straightforward. Nevertheless, it is important that the network is provided with useful and physics-meaningful data, in order to achieve a result suitable for real applications.

The aim of this part of the study is not to obtain the best-fitted LSTM model with respect to the target data, but to perform a characterisation and sensitivity analysis of the main model parameters. Considering that the number of aspects that can be varied in a LSTM model is vast, only the key ones have been selected: first, the Hidden Units (HU), and second, the Dropout Rate (DR). Both have been used in other LSTM applications as the network varying parameters Chollet et al. (2018) Marban et al. (2019). To maintain the model as simple as possible, only one LSTM layer has been used. A summary of the whole model can be see in the table below:

TABLE A.4: Neural ODE parametric study

Input Layer	$Z(t_0)$, Table A.2
RNN layer (encoder)	Hidden Layer [1], Hidden Units [25]
Latent ODE layer	Hidden Layer [1], Hidden Units [16,32,64,128,256]
Decoder layer	Hidden Layer [1], Hidden Units [20]
Output Layer	$Z(t_0 + \Delta t)$, Table A.2

The combination of the drop out rates and Hidden Unites evolves to a total of 20 cases. All of them will be analysed later in the discussion of results, and the best of those in terms of accuracy, will be compared with the findings obtained with the theoretical approach explained earlier in this section. The model has been trained with 160 cases, and tested with two selected cases not seen by the model during the training. All the models use an "adam" optimizer.

A.4.2 Neural ODE

The Neural Ordinary Differential Equations (NODE) approach, developed by chen2018 obtains an output layer solution by solving an ODE initial value problem with the use of a black-box differential equation solver. The details of the approach are described at Chapter 3.

A.4.3 SINDy

The last machine learning method that is going to be used in this study is the Sparse Identification of Nonlinear Dynamics (SINDy) Brunton and Rowley (2009). The details of the approach are described at Chapter 3

In this study, the package *PySINDy* de Silva et al. (2020) has been used. As part of the definition of the model, a second-degree differentiation has been established, together with a third-degree polynomial order as the feature library. In terms of the optimiser, and considering that it is this part where the interpretability of the output models is going to be defined, two different options have been applied. The first one, where the optimizer is a simple Ordinary Least Squares (OLS), and the second one, that uses a LASSO regression ($\alpha = 2$). The next table details both model conditions. The main difference is going to rely in the amount of parameters that conform the model equations, and will be explained in the results sections.

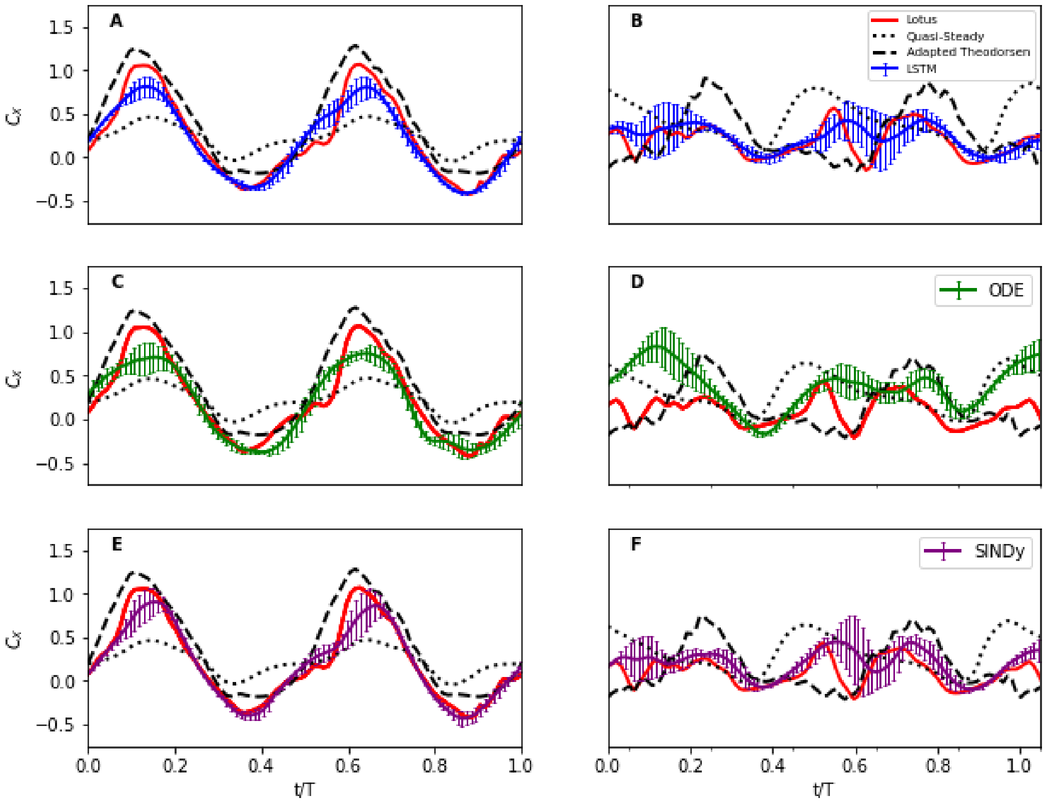

FIGURE A.2: Time signal prediction comparison for the HP case. HP test case at the left column and LP test case at the right column. LSTM results (A and B), NODE results (C and D) and SINDy (LASSO) results (E and F).

A.5 Results

This section introduces the results obtained with the methods presented in the previous chapter. As explained in the methodology, the models have been tested against two test cases, one corresponding to a High-Performance hind foil, in which the level of unsteadiness is reasonably low, and another one, a Low-Performance foil where, due to the strong body-wake interactions, the unsteadiness of the flow is considerably higher.

First, the time signal estimation for a full flapping cycle is presented. Due to the predictive approach followed for the LSTM, SINDy and ODE methods, a rolling average has been computed with the evaluations at each of the data points, and is introduced together with the standard deviation. Like so, it can be possible to appreciate whether the average estimation is accurate, but also to ascertain its stability over time. The real - and target - data obtained with Lotus is presented together with the quasi-steady and adapted Theodorsen models, and selected cases of the LSTM, Neural ODE and SINDy parametric sweep.

It is clear from Figure A.2 that the quasi-steady approach does not fit properly the evolution of the C_X obtained by Lotus. It is surprising how, even when the time signal clearly differs, the cycle-averaged thrust value would be close to the real estimation, which proves that a correct modelling of cycle-averaged quantities is not sufficient for a manoeuvring model. The adapted Theodorsen, on the other hand, seems to collapse between with the CFD results, although it can not model properly the areas of the cycle where the thrust production is negative. As expected, the prediction is considerably more accurate for the HP case than for the LP, as will be seen later in this section.

The LSTM model, Fig A.2 a) and b) appears to capture properly the peak thrust value of the HP test case and the drag-generating parts of the cycle. Although LSTM does not augment the accuracy of the Adapted Theodorsen, the results presented here have to be understood as a first approach to ML techniques. It will be the aim of further work to develop a more consistent method. About the LP test case, the LSTM method appears to capture better the sudden peaks appearing in the CFD signal, caused due to the high unsteady interactions between the foil and the upstream flow, improving the predictions of the Adapted Theodorsen. The second conclusion that can be extracted from the LSTM figure is that the stability of the predictions, represented by the confidence intervals, is in line with the mean thrust estimation, and decreases as the complexity of the model increases.

About the Neural ODE model, part c) and d) of Fig. A.2, it can be seen how, for the HP and LP case, the NODE approach appears to collapse better with the target data than the quasi-steady approach, and is close to the Theodorsen predictions, although it has not been able to improve the predictions of the LSTM network. In line with the results presented above, the complexity of the LP test case falls outside of what this Neural ODE model can achieve. On the other hand, the stability of the predictions is higher than the LSTM result, especially at the LP test case.

The SINDy output where a LASSO optimizer has been defined is presented at Fig. A.2 e) and f). Following the trend of the previous LSTM and Neural ODE, the approach performs considerably better than the quasi-steady model, but does not augment the prediction of the adapted Theodorsen, at least for the HP case. The size of the errorbars, indicator of the stability of the predictions, is in line with the LSTM results, and bigger than for the Neural ODE case, especially at the LP case.

Next, in order to evaluate all the methods together, the Normalised Root-Mean-Square Error (NRMSE) is presented:

$$NRMSE = \frac{RMSE}{y_{max} - y_{min}} \tag{A.12}$$

Where y_{max} and y_{min} correspond to the maximum and minimum of the Lotus test case C_X and C_Y predictions. The data presented here is the NRMSE result for a full flapping cycle.

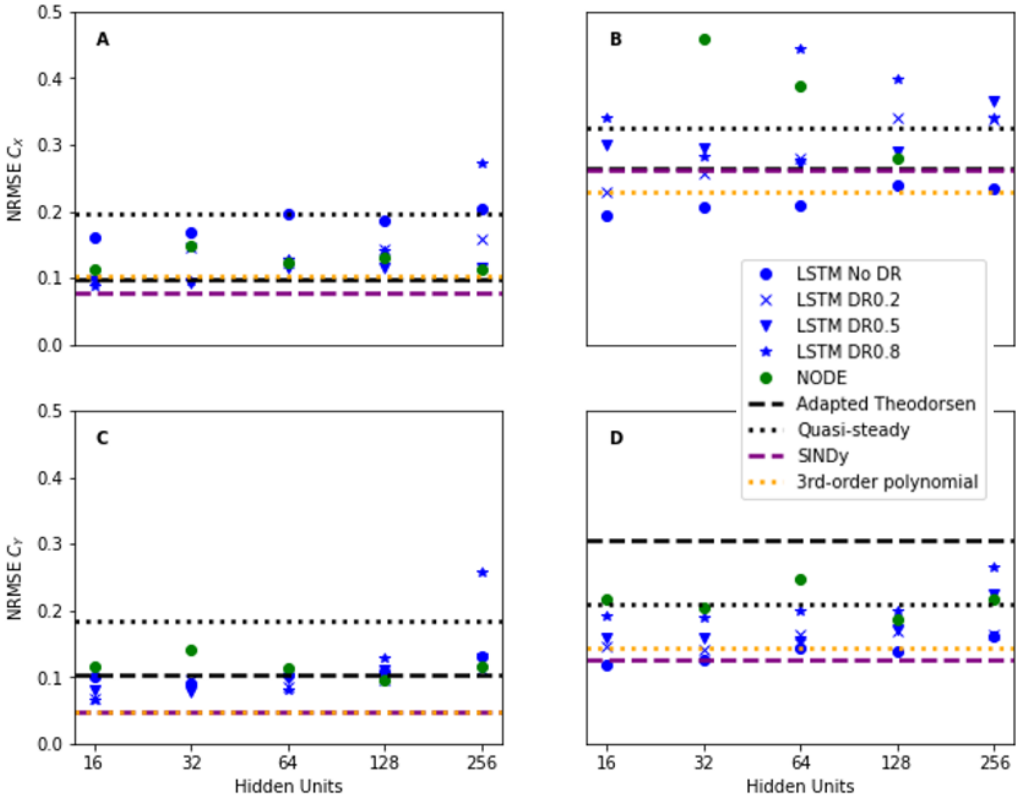

FIGURE A.3: NRMSE comparison. HP test case at the left column and LP test case at the right column. C_X (A and B) and C_Y (C and D)

As explained before, the methods developed in this study are compared against two test cases, one involving a High-Performance Hind foil, and another representing a Low-Performance scenario. Figure A.3 introduces the NRMSE comparison for both cases.

About the quasi-steady and Adapted Theodorsen models, It can be seen in the previous figure how both are obtaining a lower NRMSE for the HP test case than for the LP test. Considering that both theoretical approaches were limited in their original design to a tight range of parameters, especially quasi-steady flow conditions Theodorsen and Mutchler (1935) Garrick (1936), the mentioned result does not come as a surprise. The adapted Theodorsen has been able to obtain, for all the cases but the LP C_Y, a better prediction than the simple quasi steady, especially at the thrust estimation (9% NRMSE error the first one and 20% the second at the HP C_X).

About the LSTM results, and starting with the sensitivity analysis, the amount of Hidden Units (HU) does not appear to have a strong influence in the overall result, although for most of the cases, there is a slight trend indicating that networks with few HU could be beneficial, which could be due to a better dealing with overfitting in the training phase. The Neural ODE approach appears to be less sensitive to the variation of the hidden units than the LSTM.

For the HP test cases, neither the LSTM or the Neural ODE models can increase the accuracy of the adapted Theodorsen. About the LP case, the situation is the opposite, as both LSTM and Neural ODE methods are improving the accuracy of the adapted Theodorsen (originally around 27% error against around 20% for the LSTM and 22% for NODE). Although the ML approaches are not better than the theoretical models - in terms of prediction accuracy - for all scenarios, they can be more stable for a wider range of cases, especially when the unsteadiness increases, what highlights the potential of these methods.

Although it may appear that the OLS SINDy obtains the best prediction, especially at the LP test case (near 21% error), a simple look at the output model can reject it's application. It was explained in the methodology section that the purpose of SINDy was to obtain an interpretable output model, that could lead to knowledge gain about the physics behind the foil-wake interactions but, when using an OLS optimiser, SINDy outputs a C_X' equation with more than 91 parameters. On the other hand, if a LASSO optimizer is applied, the second SINDy model, the decrease in accuracy is considerably high (especially at the HP), but the amount of terms in the C_X' model goes down to 8.

A.6 Conclusions

In this study, several methods have been analysed to develop a high-speed maneuvering model able to estimate the performance of a flapping foil under unsteady upstream conditions. Two physics-based approaches, a simple quasi-steady and a Theodorsen and Garrick approach have been adapted in order to account for the upstream flow unsteadiness. Three machine learning models have been designed and trained, an LSTM, a Neural ODE, and a SINDy model. The physic-based and ML models have been compared against two test cases obtained using full CFD simulations.

While the quasi-steady approach has not provided accurate outputs, the adapted Theodorsen equation has achieved an error of around 9% with respect to the CFD data in the less-complex test case. On the other hand, as the unsteadiness increases, the accuracy quickly goes down, reaching an error of almost 26% for the low performance case.

It was found that both the LSTM and SINDy machine learning could match the the accuracy of the adapted Theodorsen for the less-complex test case, the SINDY with 91 parameters achieving 8% error and LSTM achieving around 9% in its best attempt. On the other hand, all the ML models can improve on the accuracy of the adapted Theodorsen in the more unsteady test case, with a best case 20% and 25% error for the LSTM and NODE respectively. The SINDy model is able to reduce the error to only 20% when allowed to use 91 parameters. However, when SINDy with LASSO optimization is used to produce an human-interpretable 8-parameter model, the error jumps up to 27%.

In conclusion, the potential of ML techniques to predict the forces on manoeuvring vehicles in unsteady inflow conditions has been demonstrated , especially when the unsteadiness is strong enough to make simple theory-based approaches unreliable. The ML models have proven to be more suitable to be applied for a wider range of conditions than the adapted theoretical approaches, which highlights their potential for manoeuvrability applications.

Acknowledgments

This research was supported financially by the Office of Naval Research award N62909-18-1-2091. The authors want to acknowledge the support of the University of Southampton's School of Engineering and The Alan Turing Institute.

References

Abrahams, M. V. and Colgan, P. W. Risk of predation, hydrodynamic efficiency and their influence on school structure. *Environmental Biology of Fishes*, 13:195–202, 1985.

Achenbach, E. Influence of surface roughness on the cross-flow around a circular cylinder. *Journal of fluid mechanics*, 46(2):321–335, 1971.

Afroz, F., Lang, A., Habegger, M. L., Motta, P., and Hueter, R. Experimental study of laminar and turbulent boundary layer separation control of shark skin. *Bioinspiration & biomimetics*, 12(1):016009, 2016.

Ahlborn, B., Harper, D. G., Blake, R. W., Ahlborn, D., and Cam, M. Fish without footprints. *Journal of Theoretical Biology*, 148(4):521–533, 1991.

Akhtar, I., Mittal, R., Lauder, G. V., and Drucker, E. Hydrodynamics of a biologically inspired tandem flapping foil configuration. *Theoretical and Computational Fluid Dynamics*, 21:155–170, 2007.

Alexander, D. E. Unusual phase relationships between the forewings and hindwings in flying dragonflies. *Journal of Experimental Biology*, 109(1):379–383, 1984. ISSN 0022-0949. URL `https://jeb.biologists.org/content/109/1/379`.

Anderson, J. M., Streitlien, K., Barrett, D., and Triantafyllou, M. S. Oscillating foils of high propulsive efficiency. *Journal of Fluid mechanics*, 360:41–72, 1998.

Ashraf, M., Young, J., and Lai, J. Reynolds number, thickness and camber effects on flapping airfoil propulsion. *Journal of Fluids and structures*, 27(2):145–160, 2011.

Baik, Y. S., Bernal, L. P., Granlund, K., and Ol, M. V. Unsteady force generation and vortex dynamics of pitching and plunging aerofoils. *Journal of Fluid Mechanics*, 709: 37–68, 2012.

Bakken, O. M., Krogstad, P.-Å., Ashrafian, A., and Andersson, H. I. Reynolds number effects in the outer layer of the turbulent flow in a channel with rough walls. *Physics of Fluids*, 17(6), 2005.

Bandyopadhyay, P. R., Castano, J., Rice, J., Philips, R., Nedderman, W., and Macy, W. Low-speed maneuvering hydrodynamics of fish and small underwater vehicles. 1997.

Barenblatt, G. I. *Scaling*, volume 34. Cambridge University Press, 2003.

Bechert, D., Bruse, M., Hage, W. v., Van der Hoeven, J. T., and Hoppe, G. Experiments on drag-reducing surfaces and their optimization with an adjustable geometry. *Journal of fluid mechanics*, 338:59–87, 1997.

Bechert, D., Bruse, M., and Hage, W. Experiments with three-dimensional riblets as an idealized model of shark skin. *Experiments in fluids*, 28(5):403–412, 2000.

Bixler, G. D. and Bhushan, B. Fluid drag reduction with shark-skin riblet inspired microstructured surfaces. *Advanced Functional Materials*, 23(36):4507–4528, 2013.

Blank, J. and Deb, K. Pymoo: Multi-objective optimization in python. *Ieee access*, 8: 89497–89509, 2020.

Bluman, J. E., Pohly, J. A., Sridhar, M. K., Kang, C.-k., Landrum, D. B., Fahimi, F., and Aono, H. Achieving bioinspired flapping wing hovering flight solutions on mars via wing scaling. *Bioinspiration & Biomimetics*, 13(4):046010, 2018.

Bohl, D. G. and Koochesfahani, M. M. Mtv measurements of the vortical field in the wake of an airfoil oscillating at high reduced frequency. *Journal of Fluid Mechanics*, 620:63, 2009.

Boschitsch, B. M., Dewey, P. A., and Smits, A. J. Propulsive performance of unsteady tandem hydrofoils in an in-line configuration. *Physics of Fluids*, 26(5), 2014.

Broering, T. M. and Lian, Y.-S. The effect of phase angle and wing spacing on tandem flapping wings. *Acta Mechanica Sinica*, 28:1557–1571, 2012.

Brunton, S. and Rowley, C. Modeling the unsteady aerodynamic forces on small-scale wings. In *47th AIAA aerospace sciences meeting including the new horizons forum and aerospace exposition*, page 1127, 2009.

Brunton, S. L., Proctor, J. L., and Kutz, J. N. Discovering governing equations from data by sparse identification of nonlinear dynamical systems. *Proceedings of the national academy of sciences*, 113(15):3932–3937, 2016a.

Brunton, S. L., Proctor, J. L., and Kutz, J. N. Sparse identification of nonlinear dynamics with control (sindyc). *IFAC-PapersOnLine*, 49(18):710–715, 2016b.

Brunton, S. L., Budišić, M., Kaiser, E., and Kutz, J. N. Modern koopman theory for dynamical systems. *arXiv preprint arXiv:2102.12086*, 2021.

Carr, L., Mcalister, K., and Mccroskey, W. Analysis of dynamic oscillating the development stall based on airfoil experiments. *NASA Tech. Rep*, 1977.

Chen, R. T., Rubanova, Y., Bettencourt, J., and Duvenaud, D. Neural ordinary differential equations. *arXiv preprint arXiv:1806.07366*, 2018.

Chollet, F. et al. *Deep learning with Python*, volume 361. Manning New York, 2018.

Chowdhury, H., Loganathan, B., Wang, Y., Mustary, I., and Alam, F. A study of dimple characteristics on golf ball drag. *Procedia engineering*, 147:87–91, 2016.

Darwin, C. and Bynum, W. F. *The origin of species by means of natural selection: or, the preservation of favored races in the struggle for life*. AL Burt New York, 2009.

Das, A., Shukla, R. K., and Govardhan, R. N. Existence of a sharp transition in the peak propulsive efficiency of a low-pitching foil. *Journal of Fluid Mechanics*, 800:307–326, 2016.

Das, A., Shukla, R. K., and Govardhan, R. N. Foil locomotion through non-sinusoidal pitching motion. *Journal of Fluids and Structures*, 89:191–202, 2019.

de Silva, B. M., Champion, K., Quade, M., Loiseau, J.-C., Kutz, J. N., and Brunton, S. L. Pysindy: A python package for the sparse identification of nonlinear dynamics from data. *arXiv preprint arXiv:2004.08424*, 2020.

Dean, B. and Bhushan, B. Shark-skin surfaces for fluid-drag reduction in turbulent flow: a review. *Philosophical Transactions of the Royal Society A: Mathematical, Physical and Engineering Sciences*, 368(1929):4775–4806, 2010.

DeLaurier, J. and Harris, J. Experimental study of oscillating-wing propulsion. *Journal of Aircraft*, 19(5):368–373, 1982.

Deng, J., Sun, L., Teng, L., Pan, D., and Shao, X. The correlation between wake transition and propulsive efficiency of a flapping foil: A numerical study. *Physics of Fluids*, 28 (9), 2016.

Dewey, P. A., Boschitsch, B. M., Moored, K. W., Stone, H. A., and Smits, A. J. Scaling laws for the thrust production of flexible pitching panels. *Journal of Fluid Mechanics*, 732:29–46, 2013.

Domel, A. G., Domel, G., Weaver, J. C., Saadat, M., Bertoldi, K., and Lauder, G. V. Hydrodynamic properties of biomimetic shark skin: effect of denticle size and swimming speed. *Bioinspiration & biomimetics*, 13(5):056014, 2018a.

Domel, A. G., Saadat, M., Weaver, J. C., Haj-Hariri, H., Bertoldi, K., and Lauder, G. V. Shark skin-inspired designs that improve aerodynamic performance. *Journal of the Royal Society Interface*, 15(139):20170828, 2018b.

Drucker, E. G. and Lauder, G. V. Locomotor function of the dorsal fin in teleost fishes: experimental analysis of wake forces in sunfish. *Journal of Experimental Biology*, 204 (17):2943–2958, 2001.

Du, Z., Li, H., Cao, Y., Wan, X., Xiang, Y., Lv, P., and Duan, H. Control of flow separation using biomimetic shark scales with fixed tilt angles. *Experiments in Fluids*, 63(10):1–12, 2022.

Ehrmann, R. S., Wilcox, B., White, E. B., and Maniaci, D. C. Effect of surface roughness on wind turbine performance. Technical report, Sandia National Lab.(SNL-NM), Albuquerque, NM (United States), 2017.

Eloy, C. Optimal strouhal number for swimming animals. *Journal of Fluids and Structures*, 30:205–218, 2012.

Fasel, U., Kutz, J. N., Brunton, B. W., and Brunton, S. L. Ensemble-sindy: Robust sparse model discovery in the low-data, high-noise limit, with active learning and control. *Proceedings of the Royal Society A*, 478(2260):20210904, 2022.

Fernandez-Feria, R. and Sanmiguel-Rojas, E. Effect of the pivot point location on the propulsive performance of a pitching foil. *Journal of Fluids and Structures*, 97:103089, 2020.

Gad-el Hak, M. and Bushnell, D. M. Separation control: Review. *Journal of Fluids Engineering*, 113:5–30, 1991.

Garrick, I. Propulsion of a flapping and oscillating airfoil. *Report National Advisory Committee for Aeronautics, NACA Report*, (567):419–427, 1936.

Garrick, I. et al. Propulsion of a flapping and oscillating airfoil. *NACA report*, 567: 419–427, 1937.

Geder, J. D., Ramamurti, R., Viswanath, K., and Pruessner, M. Underwater thrust performance of tandem flapping fins: Effects of stroke phasing and fin spacing. In *OCEANS 2017-Anchorage*, pages 1–7. IEEE, 2017.

Gehrke, A., de Guyon-Crozier, G., and Mulleners, K. Genetic algorithm based optimization of wing rotation in hover. *Fluids*, 3(3):59, 2018.

Gerrard, J. The mechanics of the formation region of vortices behind bluff bodies. *Journal of fluid mechanics*, 25(2):401–413, 1966.

Gravish, N., Peters, J. M., Combes, S. A., and Wood, R. J. Collective flow enhancement by tandem flapping wings. *Physical review letters*, 115(18):188101, 2015.

Gunnarson, P., Mandralis, I., Novati, G., Koumoutsakos, P., and Dabiri, J. O. Learning efficient navigation in vortical flow fields. *Nature communications*, 12(1):7143, 2021.

Guo, P., Zhang, K., Yasuda, Y., Yang, W., Galipon, J., and Rival, D. E. On the influence of biomimetic shark skin in dynamic flow separation. *Bioinspiration & Biomimetics*, 16 (3):034001, 2021.

Heathcote, S., Wang, Z., and Gursul, I. Effect of spanwise flexibility on flapping wing propulsion. *Journal of Fluids and Structures*, 24(2):183–199, 2008.

Hochreiter, S. and Schmidhuber, J. Long short-term memory. *Neural computation*, 9(8): 1735–1780, 1997.

Hover, F., Haugsdal, Ø., and Triantafyllou, M. Effect of angle of attack profiles in flapping foil propulsion. *Journal of Fluids and Structures*, 19(1):37–47, 2004.

Isogai, K., Shinmoto, Y., and Watanabe, Y. Effects of dynamic stall on propulsive efficiency and thrust of flapping airfoil. *AIAA journal*, 37(10):1145–1151, 1999.

Iverson, D., Rahimpour, M., Sakai, M., Kiwata, T., and Oshkai, P. Effect of chord-wise flexibility on propulsive performance of oscillating foils. In *FIV2018 Conference*, 2018.

Jeanmonod, G. and Olivier, M. Effects of chordwise flexibility on 2d flapping foils used as an energy extraction device. *Journal of Fluids and Structures*, 70:327–345, 2017.

Kato, N. Control performance in the horizontal plane of a fish robot with mechanical pectoral fins. *IEEE journal of oceanic engineering*, 25(1):121–129, 2000.

Kim, M., Joe, H., Kim, J., and Yu, S.-c. Integral sliding mode controller for precise manoeuvring of autonomous underwater vehicle in the presence of unknown environmental disturbances. *International Journal of Control*, 88(10):2055–2065, 2015.

Kinsey, T. and Dumas, G. Parametric study of an oscillating airfoil in a power-extraction regime. *AIAA journal*, 46(6):1318–1330, 2008.

Kumar, A. and Hu, H. An experimental investigation on the wake flow characteristics of tandem flapping wings. In *6th AIAA theoretical fluid mechanics conference*, page 3120, 2011.

Kurt, M. and Moored, K. W. Flow interactions of two-and three-dimensional networked bio-inspired control elements in an in-line arrangement. *Bioinspiration & biomimetics*, 13(4):045002, 2018.

Kurt, M., Eslam Panah, A., and Moored, K. W. Flow interactions between low aspect ratio hydrofoils in in-line and staggered arrangements. *Biomimetics*, 5(2):13, 2020.

Lagopoulos, N. S. *Investigation of single and tandem flapping hydrofoils*. PhD thesis, University of Southampton, 2021.

Lagopoulos, N., Weymouth, G., and Ganapathisubramani, B. Universal scaling law for drag-to-thrust wake transition in flapping foils. *Journal of Fluid Mechanics*, 872, 2019.

Lagopoulos, N., Weymouth, G., and Ganapathisubramani, B. Deflected wake interaction of tandem flapping foils. *Journal of Fluid Mechanics*, 903:A9, 2020.

Li, Y., Liu, T., Wang, Y., and Xie, Y. Deep learning based real-time energy extraction system modeling for flapping foil. *Energy*, 246:123390, 2022.

Licht, S., Polidoro, V., Flores, M., Hover, F., and Triantafyllou, M. Design and projected performance of a flapping foil auv. *IEEE Journal of Oceanic Engineering*, 29(3):786–794, 2004a. .

Licht, S., Polidoro, V., Flores, M., Hover, F. S., and Triantafyllou, M. S. Design and projected performance of a flapping foil auv. *IEEE Journal of oceanic engineering*, 29(3): 786–794, 2004b.

Lighthill, M. Hydromechanics of aquatic animal propulsion. *Annual review of fluid mechanics*, 1(1):413–446, 1969.

Lin, X., Wu, J., Zhang, T., and Yang, L. Phase difference effect on collective locomotion of two tandem autopropelled flapping foils. *Physical Review Fluids*, 4(5):054101, 2019.

Lissaman, P. and Shollenberger, C. A. Formation flight of birds. *Science*, 168(3934): 1003–1005, 1970.

Liu, X., Si, S., Cao, Q., Kumar, S., and Hsieh, C.-J. Neural sde: Stabilizing neural ode networks with stochastic noise. *arXiv preprint arXiv:1906.02355*, 2019a.

Liu, Z., Bhattacharjee, K. S., Tian, F.-B., Young, J., Ray, T., and Lai, J. C. Kinematic optimization of a flapping foil power generator using a multi-fidelity evolutionary algorithm. *Renewable energy*, 132:543–557, 2019b.

Long Jr, J. H., Schumacher, J., Livingston, N., and Kemp, M. Four flippers or two? tetrapodal swimming with an aquatic robot. *Bioinspiration & Biomimetics*, 1(1):20, 2006.

Lu, K., Xie, Y., and Zhang, D. Numerical study of large amplitude, nonsinusoidal motion and camber effects on pitching airfoil propulsion. *Journal of Fluids and Structures*, 36:184–194, 2013.

Lua, K. B., Lu, H., Zhang, X., Lim, T., and Yeo, K. Aerodynamics of two-dimensional flapping wings in tandem configuration. *Physics of Fluids*, 28(12), 2016.

Lupandin, A. Effect of flow turbulence on swimming speed of fish. *Biology Bulletin*, 32 (5):461–466, 2005.

Mackowski, A. and Williamson, C. Direct measurement of thrust and efficiency of an airfoil undergoing pure pitching. *Journal of Fluid Mechanics*, 765:524–543, 2015.

Mackowski, A. and Williamson, C. Effect of pivot location and passive heave on propulsion from a pitching airfoil. *Physical Review Fluids*, 2(1):013101, 2017.

Maertens, A. P. and Weymouth, G. D. Accurate cartesian-grid simulations of near-body flows at intermediate reynolds numbers. *Computer Methods in Applied Mechanics and Engineering*, 283:106–129, 2015.

Mallah, S. R., Sooraj, P., Sharma, A., and Agrawal, A. Effect of superhydrophobicity on the wake of a pitching foil across various strouhal numbers. *Physics of Fluids*, 33(11): 111905, 2021.

Marban, A., Srinivasan, V., Samek, W., Fernández, J., and Casals, A. A recurrent convolutional neural network approach for sensorless force estimation in robotic surgery. *Biomedical Signal Processing and Control*, 50:134–150, 2019.

Medjroubi, W., Stoevesandt, B., Carmo, B., and Peinke, J. High-order numerical simulations of the flow around a heaving airfoil. *Computers & Fluids*, 51(1):68–84, 2011.

Muscutt, L., Weymouth, G., and Ganapathisubramani, B. Performance augmentation mechanism of in-line tandem flapping foils. *Journal of Fluid Mechanics*, 827:484–505, 2017a.

Muscutt, L. *The hydrodynamics of plesiosaurs*. PhD thesis, University of Southampton, 2017.

Muscutt, L. E., Dyke, G., Weymouth, G. D., Naish, D., Palmer, C., and Ganapathisubramani, B. The four-flipper swimming method of plesiosaurs enabled efficient and effective locomotion. *Proceedings of the Royal Society B: Biological Sciences*, 284(1861): 20170951, 2017b.

Nudds, R. L., Taylor, G. K., and Thomas, A. L. Tuning of strouhal number for high propulsive efficiency accurately predicts how wingbeat frequency and stroke amplitude relate and scale with size and flight speed in birds. *Proceedings of the Royal Society of London. Series B: Biological Sciences*, 271(1552):2071–2076, 2004.

Oeffner, J. and Lauder, G. V. The hydrodynamic function of shark skin and two biomimetic applications. *Journal of Experimental Biology*, 215(5):785–795, 2012.

Ol, M. Vortical structures in high frequency pitch and plunge at low reynolds number. In *37th AIAA Fluid Dynamics Conference and Exhibit*, page 4233, 2007.

Ol, M. V., Bernal, L., Kang, C.-K., and Shyy, W. Shallow and deep dynamic stall for flapping low reynolds number airfoils. *Animal locomotion*, pages 321–339, 2010.

Park, H. and Choi, H. Kinematic control of aerodynamic forces on an inclined flapping wing with asymmetric strokes. *Bioinspiration & Biomimetics*, 7(1):016008, 2012.

Pitcher, T., Magurran, A., and Winfield, I. Fish in larger shoals find food faster. *Behavioral Ecology and Sociobiology*, 10:149–151, 1982.

Platzer, M. F., Jones, K. D., Young, J., and Lai, J. C. Flapping wing aerodynamics: progress and challenges. *AIAA journal*, 46(9):2136–2149, 2008.

Polet, D. T., Rival, D. E., and Weymouth, G. D. Unsteady dynamics of rapid perching manoeuvres. *Journal of Fluid Mechanics*, 767:323–341, 2015.

Price, K. V. Differential evolution. In *Handbook of optimization: From classical to modern approach*, pages 187–214. Springer, 2013.

Ramananarivo, S., Godoy-Diana, R., and Thiria, B. Rather than resonance, flapping wing flyers may play on aerodynamics to improve performance. *Proceedings of the National Academy of Sciences*, 108(15):5964–5969, 2011.

Ratti, J. and Vachtsevanos, G. High endurance, micro aerial surveillance and reconnaisance robot. In *2011 IEEE Conference on Technologies for Practical Robot Applications*, pages 1–6. IEEE, 2011.

Read, D. A., Hover, F., and Triantafyllou, M. Forces on oscillating foils for propulsion and maneuvering. *Journal of Fluids and Structures*, 17(1):163–183, 2003.

Rival, D., Hass, G., and Tropea, C. Recovery of energy from leading-and trailing-edge vortices in tandem-airfoil configurations. *Journal of Aircraft*, 48(1):203–211, 2011.

Rohr, J. J. and Fish, F. E. Strouhal numbers and optimization of swimming by odontocete cetaceans. *Journal of Experimental Biology*, 207(10):1633–1642, 2004.

Rohr, J., Hendricks, E., Quigley, L., Fish, F., Gilpatrick, J., and Scardina-Ludwig, J. Observations of dolphin swimming speed and strouhal number. *Space and Naval Warfare Systems Center Technical Report 1769*, 1998.

Rubanova, Y., Chen, R. T., and Duvenaud, D. Latent ordinary differential equations for irregularly-sampled time series. 2019.

Sagol, E., Reggio, M., and Ilinca, A. Issues concerning roughness on wind turbine blades. *Renewable and sustainable energy Reviews*, 23:514–525, 2013.

Salta, M., Wharton, J. A., Stoodley, P., Dennington, S. P., Goodes, L. R., Werwinski, S., Mart, U., Wood, R. J., and Stokes, K. R. Designing biomimetic antifouling surfaces. *Philosophical Transactions of the Royal Society A: Mathematical, Physical and Engineering Sciences*, 368(1929):4729–4754, 2010.

Sampath, K., Geder, J. D., Ramamurti, R., Pruessner, M. D., and Koehler, R. Hydrodynamics of tandem flapping pectoral fins with varying stroke phase offsets. *Physical Review Fluids*, 5(9):094101, 2020.

Scherer, J. O. Experimental and theoretical investigation of large amplitude oscillating foil propulsion systems. Technical report, Hydronautics, Incorporated, 1968.

Schnipper, T., Andersen, A., and Bohr, T. Vortex wakes of a flapping foil. *Journal of Fluid Mechanics*, 633:411–423, 2009.

Schouveiler, L., Hover, F., and Triantafyllou, M. Performance of flapping foil propulsion. *Journal of fluids and structures*, 20(7):949–959, 2005.

Senturk, U. and Smits, A. J. Reynolds number scaling of the propulsive performance of a pitching airfoil. *Aiaa Journal*, 57(7):2663–2669, 2019.

Shyy, W., Berg, M., and Ljungqvist, D. Flapping and flexible wings for biological and micro air vehicles. *Progress in aerospace sciences*, 35(5):455–505, 1999.

Soueid, H., Guglielmini, L., Airiau, C., and Bottaro, A. Optimization of the motion of a flapping airfoil using sensitivity functions. *Computers & Fluids*, 38(4):861–874, 2009.

Streitlien, K. and Triantafyllou, G. On thrust estimates for flapping foils. *Journal of fluids and structures*, 12(1):47–55, 1998.

Sun, C., Tian, T., Zhu, X., and Du, Z. Sparse identification of nonlinear unsteady aerodynamics of the oscillating airfoil. *Proceedings of the Institution of Mechanical Engineers, Part G: Journal of Aerospace Engineering*, 235(7):809–824, 2021.

Taylor, G. K., Nudds, R. L., and Thomas, A. L. Flying and swimming animals cruise at a strouhal number tuned for high power efficiency. *Nature*, 425(6959):707–711, 2003.

Theodorsen, T. and Mutchler, W. General theory of aerodynamic instability and the mechanism of flutter. 1935.

Thomas, A. L., Taylor, G. K., Srygley, R. B., Nudds, R. L., and Bomphrey, R. J. Dragonfly flight: free-flight and tethered flow visualizations reveal a diverse array of unsteady lift-generating mechanisms, controlled primarily via angle of attack. *Journal of Experimental Biology*, 207(24):4299–4323, 2004.

Triantafyllou, G. S., Triantafyllou, M. S., and Grosenbaugh, M. A. Optimal thrust development in oscillating foils with application to fish propulsion. *Journal of Fluids and Structures*, 7(2):205–224, 1993.

Triantafyllou, M. S., Triantafyllou, G., and Yue, D. Hydrodynamics of fishlike swimming. *Annual review of fluid mechanics*, 32(1):33–53, 2000.

Triantafyllou, M., Triantafyllou, G., and Gopalkrishnan, R. Wake mechanics for thrust generation in oscillating foils. *Physics of Fluids A: Fluid Dynamics*, 3(12):2835–2837, 1991.

Tuncer, I., Walz, R., and Platzer, M. A computational study on the dynamic stall of a flapping airfoil. In *16th AIAA applied aerodynamics conference*, page 2519, 1998.

Van Bokhorst, E., De Kat, R., Elsinga, G. E., and Lentink, D. Feather roughness reduces flow separation during low reynolds number glides of swifts. *Journal of Experimental Biology*, 218(20):3179–3191, 2015.

Van Buren, T., Floryan, D., Quinn, D., and Smits, A. Nonsinusoidal gaits for unsteady propulsion. *Physical Review Fluids*, 2(5):053101, 2017.

Verma, S., Novati, G., and Koumoutsakos, P. Efficient collective swimming by harnessing vortices through deep reinforcement learning. *Proceedings of the National Academy of Sciences*, 115(23):5849–5854, 2018.

Vilumbrales-Garcia, R., Weymouth, G. D., and Ganapathisubramani, B. Physics-based and machine learning predictions of maneuvering forces in unsteady inflow conditions. In *The 9th Conference on Computational Methods in Marine Engineering (Marine 2021)*, 2022.

Vilumbrales-Garcia, R., Kurt, M., Weymouth, G. D., and Ganapathisubramani, B. Effects of surface roughness on the propulsive performance of pitching foils. *arXiv preprint arXiv:2301.03942*, 2023.

Walsh, M. Turbulent boundary layer drag reduction using riblets. In *20th aerospace sciences meeting*, page 169, 1982.

Weihs, D. Hydromechanics of fish schooling. *Nature*, 241(5387):290–291, 1973.

Weihs, D. Some hydrodynamical aspects of fish schooling. *Swimming and Flying in Nature: Volume 2*, pages 703–718, 1975.

Weimerskirch, H., Martin, J., Clerquin, Y., Alexandre, P., and Jiraskova, S. Energy saving in flight formation. *Nature*, 413(6857):697–698, 2001.

Wen, L., Weaver, J. C., and Lauder, G. V. Biomimetic shark skin: design, fabrication and hydrodynamic function. *Journal of Experimental Biology*, 217(10):1656–1666, 2014.

Weymouth, G. D. and Yue, D. K. Boundary data immersion method for cartesian-grid simulations of fluid-body interaction problems. *Journal of Computational Physics*, 230 (16):6233–6247, 2011.

Weymouth, G. Chaotic rotation of a towed elliptical cylinder. *Journal of fluid mechanics*, 743:385–398, 2014.

Weymouth, G. and Triantafyllou, M. Global vorticity shedding for a shrinking cylinder. *Journal of Fluid Mechanics*, 702:470–487, 2012.

Weymouth, G. and Yue, D. K. P. Physics-based learning models for ship hydrodynamics. *Journal of Ship Research*, 57(1):1–12, March 2013.

Xia, D., Chen, W.-s., Liu, J.-k., and Luo, X. Using spanwise flexibility of caudal fin to improve swimming performance for small fishlike robots. *Journal of Hydrodynamics*, 30(5):859–871, 2018.

Yang, W., Song, B., Song, W., and Wang, L. The effects of span-wise and chord-wise flexibility on the aerodynamic performance of micro flapping-wing. *Chinese Science Bulletin*, 57(22):2887–2897, 2012.

Yin, X., Goudriaan, J., Lantinga, E. A., Vos, J., and Spiertz, H. J. A flexible sigmoid function of determinate growth. *Annals of botany*, 91(3):361–371, 2003.

Younsi, A., El-Hadj, A. A., Abd Rahim, S. Z., and Rezoug, T. Effects of the wing spacing, phase difference, and downstroke ratio on flapping tandem wings. *Proceedings of the Institution of Mechanical Engineers, Part C: Journal of Mechanical Engineering Science*, 236 (9):4689–4712, 2022.

Yu, D., Wang, L., and Yeung, R. W. Experimental and numerical study of ship-to-ship interactions in overtaking manoeuvres. *Proceedings of the Royal Society A*, 475(2225): 20180748, 2019.

Zdravkovich, M. Different modes of vortex shedding: an overview. *Journal of fluids and Structures*, 10(5):427–437, 1996.

Zhang, J., Liu, N.-S., and Lu, X.-Y. Locomotion of a passively flapping flat plate. *Journal of Fluid Mechanics*, 659:43, 2010.

Zhu, Q. Numerical simulation of a flapping foil with chordwise or spanwise flexibility. *AIAA journal*, 45(10):2448–2457, 2007.

Zhu, Y., Tian, F.-B., Young, J., Liao, J. C., and Lai, J. C. A numerical study of fish adaption behaviors in complex environments with a deep reinforcement learning and immersed boundary–lattice boltzmann method. *Scientific Reports*, 11(1):1691, 2021.

Zhu, Y., Pang, J.-H., Gao, T., and Tian, F.-B. Learning to school in dense configurations with multi-agent deep reinforcement learning. *Bioinspiration & Biomimetics*, 18(1): 015003, 2022a.

Zhu, Y., Pang, J.-H., and Tian, F.-B. Point-to-point navigation of a fish-like swimmer in a vortical flow with deep reinforcement learning. *Frontiers in Physics*, 10:870273, 2022b.

Zurman-Nasution, A., Ganapathisubramani, B., and Weymouth, G. Influence of three-dimensionality on propulsive flapping. *Journal of Fluid Mechanics*, 886:A25, 2020.

Zurman-Nasution, A. N., Ganapathisubramani, B., and Weymouth, G. D. Effects of aspect ratio on rolling and twisting foils. *Physical Review Fluids*, 6(1):013101, 2021a.

Zurman-Nasution, A. N., Ganapathisubramani, B., and Weymouth, G. D. Fin sweep angle does not determine flapping propulsive performance. *Journal of the Royal Society Interface*, 18(178):20210174, 2021b.